Czech Technical University in Prague
Faculty of Electrical Engineering
Department of Radioelectronics

FACULTY OF ELECTRICAL ENGINEERING CTU IN PRAGUE

Modeling of Space Variant Optical Systems

Doctoral Thesis

Ing. Petr Janout

Prague, February 2018

Ph.D. programme: Electrical Engineering and Information Technology
Branch of study: Radioelectronics

Supervisor: doc. Mgr. Petr Páta, Ph.D.
Supervisor-Specialist: Ing. Stanislav Vítek, Ph.D.

Supervisor:
doc. Mgr. Petr Páta, Ph.D.
Department of Radioelectronics
Faculty of Electrical Engineering
Czech Technical University in Prague
Technická 2
166 27 Prague 6
Czech Republic

Co-Supervisor:
Ing. Stanislav Vítek, Ph.D.
Department of Radioelectronics
Faculty of Electrical Engineering
Czech Technical University in Prague
Technická 2
166 27 Prague 6
Czech Republic

Věrušce

Declaration

I hereby declare that I worked out the presented thesis independently and I quoted all the sources used in this thesis in accord with Methodical instructions about ethical principles for writing academic thesis.

Praha, 23 February 2018   Petr Janout

Acknowledgements

Abstract

The doctoral thesis under the title Modeling Space Variant Optical Systems is focused on modeling imaging systems with a complicated PSF. The complexity of the PSF is caused by the wide angle of view and by optical aberrations or anisotropy and inhomogeneity of the optical material. The description of the imaging system is expressed by its Point Spread Function, i.e., by its impulse response. The PSF describes the influence of the imaging system (the optics, the sensor) and the influence of the transition medium (atmospheric turbulence). However, UW-FOV imaging systems complicate the modeling task, and current PSF models do not provide a suitable solution with the desired accuracy. The imprecision of the PSF description in parts of the FOV causes issues during deconvolution, further processing and precise measurements (astrometry, photometry) of ultra-widefield images. This thesis presents a PSF model with field-dependent polynomials. The model is based on Zernike polynomials up to the 8th order. An estimate of the parameters of the model is performed in the image plane, and this allows the imaging system to be modeled directly from the image data acquired by the system. The advantage is obvious. We do not need complicated measurements of optical parameters involving Shack-Hartman interferometry. The proposed model is used to provide a PSF model, including a set of coefficients and polynomials, and therefore provides the set and the power of the optical aberrations of the imaging system. The proposed PSF model has been verified on a series of simulated and acquired image datasets covering different types of imaging systems (CCD, CMOS) and optical designs.

Keywords: Zernike polynomials, N-gons, imaging, Field-of-View, space-variant.

Abstrakt

Dizertační práce Modelování prostorově variantních optických systémů se věnuje tématu modelování obrazových systémů s komplikovanou bodovou rozptylovou funkcí širokoúhlých systémů a anizotropních optických materiálů. Obrazové systémy se popisují pomocí impulsové odezvy (rozptylová funkce bodu). Impulsová odezva popisuje vliv obrazového systému (optické části a senzoru) a vliv přenosového média (např. vliv atmosféry). Extrémně širokoúhlé obrazové systémy komplikují modelování a současné modely neposkytují vhodné řešení s dostatečnou přesností. Nepřesnost popisu impulsové odezvy v okrajových částech zorného pole způsobuje problémy během dekonvoluce, dalšího zpracování obrazu a přesných měření (astrometrie, fotometrie) extrémně širokoúhlých a jiných prostorově variantních systémů. V dizertaci je navržen model impulsové odezvy založený na polynomech s prostorovou závislostí. Navržený model je založen na modelování vlnoploch pomocí Zernikových polynomů vyjádřených do osmého řádu. Odhad parametrů modelu probíhá v obrazové rovině a dovoluje modelování obrazového systému přímo z dat pořízených samotným systémem. Výhoda tohoto přístupu je zřejmá. Není nutné provádět složité měření optických parametrů pomocí Shack-Hartmanova interferometru. Aplikací zmíněného modelu je možné získat set koeficientů a příslušných polynomů optických aberací daného systému. Navržený model byl ověřen na několika sériích simulovaných dat, a dat pořízených různými typy obrazových systémů (CCD, CMOS) a optických designů.

Klíčová slova: Zernikovy polynomy, N-gony, zobrazovací systémy, zorné pole, prostorově variantní.

Contents

List of Figures

List of Tables

Glossary

ANN Artificial neural network

AOTF Acousto-Optic Tunable Filter

CCD Charge-coupled device

CMOS Complementary Metal Oxide Semiconductor

DSLR Digital Single-Lens Reflex camera

ESN Echo state network

FEO Front-End Optics

FFT Fast Fourier transform

FOV Field-of-View

FT Fourier transform

FWHM Full width at half maximum

GSOP Gram-Schmidt orthogonalization process

MAIA Meteor Automatic Imager and Analyzer

MD Maximum Difference

MTF Modulation Transfer Function

OA Optical axis

OTF Optical Transfer Function

PSF Point Spread Function

RMS Root Mean Square

RMSE Root Mean Square Error

SNR Signal-to-Noise Ratio

SV Space Variance

SVPSF Space-Variant Point Spread Function

THETIS Thermal Hyperspectral Imaging System

TIR Thermal Infra-Red

UWFOV Ultra-Wide Field-of-View

VIS Visible spectrum

WILLIAM WIde-field aLL-sky Image Analyzing Monitoring system

Introduction

Modern photonic imaging systems play an important role in our lives. They are used in astronomy, biomedicine, security and other areas of science, and they are required to perform with high imaging quality, a wide aperture (i.e., low F-numbers) and high spatial resolution. These systems are known as Ultra-Wide Field-of-View (UWFOV) systems. The wide-angle optical elements used in UWFOV systems introduce a significant shift variance [1], which complicates the modeling task. Many recent research works have focused on finding a model of UWFOV systems that is suitable for reducing the uncertainties in reconstructing image data from wide-field microscopic systems [2–4], security cameras [5–7], and all-sky cameras [8–13]. Extremely wide-field imaging systems have many advantages for the large display scenes used in microscopy, in all-sky cameras, and in security technologies. The wide viewing angle comes at the cost of a large number of aberrations, and this affects the observed objects, especially at wide angles. The second group of space-variant imaging systems consists of devices containing unique optical materials, e.g., Calomel. UWFOV and other Space-Variant Point Spread Function (SVPSF) systems are imaging systems with a complicated description, which is currently not perfectly addressed. These images are therefore processed with a significant error, or cannot be processed automatically, because each of the images is basically unique. The uniqueness of these images becomes an issue when a significant amount of data needs to be processed, and places demands on user interaction.

Modeling wavefront aberrations using Zernike polynomials [14] is well-known and is widely used. However, models based on Zernike polynomials are usually partially invariant, or they are simplified into singular points, and they do not account for the field dependency of polynomials. The proposed method models system aberrations by modeling the wavefront, and calculating the Point Spread Function of the imaging system that is used, since it is not possible to recover the wavefront from the Point Spread Function (PSF). This is a very complicated task, and it is difficult to achieve the desired accuracy with conventional methods. However, modeling the PSF directly in the image plane allows the imaging system to be estimated without complicated measurements of optical parameters using a Shack-Hartman interferometer. The analysis and the estimate of the optical para-

meters are processed on the testing dataset acquired by the imaging system itself. The proposed optimization techniques for searching the coefficients of space-variant Zernike polynomials can be described as a comprehensive model for UWFOV imaging systems. This model is an attempt to estimate the size of the modeled Point Spread Function, which is comparable to the pixel size. Issues associated with sampling, pixel size, and pixel sensitivity profile must be taken into account in the design. However, knowledge of the system's PSF allows us to process the images (detection, measurement) further, and to perform deconvolution and precise measurements in astronomy (astrometry, photometry).

Aims of the Doctoral Thesis

1. Propose a PSF model describing the field-dependent PSF over the entire Field-of-View (FOV), especially for UWFOV imaging systems. The model will extend current PSF models by expressing the field dependency of the PSF, and it will allow a description of distorted off-axis PSFs with the desired accuracy. This description allows parts of the FOV to be processed that were formerly problematic or impossible to process.

2. Adapt optical techniques for describing general imaging systems, such as the Zernike polynomials for describing the wavefront.

3. Verify and quantitatively analyze the proposed model on a series of image data acquired by SVPSF and UWFOV imaging systems, e.g. the WIde-field aLL-sky Image Analyzing Monitoring system (WILLIAM).

4. Confront the verification results of the PSF model estimation with the results obtained by competing models.

Structure of the Doctoral Thesis

The thesis is organized into six chapters as follows:

1. *State-of-the-Art*: The first Chapter establishes the position of the thesis in the field of optics design description, and its relation to three major works that laid the foundations of SVPSF modeling.

2. *SVPSF imaging systems*: Chapter 2 introduces the imaging systems used for the work presented here. The systems were developed at the Department of Radioelectronics, Faculty of Electrical Engineering, Czech Technical University in Prague, with the participation of the author of this thesis. The chapter includes a brief description of the WILLIAM imaging system, the Meteor Automatic Imager and Analyzer (MAIA) imaging system, and the Thermal Hyperspectral Imaging System (THETIS). The WILLIAM and MAIA cameras are space-variant due to their wide field of view. However, the THETIS instrument is space-variant due to the acousto-optical tunable filter, which uses the birefringent Calomel crystal.

3. *Theoretical background*: the third section is devoted to an analytic description of SVPSF systems, and it provides the mathematical tools for the development of the SVPSF model.

4. *Space-Variant optical model*: Chapter 4 introduces the proposed model, the field dependency of the model, and a verification of the versatility of the proposed solution.

5. *Verification of the SVPSF model*: This chapter aims to apply the proposed model to a series of space-variant image data, and to verify the model. A dataset was acquired and simulated by various sensors and optics covering the broad field of SVPSF systems. The verification demonstrated the precision of the proposed model. The results presented in this chapter are related to the results of the model introduced in Chapter 1.

6. *Conclusions*: The last chapter summarizes the results, and relates them to the objectives set in the introduction.

State of the Art

Any imaging system can be described by its spatial impulse response function, commonly referred to as the PSF. PSF is used to represent the aberrations of UWFOV devices simultaneously with a wavefront description, and can be applied either to the entire image or within regions uniquely defined by the isoplanatic angle. However, it can sometimes be complicated to obtain a PSF model of the system. It can be difficult to achieve the desired accuracy using conventional methods - not from the measurement point of view, but because it is difficult to describe the Space Variance (SV) of the PSF over the FOV. This leads to an obvious issue. From the measurement point of view, it is necessary to obtain the PSF for all discrete points of the entire FOV. Then the PSF of the system is described by such a field of individual PSFs. Born [15] calls this type of PSF partially space-invariant because there are just discrete points (PSFs) in parts of the FOV. However, a space-variant PSF is described by a model in all points of the acquired image. Of course, this brings high demands on the precision of the model. Issues associated with sampling, pixel size and the pixel sensitivity profile must be taken into consideration in the design. It is very difficult to obtain the parameters of the model, especially in image areas with a heavily aberrated impulse response and for objects with a small Full width at half maximum (FWHM) parameter in relation to the pixel size. These objects, captured, e.g., in microscopy using all-sky cameras and/or special optical elements, can hardly be processed using current techniques, which are typically oriented to multimedia content.

A widely-used approach for obtaining the PSF is to model wavefront aberrations using Zernike polynomials. These polynomials were introduced by Zernike in [16]. This work was later used by Noll [17], who introduced his approach to indexing, which is widely used in the design of optics. Zernike polynomials are usually applied to rotationally symmetric optical surfaces. Zernike polynomials form a basis in optics with Hopkins [18] field dependent wave aberration. Recently, Sasián [19] reformulated the work of Hopkins. This new formulation is more practical for optical design. A more recent contribution by Ye et al. [20] uses Bi-Zernike polynomials, which is an alternative to the method mentioned in Gray's article [21].

1.1 Related Work

Zernike polynomials are used in modern interferometers for describing wave aberrations. However, researchers have begun to think about using these polynomials for an overall description of lens optics. When the first all-sky camera projects appeared, the question of how to model aberrations of fisheye lenses arose. Following paragraphs provide an extended introduction to projects involving modeling of space-variant imaging systems. The approaches of particular projects exhibit common signs, such as using of Zernike polynomials. However, the particular solutions are individual and introduce significant ideas.

Reservoir Computing First of mentioned works is the approach of Weddell [22]. He proposed a predictive partially space-invariant model of PSF based on Zernike polynomials. His approach is based on a recurrent Artificial neural network (ANN). The prediction is used for modeling of PSF in an anisoplanatic region over the FOV. The ANN is used to learn the changes of aberrations (i.e., changes in PSF) over the entire anisoplanatic region. Weddell describes the architecture of reservoir computing as

$$
\begin{aligned}
X(n) &= \varphi^{trn}(w_{in}u(n)^T + w_{DR}X(n-1)^T + w_{back}Y(n-1)^T), \\
Y(n) &= \varphi^{out}(w_{out}X(n)^T),
\end{aligned}
\tag{1.1}
$$

where $X(n)$ is the input vector and $Y(n)$ is the output vector. w_{DR} is the sparse matrix used as dynamic reservoir matrix, the w_{out} is the linear output, the w_{in} is the input weight matrix. w_{back} represents the feedback matrix and $\varphi^{\cdot}$ are noted as activation functions. The predicted output of input series $u(n)$ is expressed as

$$
\hat{u}(n+1) = Y(n).
\tag{1.2}
$$

The Echo state network (ESN) is used for estimation of Zernike coefficients from obtained spatiotemporal data. Using the training, the output w_{out} output weight can be obtained as

$$
w_{out} = (Xw_{train})^+,
\tag{1.3}
$$

where X is the state vector and w_{train} represents training vector that comprises the Zernike terms Z and spatial data.

Pi of the Sky Another astronomical project, Pi of the Sky [1], focused on optical transients of gamma-ray bursts, attempted to make a model of PSF. Their approach was quite different from Weddell's [23]. Important part of the PSF model is the part describing the sensor sensitivity profile included in the expression of impulse response convolution function

$$PSF(r', \phi') = \iint PRF(r, \phi; r', \phi') \cdot PSF_L(r, \phi) r dr d\phi \qquad (1.4)$$

that relates the optical PSF at (r, ϕ) coordinates with sensor response function PRF. Coordinates r', ϕ' correspond with the specific point of final response function and (r, ϕ) denotes the coordinates of integration point. The polynomials used for wavefront description became from Zernike polynomial basis. However, the modeling method uses only the coefficients of astigmatism, coma, spherical aberration, trefoil, secondary coma and secondary spherical aberration. It should be noted, that author admits the possibility of extension to a bigger set of aberration coefficients. Thus, the wavefront equation is expressed as

$$\begin{aligned} W(\rho, \phi) =& A(\rho^2 cos2\phi) + C((3\rho^2 - 2)\rho cos\phi) + S(6\rho^4 - 6\rho^2 + 1) \cdots \\ &+ T(\rho^3 cos3\phi) + C'((10\rho^5 - 12\rho^3 + 3\rho)cos\phi) \cdots \\ &+ S'(20\rho^6 - 30\rho^4 + 12\rho^2 - 1). \end{aligned} \qquad (1.5)$$

Notation $A; C; S; T; C'; S'$ stands for mentioned aberrations. The method of modeling in the Pi of the Sky does not describe the complicated model of field dependency (except tilt or defocus, because these are present in diffraction formula), but it is of high importance, because it takes into account the non-uniform sensor sensitivity, i.e., the pixel sensitivity.

Characterization of SV aberrations in microscopy The search for the best description of UWFOV systems is not limited to the astronomical imaging. Microscopy is another area where the UWFOV type of lens is used. Measurements of the special spherical aberration using a shearing interferometer were described in [24]. A promising new approach was formulated in [25]. It is based on aberration measurements of photolithographic lenses with the use of hybrid diffractive photomasks. The aperture exit wavefront deformation is modeled in [26] for wide field-of-view fluorescence image deconvolution with aberration-estimation from Fourier ptychography. However, comprehensive work wrote Zheng [2]. Zheng's work uses the Zernike polynomials just like the previous work of Weddell or Piotrowski. However, Zheng described a convincing approach to a pattern search. It is based on optimization of pupil function recovery, where he determinates the estimated defocused and off-axis intensity images at specific positions. By recursive algorithm, he modifies the unknown pupil aberration, until the compared intensity image meets the desired match in the output. Using this approach, it is actually possible to estimate the unknown wavefront function as Zheng proved.

Gray [21] proposed a method for describing the spatial variance of Zernike polynomials. This approach is derived from the description provided by Hopkins [18] and laid the foundations for truly space-variant Zernike polynomials. Of course, there is also the problem of space-variant PSF. In fact, we cannot be limited to rotationally symmetric imaging systems only. Hasan [27] and Thompson [28] came

up with a more general description of the pupil function for elliptical or rotationally non-symmetrical Zernike polynomials. This description can be used for calculating the wave aberration in optical materials such as Calomel for acousto-optical elements [29]. The first optical approach to wave aberration estimation was described by Páta et al. [30]. Other works of Díaz [31] devoted to imaging by a hexagonal pupil system or work of Ferreira [32] devoted to polygonal facets description, should be mentioned. However, the fundamental works describing non-circular apertures proposed Mahajan [33, 34] and Díaz [35].

UWFOV cameras are also used in surveillance systems. However, an image affected by aberrations can have a negative effect in criminal investigations [6]. Ito et al. [5] face this issue, and they propose an approach that estimates a matrix of coefficients of the wavefront aberrations. Many authors have reported on investigations of space-variant imaging systems. An estimate of the PSF field dependency is critical for restoring the degraded image. Qi and Cheng proposed their linear space-variant model [36] and focused on the restoration algorithm for imaging systems. Heide et al. [37] proposed techniques for removing aberration artifacts using blind deconvolution for the imaging system with a simple lens.

In this thesis, it is proposed a modeling method for PSF estimation for space-variant imaging systems. Since we would like to use this model for general optical systems, the method is based on modeling the PSF of the system without knowledge of the wavefront. Thus, the method can be an alternative to the Shack-Hartmann interferometer [4, 38], or to other direct wavefront measurement methods, since we can estimate wavefront aberrations from fitting PSF in the image plane. A workbench for testing and experiment purposes is our project WILLIAM [39] that faces the issue of aberrations at an extremely wide-field FOV (see also [40, 41]). Following chapter focuses on the brief description of the WILLIAM and other SVPSF imaging systems.

SVPSF imaging systems

This chapter focuses on the introduction of the realized projects of the spatially-variant point spread function imaging systems at our department. These systems can be divided into UWFOV systems and SVPSF anisotropic material-based imaging systems. Parts of this chapter were published in [39], [42] and [43].

2.1 Description of the space-variant system

A basic general imaging system consisting of front-end optics (lens or mirrors), optionally filter (Infra-Red cut, a spatial filter, etc.) and a sensor that is not limited to paraxial rays and changes its impulse response across the FOV is defined as a SVPSF imaging system. As can be seen in Figure 2.1, the Front-End Optics (FEO) transforms input plane wavefront into spherical wavefront, because the lens is designed to be focused to the image plane, where is placed the sensor. However, the theoretical spherical wavefront is produced only by an ideal aberration-free optics. In practice, the transmitted wavefront is deformed by the amount of aberration which produce aberrated spherical wavefront, as illustrate Figure 2.1. Then, it has to be taken into account that every part of the imaging system produces some kind of deformation of the transmitting wavefront. The model of the imaging system then describes the resulting transform function including contributions from all involved parts of the system. The SVPSF imaging systems usually have heavily deformed wavefront due to wide-field viewing angle (deformation of the scene) or due to the optical material (anisotropy, non-homogeneity, scratches, bubbles).

The imaging system transforms the ideal wavefront into the wavefront deformed by aberrations. This transformation can be described by convolution between the input image function $f(\xi, \eta)$, the PSF $h(u, v; \xi, \eta)$ and the noise $n(u, v)$. The output linear function $g(u, v)$ [44] is described as

$$g(u, v) = \iint\limits_{-\infty}^{\infty} f(\xi, \eta) h(u, v; \xi, \eta) d\xi d\eta + n(u, v). \tag{2.1}$$
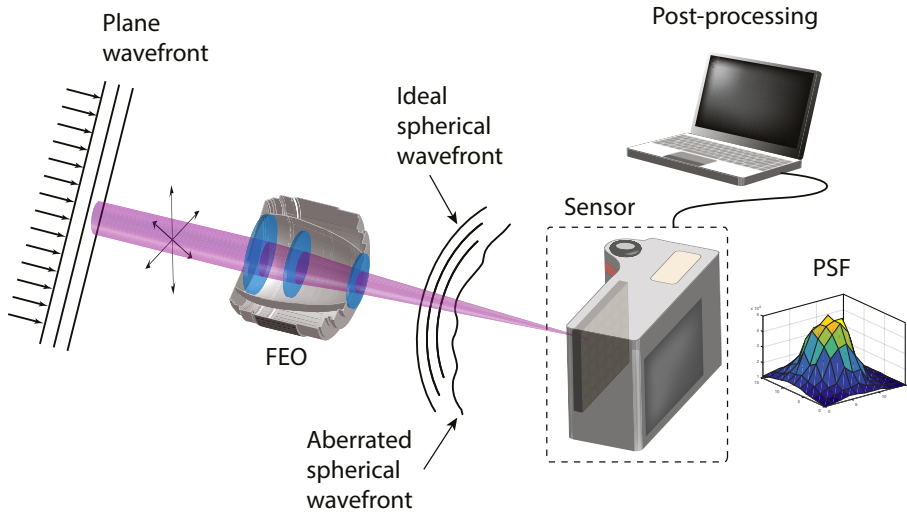
Figure 2.1: A scheme of a general imaging system including illustration of the wavefront deformation.

The PSF provides information about deformations caused by the imaging system, or more generally, the information about image deformations caused by transmitting medium. However, precious description of SVPSF cannot stand alone without proper measurement of basic characteristics. The PSF measurement starts with the setting of a point light source, a distance of the imaging system from the light source. Measurement of a Modulation Transfer Function (MTF) has to be performed in several locations to cover entire FOV, similarly to PSF measurement. Therefore, the wide angle of UWFOV systems requires modification of the standard techniques of an image data acquiring. An adaptation of these techniques using a nodal stage was summarized in [45].

Another factor, which has to be taken into account is natural color blindness of imaging sensors. There are two major ways how to obtain a color image. The first way is used mostly in specialized Charge-coupled device (CCD) cameras which have filter carousel and can obtain one color channel per exposure. This method has an advantage in the usage of the full resolution of the sensor, but for RGB image three exposures are needed. The second method is spread mostly in Digital Single-Lens Reflex camera (DSLR) and end-user cameras. They use Bayer color filter array to acquire all three (red, green and blue) colors at one exposure, but the resolution in each channel is lower due to filter cells placement, as can be seen from Figure 2.2. To correctly decode image some kind of image interpolation must be used. The method of interpolation can affect some details and artifacts in the image. Then the appropriate method must be selected because astronomical images with stars as regions of the high-frequency signal are specific and straightforward bilinear transformation is not suitable for its tendency to create artifacts in those places. For this reason, adaptive edge sensing method has been utilized. Laroche

and Prescott's interpolation [46] represents a good compromise between simplicity; that means an only minimal change in a star shape and good artifact suppression.

(a) Decomposed RGB image.

(b) The original image of a stellar object.
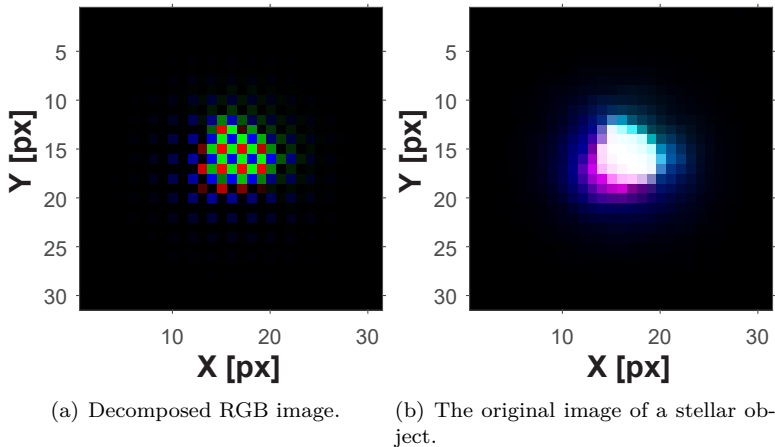
Figure 2.2: Comparison of the stellar object illustrated after interpolation of Bayer mask (b) and same object shown with Bayer mask RGB sampling (a).

2.2 MAIA

The MAIA [47] is a project of double station observation of meteors using two video systems coupled with image intensifiers located at the Ondřejov observatory and the Kunžak observatory. The MAIA is space-variant astronomical imaging system as well as the system WILLIAM. As it was described in [48] and [11], MAIA cameras use an image intensifiers to get the best observation of the night sky. The image intensifier allows real-time detection [49] of meteors down to masses of fractions of one gram. Due to the usage of video recording instead of capturing images with a camera, the MAIA does not have precise spatial resolution and high dynamic range. However, because of video recording, it provides sequences from which is possible to calculate the atmospheric trajectory of meteors and other properties. The design of hardware setup is based on a previous analog system which was based on VHS cam-coders. Here could be seen long tradition has the meteor detection and analysis at the Astronomical Institute of the Czech Academy of Sciences of the Czech Republic. Modern digital output with gigabit ethernet cameras allowed automatic observation process.

The main components are the input lens, image intensifier, camera lens and the camera itself. The input lens is Pentax SMC FA $1.4/50mm$[1]. As mentioned the MAIA is equipped with the image intensifier. Involved intensifier Photonis XX1332 has large diameter input (50 mm) and output (40 mm) apertures, high gain (typically 30 000 to 60 000 lm/lm) and the good resolution (typically 30 lp/mm). Image

---

[1]https://www.pentaxforums.com/lensreviews/SMC-Pentax-FA-50mm-F1.4-Lens.html

acquisition is provided by monochromatic camera JAI CM-040GE[2] with 1/2" progressive scan CCD sensor offering 776 x 585 (0.45 megapixels) resolution with 8.3 um square pixels (active area of the chip 6.49 x 4.83 mm). Image data are 10 or 8-bit, and the camera provides 61.15 frames per second with full resolution in continuous operation. The important parameter is high non-linearity caused by the automatic gain control in the image intensifier. The automatic gain control provides the extremely high dynamic range. However, it causes the non-linearity.
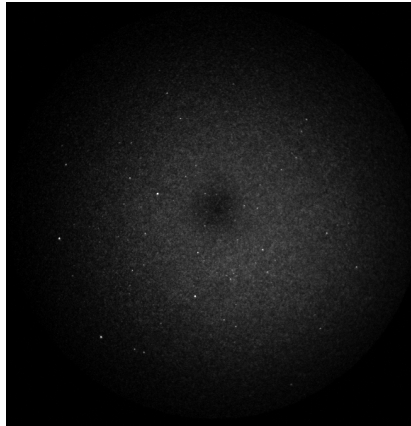
(a) Acquired image during night observation.
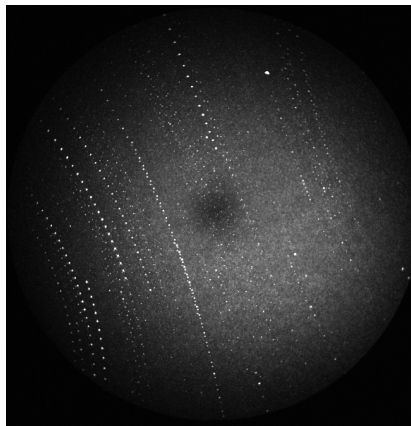
(b) Star Trails - stellar motions during one hour of observation.

Figure 2.3: Images acquired and processed by the MAIA system.

---

[2]http://www.jai.com/en/products/cm-040ge

2.3 THETIS

The THETIS project focuses on the development of a Thermal Hyper-spectral Imaging System integrating a Calomel-based Acousto-Optic Tunable Filter (AOTF) for 5 μm and with possible extension to Visible spectrum (VIS) and the Thermal Infra-Red (TIR) band, up to 10 μm. The potential of the THETIS instrument is in observation of soil monitoring, volcanism, atmosphere and risk management from Earth's orbit (or another planetary orbit). Other potential applications can be found in surveillance systems, environment monitoring (oil spills), where the observation distance is smaller. Figure 2.4 shows a basic scheme of the THETIS instrument. As can be seen, a FEO focuses the input light into the Calomel crystal based AOTF, and the light propagates through the precise cube polarizer. The transducer power-loads the AOTF unit by an acoustic wave that excites temporary local changes in the Calomel crystal forming the diffraction grid. The light passing through this grid diffracts and results in the spectral image. However, to obtain the full hyper-spectral image, it is necessary to change the acoustic frequency and obtain a series of the spectral images. Smart processing of the image series provides the hyperspectral images of the observed scene. However, the tuning of the wavelength is limited by the band where the crystal filter is optimized.
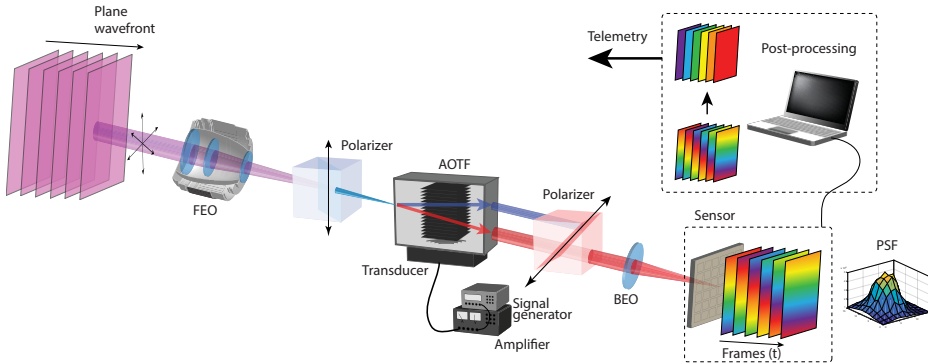
Figure 2.4: The set of Zernike polynomials used here. Table 4.1 includes the field dependency of these polynomials.

The strength of the THETIS instrument is the bandwidth, where it can operate (VIS to TIR). The most important part is the AOTF unit, or more specific, the Calomel crystal. This optical material allows work with such a wide range of wavelengths and applications. However, the design of the AOTF unit is a complicated task, based on calculating of light and acoustic wave propagation through the crystal. Description of the AOTF design is well-written in work of Chang [50] or Voloshinov [51]. An important part is the chosen interaction regime, i.e., Raman-Nath or Bragg's regime. The project THETIS is in the phase of breadboard model at the moment, and all tests of acoustic matching, diffraction efficiency, etc. are subjects of further research.

2.4 WILLIAM

The WILLIAM[3] is the imaging system designed and manufactured at the Department of Radioelectronics, FEE, CTU in Prague. It was first introduced in [39], and it is the UWFOV imaging system designed for monitoring and evaluation of the weather conditions. The main purpose of the WILLIAM was obtaining night sky images and analysis weather conditions during the night with an extension to the stellar object detection and identification [39,52]. The images acquired during the day were not subjects of the analysis, until Blažek [53] described his approach of the clouds color analysis. This approach allows evaluation of the weather conditions during the day, and due to the results mentioned in [53], we can recognize rain and storm clouds and sudden weather changes. The WILLIAM can also capture various atmospheric phenomena like storms, halos, auroras, airglow. Furthermore, some selected bright deep-sky objects and about 100,000 stars at ideal conditions with low light condition stars up to 8.8 mag can be detected. An example of observed magnitudes can be seen in Figure 2.5 and Figure 2.6.

(a) Detected stellar objects and visible magnitudes.

(b) Detected stellar object C/2014 Q2 Lovejoy [54].

Figure 2.5: Images acquired and processed by the WILLIAM imaging system.

Except mentioned weather condition evaluation, the WILLIAM imaging system was used for obtaining of ultra-wide-field of view image datasets. These valuable data were used while designing the algorithm of the PSF estimation, described in [42]. Our approach to the PSF estimation and modeling of the UWFOV imaging systems follows our effort of the description of the imaging systems described in [55]. The data acquired by WILLIAM was used in a number of publications such as by Fliegel [56], Anisimova [57], Vítek [58–60] and Trigo-Rodriguez [61]. At the moment, the WILLIAM operates in two versions - the second and the third generation. The second generation of the WILLIAM is placed in Jarošov nad Nežárkou in South Bohemia (GPS 49.185N, 15.072E). The third generation is placed on the roof of Faculty of Electrical Engineering, Czech Technical University in Prague (GPS 50.103N 14.3933E), see the map in Figure 2.8.

The first generation operated in Prague since mid-2014 and in 2017, was replaced by the third generation camera system equipped by the ZWO astronomical

---

[3]http://william.multimediatech.cz/
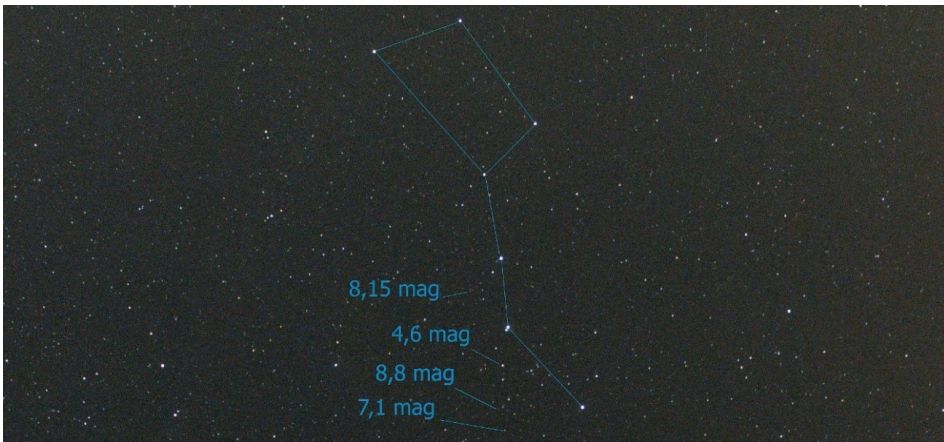
(a) Detected stellar objects and visible magnitudes.

Figure 2.6: Images acquired and processed by the WILLIAM imaging system.

camera. The second station (2nd generation) operates in Jarošov since mid-2015 and it is still equipped by DSLR camera.
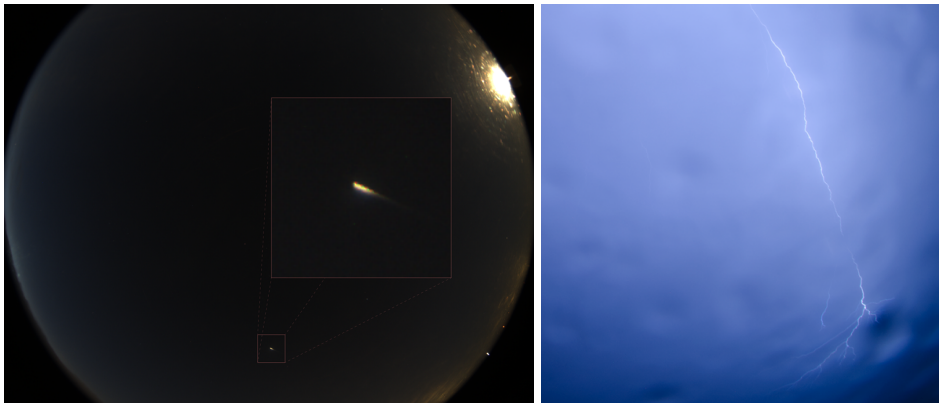
(a) Acquired bolid.

(b) Acquired flash.

Figure 2.7: Images acquired and processed by the WILLIAM imaging system.

2.4.1 Camera hardware

The core of the WILLIAM imaging system is naturally the camera. The first generation of the WILLIAM used the Nikon D5100 DSLR camera[4] with a $23.6 \times 15.6\ mm$ and 4928×3264 pixels resolution back-illuminated Complementary Metal Oxide Semiconductor (CMOS) sensor. This DSLR camera was later replaced by the

---

[4]http://imaging.nikon.com/lineup/dslr/d5100/

newer Nikon D5300 equipped by a sensor with same size 23.5×15.6 *mm*, but higher resolution - 6000×4000. The third generation is designed to operate astronomical cameras. One of the stations, placed in Prague, uses the ASI 178MC color camera[5] with a 7.4×5 *mm* and 3096×2080 pixels resolution CMOS sensor. However, a housing of the third generation of the WILLIAM can hold even bigger cameras such as ASI 1600MM-Cool[6]. The ASI 1600MM-Cool provides a high-resolution cooled 17.6×13.3 *mm* and 4656×3520 pixels CMOS sensor. However, letters MM in the name of the camera indicates that it is a monochromatic sensor-equipped camera. The advantage is an absence of the Bayer mask and therefore sampling among color channels. However, obtaining of the color image datasets is essential for clouds analysis. Therefore we have to use additional color filters such as LRGB filters[7] provided by the manufacturer of the ASI camera. The 1.25" LRGB filters have more than 92% transmission at pass-band, a multi-layer anti-reflection coating and cut-off at 700-1100 nm in infra-red band.
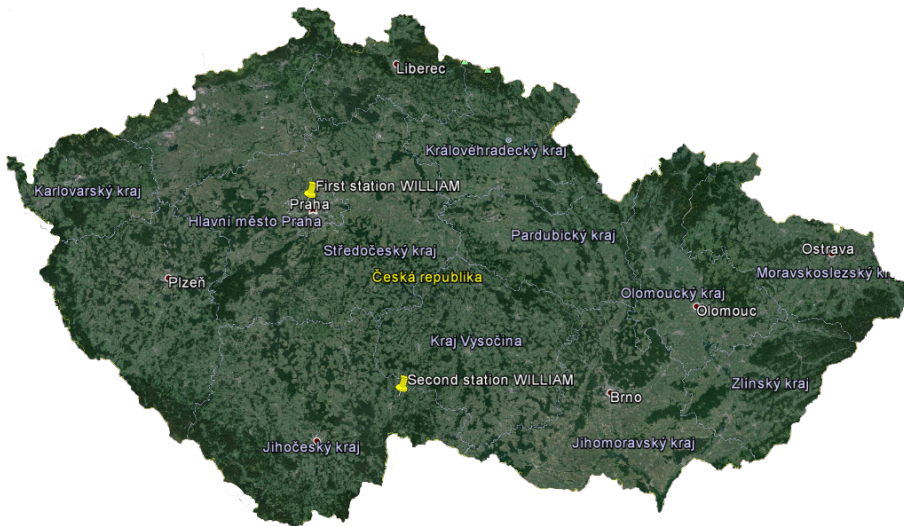
Figure 2.8: The locations of the two stations of the WILLIAM.

As can be seen, we experiment with different types of astronomical cameras, because different tasks require different cameras. For clouds detection algorithm is suitable for the ASI 178MC camera or DSLR camera Nikon D5100. They produce color images, that is essential for image clustering, and mentioned clouds detection does not require a high-resolution sensor. The advantage of the Bayer mask is that ASI 178MC obtain a color image by one capture and there is no image shift in RGB channels when shooting multiple captures. Whereas the camera ASI 1600MM-Cool with the high-resolution sensor is suitable for stellar objects observations. An additional filter wheel allows using different high precision filters.

---

[5]https://astronomy-imaging-camera.com/products/usb-3-0/asi178mc-color/
[6]https://astronomy-imaging-camera.com/products/USB-3-0/asi1600mm-cool/
[7]https://astronomy-imaging-camera.com/products/filterfilter-wheel/
zwo-new-rgbl-filters-optimised-asi1600/

Figure 2.9 shows a basic scheme of the new generation of the WILLIAM. As can be seen, the scheduler controls tasks planned repeatedly or some occasional tasks defined by the user. The camera systems are complemented by additional sensors of the humidity, atmospheric air pressure, temperature, and it can be connected to a conventional weather station. Furthermore, from Figure 2.9 can be seen that different types of outputs can be achieved. When the camera system obtains an image with evidence of rain or storm clouds in the image, the analyzing algorithm should detect potential danger and create an alarm. This part of the system can serve as prevention before the sudden rain. Another type of the output can be a visualization of the detected clouds, statistics of cloud level and a number of visible stellar objects.
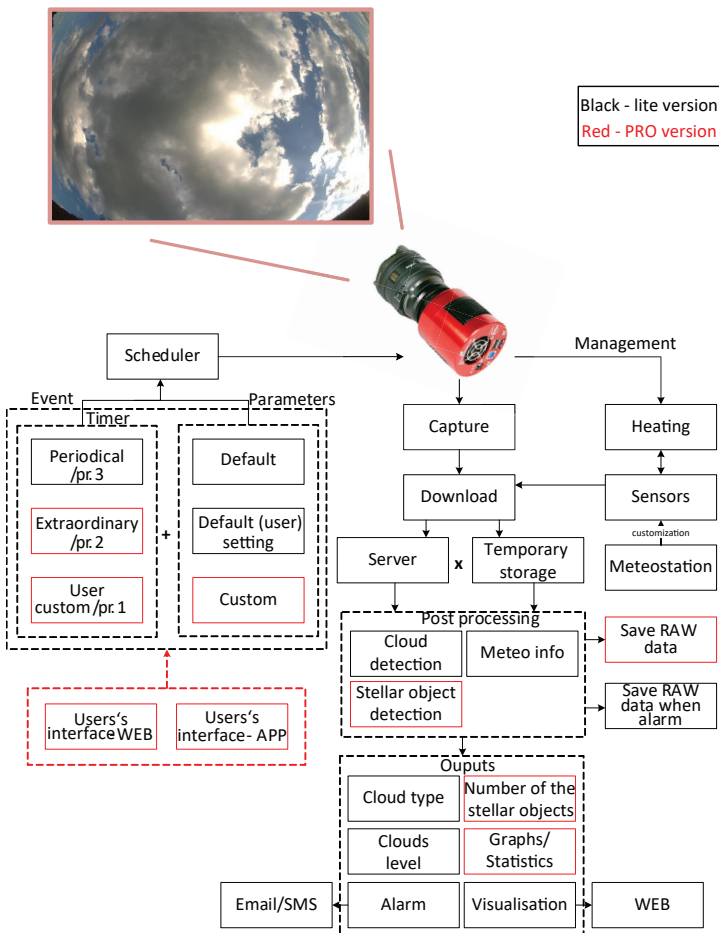
Figure 2.9: The scheme of the WILLIAM imaging system. The WILLIAM can operate without user management. However, it is prepared to proceed scheduled tasks defined by the user. Output can be realized in a form of graphs, alarms or visualization of the clouds.

2.4.2   Color processing

During designing of the new generation of the WILLIAM camera, we have used findings reported in previous papers mentioned above. The new generation of the WILLIAM reacts to last requirements in image processing of the weather condition observations. We have introduced in [43] our SVPSF estimation algorithm and clouds analysis including the results of the SVPSF model and MTF comparison of both generations of cameras. We found explicit statistical criteria to distinguish different cloud types from a clear sky in the luminous-less color diagrams. Measured data provide valuable information about the used camera and optics that can be used for compensation of the aberrations during analysis.
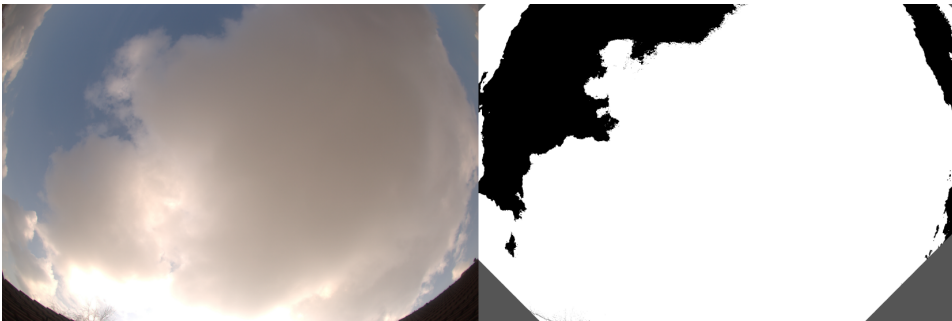
Figure 2.10: An example of acquired day image from Jarošov and the corresponding image of clusters after segmentation.

As mentioned, the WILLIAM camera processes day images to obtain the information about cloud type. The algorithm is based on the processing of the color information. The output of digital camera sensors is usually represented in RGB channels with the information about both color and luminosity. Following procedure describes the case of the color sensor with Bayer mask. This process makes use of standardized calibration from AdobeRGB space. However, any other appropriate calibration may be used (such as sRGB). If the monochromatic camera is used then the corresponding calibration from the set of color filters (such as Johnson photometric UBVRI or standard RGB) based on the knowledge of spectral response into other color spaces is necessary. The influence of the atmospheric conditions (clouds, clear sky, rain) on the color has been discussed in [62,63]. Transformation into other color spaces such as CIE 1931 [64], CIE L*a*b* [65] or YCbCr [66] can separate color from luminosity. This was proved to be useful for the automatic cloud boundary recognition and rough cloud type classification [53]. The reason is that for the RGB system it is necessary to use the combination of all three channels, while for the other color transformations the luminosity channel can be excluded for following image processing segmentation. Illustration of image after segmentation is in Figure 2.10. Therefore, only a* and b* may be used in CIE L*a*b*, x and z for CIE 1931 and only channels Cb and Cr for the color system YCbCr. The considerable advantage of using, e.g., L*a*b* transformation instead of the standard RGB system is to separate the clouds from the clear sky or even to distinguish different types of clouds from the others [53].

A crucial part of the algorithm is the transformation into different color space, and as well following image processing segmentation which uses just two chrominance channels without the information about the cloud/sky luminosity. For this purpose the K-means segmentation [67] has been proved as very useful [53]. Images from WILLIAM database are separated into three independent sectors (clusters) of similar colors regardless of the luminosity channel. The resulting color-color diagrams (combination of two chrominance channels, such as R-G for RGB or x-y for CIE 1931) can show up statistically the position of each color segment (for instance stormy cloud or clear sky in the wide-field). Based on our preliminary measurements from few hundreds of transformations it seems that dense and rainy clouds such as Cumulus, Cumulonimbus, and Nimbostratus tend to occur in the statistical areas for CIE 1931 [53].

Theoretical background

The following chapter focuses on the description of a mathematical background that is used for modeling of the imaging systems. The chapter begins with the PSF description, since it is the function including the influence of the system. Follows the description of the wavefront modeling using the Zernike polynomials and adaptation of these polynomials to an N-gonal aperture. Parts of this chapter were published in [42], [68] and [69].

3.1 Point Spread function

The description of the general optical system should start with the geometrical optics model. However, this model is not fully satisfactory as determined by Abbe in 1873, when he proposed the theory of image formation [70, 71] assuming coherent illumination. Although, it was Hopkins [18, 72, 73], who described his model allowing the Fast Fourier transform (FFT) for practical calculations. Considering a basic image creation as transformation of the input wavefront through an apertures (considering that lens has entrance and exit aperture), the PSF can be expressed by Rayleigh-Sommerfeld equation, as described in [44], or using boundaries by Helmholtz-Kirchhoff formulation that are essential formulations of aperture integral describing image creation and providing corresponding diffraction pattern. However, assuming the aperture and image size much smaller than z (the distance from exit aperture to the image plane), the Fresnel approximation of complex field $U(u, v)$ becomes

$$U(u,v) = \frac{e^{jkz}}{j\lambda z} \iint\limits_{-\infty}^{\infty} P(x,y) \exp\left(\frac{jk}{2z}[(u-x)^2 + (v-y)^2]\right) dxdy, \qquad (3.1)$$

where $P(x, y)$ is unity describing amplitude transmittance, k is the wavenumber. The coordinate system is illustrated in Figure 3.1. The object plane is described by the ξ, η coordinates; the exit pupil uses x, y notation, and the image plane uses u, v notation.

The Fresnel expression is, in fact, a paraxial solution for small angles around the optical axis. Considering larger distances, where $z > \frac{k(x^2+y^2)}{2}$, the Fraunhofer approximation becomes valid as

$$U(u,v) = \frac{e^{jkz}}{j\lambda z} \exp\left(\frac{jk}{2z}(u^2+v^2)\right) \iint\limits_{-\infty}^{\infty} P(x,y)\exp\left(-j\frac{2\pi}{\lambda z}(ux+vy)\right)dxdy.$$

(3.2)
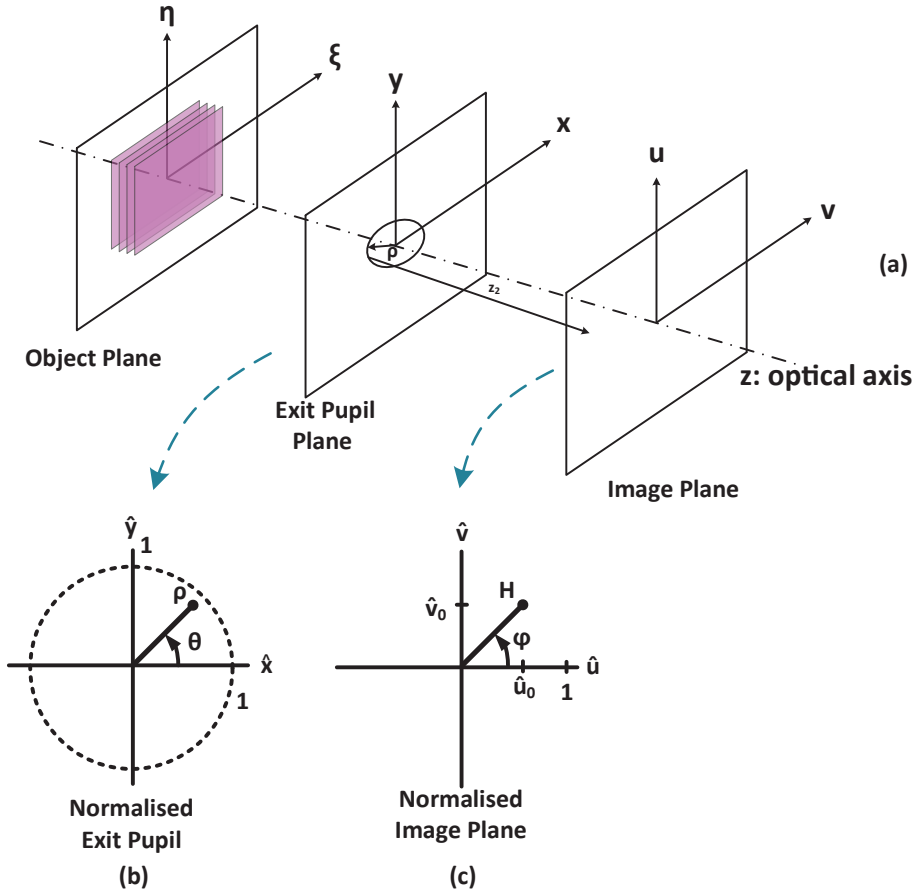
Figure 3.1: Graphical representation of the adopted coordinate systems. Subfigure (**a**) illustrates all planes, subfigure (**b**) illustrates normalized exit pupil plane and (**c**) illustrates notation of normalized Image plane.

However, optics is usually affected by various aberrations, such as distortion which makes the PSF of the system space-variant, i.e., the PSF changes across the field of view. It is, therefore, necessary to use a complicated model of the

system's PSF with a perfect agreement with previous results with the Fraunhofer diffraction pattern, using a description of the wavefront aberration $W(x,y)$. It should be noted, that both, Fresnel and Fraunhofer formulas can be expressed by Fourier-transform. Let's begin with a linear space-invariant optical imaging system, which can be expressed as

$$h(u,v) = |\mathcal{F}\{P(x,y)\}|^2 = \left| \mathcal{F}\left\{ p(x,\ y)\exp\left(-i\frac{2\pi}{\lambda^2}W(x,y)\right)\right\}\right|^2, \tag{3.3}$$

where $p(x,y)$ is the unity inside and zero outside that defines the shape, the size, and the transmission of the exit pupil, and $W(x,y)$ is the phase deviation of the wavefront from a reference sphere. The symbol of $\mathcal{F}$ denotes the Fourier-transformation. The generalized exit pupil function is described in [44] as

$$P(x,y) = p(x,y)\exp\left(-i\frac{2\pi}{\lambda}W(x,y)\right). \tag{3.4}$$

An imaging system is space-invariant, if the image of a point source object changes only in position, not in the functional form [22]. However, wide-field optical systems give images where the point source object changes both in position and in functional form. Thus, wide-field systems and their impulse responses lead to space-variant optical systems. Then, from Equation (3.2) the light amplitude point light source is the Fraunhofer expression at $u = M\xi, v = M\eta$ [6] [44] described as

$$h(u,v;\xi,\eta) = \frac{1}{\lambda z_1 z_2} \iint\limits_{-\infty}^{\infty} P(x,y)\cdots$$
$$\cdots \exp\left\{-j\frac{2\pi}{\lambda z_2}[(u-M\xi)x + (v-M\eta)y]\right\}dxdy. \tag{3.5}$$

Impulse response of the SVPSF then can be expressed as

$$h(u,v;\xi,\eta) = \frac{1}{\lambda^2 z_1 z_2} \iint\limits_{-\infty}^{\infty} p(x,y)\exp\left(-i\frac{2\pi}{\lambda}W(x,y)\right)\cdots$$
$$\cdots \exp\left\{-j\frac{2\pi}{\lambda z_2}[(u-M\xi)x + (v-M\eta)y]\right\}dxdy, \tag{3.6}$$

with a defined magnification of the system

$$M = -\frac{z_2}{z_1}, \tag{3.7}$$

where z_1 is the distance from the object plane to the principal plane and z_2 is the distance from the principal plane to the image plane.

3.2   Wavefront Aberration Functions

An ideal diffraction limited imaging system transforms a spherical input wave with an inclination equal to the plane wave direction. As described by Hopkins [18], real imaging systems convert the input plane wave into a deformed wavefront. The difference between an ideal wavefront and an aberrated wavefront in the exit aperture can be expressed as

$$W(x, y) = W_{ab}(x, y) - W_{sp}(x, y), \tag{3.8}$$

where $W(x, y)$ are wavefronts - the surface of points characterized by the same phase. Figure 3.2 illustrates the shape of the ideal spherical wavefront $W_{sp}(x, y)$ and aberrated wavefront $W_{ab}(x, y)$. Then the $\hat{x}, \hat{y}$ normalized coordinates are introduced (see Figure 3.1b,c) at the exit pupil and ρ, θ polar coordinates. The normalized image plane coordinates are $\hat{u}, \hat{v}$ and H, ϕ, respectively.
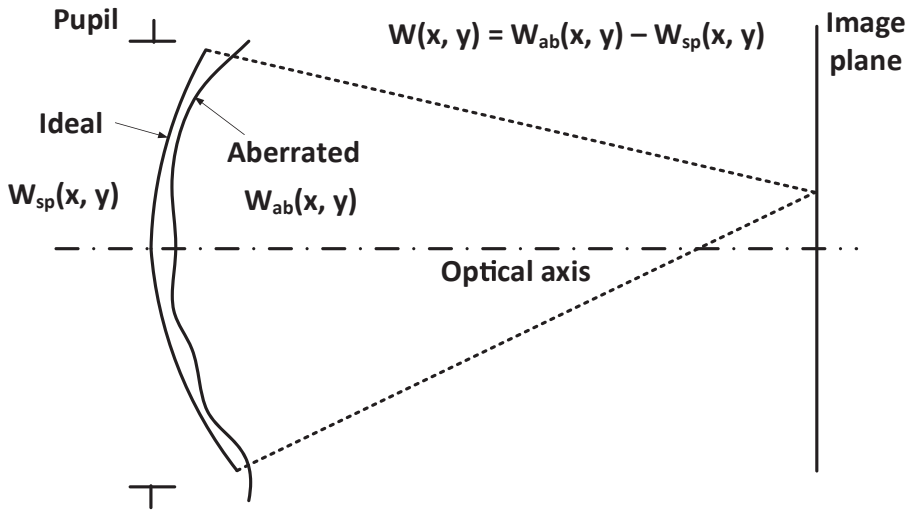
Figure 3.2: The difference between an ideal spherical wavefront and an aberrated wavefront.

The aberrated wavefront can be represented by a set of primary Seidel aberrations [74]. The primary aberrations are described by a series as

$$\begin{aligned} W\left(x, y\right) = A_0 + A_1\rho cos\theta + A_2\rho sin\theta + A_3\rho^2 + A_4\rho^2 cos\left(2\theta\right) + \dots \\ \dots A_5\rho^2 sin\left(2\theta\right) + A_6\rho^3 cos\theta + A_7\rho^3 sin\theta + A_8\rho^4 + \dots, \end{aligned} \tag{3.9}$$

where expansion coefficients A_i relate to piston, tilt, defocus, astigmatism, coma and spherical aberration. ρ and θ are a polar normalised pupil coordinates, according to Figure 3.1. However, more popular representation of the wavefront description is a set of orthonormal base functions, known as Zernike polynomials. Zernike polynomials, which are described in [16] and in [75–78], are a set of functions orthogonal over the unit circle, usually described in polar coordinates as $Z_n^m(\rho, \theta)$, where ρ is the radius and θ is the angle with respect to the $\hat{x}$-axis in the exit aperture (see Figure 3.1b). They represent functions of optical distortions that classify each aberration using a set of polynomials. The set of Zernike polynomials is defined in [16]; other adoptions are in [75–78], and it can be written as

$$
\begin{aligned}
Z_n^m(\rho, \theta) &= N_n^m R_n^{|m|}(\rho) \cos(m\theta) & m \geq 0 \\
Z_n^m(\rho, \theta) &= -N_n^m R_n^{|m|}(\rho) \sin(m\theta) & m < 0
\end{aligned}
\quad , \tag{3.10}
$$

with n describing the power of the radial polynomial and m describing the angular frequency.

$$
N_n^m = \sqrt{\frac{2(n+1)}{1 + \delta_{m0}}}, \tag{3.11}
$$

is the normalization factor with the Kronecker delta function $\delta_{m0} = 1$ for $m = 0$, and $\delta_{m0} = 0$ for $m \neq 0$, and

$$
R_n^{|m|}(\rho) = \sum_{s=0}^{(n-|m|)/2} \frac{(-1)^s (n-s)!}{s! \left[\frac{(n+|m|)}{2} - s\right]! \left[\frac{(n-|m|)}{2} - s\right]!} \rho^{(n-2s)}, \tag{3.12}
$$

is the radial part of the Zernike polynomial.

Any wavefront phase distortion over a circular aperture of unit radius can be expanded as a sum of the Zernike polynomials as

$$
W(\rho, \theta) = \sum_n^k \sum_{m=-n}^n a_n^m Z_n^m(\rho, \theta), \tag{3.13}
$$

which can be rewritten using Equation (3.10) as

$$
W(\rho, \theta) = \sum_n^k \sum_{m=0}^n a_n^m N_n^m R_n^{|m|}(\rho) \cos(m\theta) - \sum_n^k \sum_{m=-n}^{-1} a_n^m N_n^m R_n^{|m|}(\rho) \sin(m\theta), \tag{3.14}
$$

25

where m has values of $-n, -n+2, \ldots n$, k is the order of the polynomial expansion, and $a_n^m = a_n^m(H, \varphi)$ is the expansion coefficient of the Z_n^m aberration term in the expansion, i.e., it is equal to the Root Mean Square (RMS) phase difference for that mode. The wavefront aberration function across the field of view of the optical system can then be described as

$$W(\rho, \theta, H, \varphi) = \sum_{n=0}^{k} \sum_{m=-n}^{n} a_n^m (H, \varphi) Z_n^m (\rho, \varphi - \theta), \qquad (3.15)$$

where the wavefront is described with normalized polar coordinates. A better understanding can be provided by Table 3.1 and by Figure 3.3, which describes the indexing of Zernike polynomials and the kind of aberration associated with an index of Zernike polynomials.
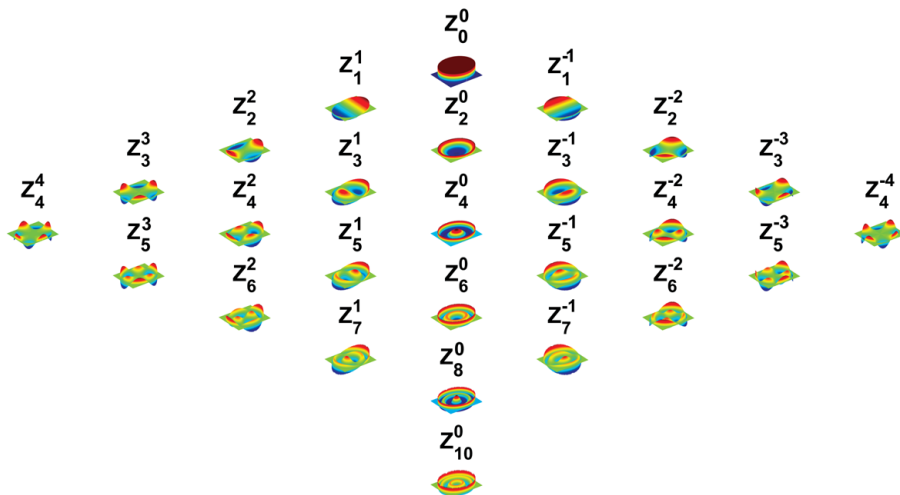
Figure 3.3: The set of Zernike polynomials used in the model. Table 4.1 includes the field dependency of these polynomials.

3.3   Introduction to aperture shapes

Optical design is not limited to circular shapes. Imaging systems can be designed with various types of aperture shapes, e.g., squares, rectangles, ellipsoids or mirrors with a hexagonal shape. However, N-gon polynomials require adapted orthogonal polynomials, because the Zernike polynomials are not orthogonal over non-circular apertures. The Zernike polynomials form a complete set of orthogonal basis functions on the unit circle, where the addition or subtraction of several polynomials does not affect the rest of the coefficients. Upton [79] published a description of the Gram-Schmidt orthogonalization process (GSOP), which can be applied to apertures of arbitrary shape. They provide treatment of each basis function as

a linear combination of circular Zernike polynomials. However, the most important and most comprehensive works have been written by Mahajan starting with a description of the Gram-Schmidt [80] orthogonalization process for non-circular polynomials in [81]. In this work, the authors describe how to obtain the orthonormal polynomial basis set for a hexagonal aperture by recursive GSOP. This work was followed up by [33, 82], where Mahajan and Dai propose an analytic solution for orthonormal basis functions for a hexagon, a rectangle, a square, an ellipse and a slit as the limiting case of a rectangle. Works of Mahajan [33, 82] are included in summarizing and extended paper [77]. As has been mentioned, Mahajan's work was based on a recursive algorithm of the GSOP. However, the GSOP recursive algorithm becames unstable when the number of basis functions is increased. Dai [83], therefore, came up with a solution that uses a non-recursive method with a matrix formulation.

The motivation of the following work is to obtain a set of orthonormal polynomial basis functions for a general N-gon, based on the Zernike circular polynomials. The N-gon is a general polygon with N vertices. Non-circular apertures can be found for example in numerous applications such as polygonal mirrors of large telescopes [84] or applications of the Calomel crystal with a square aperture window [29, 30, 85]. The next example of the non-circular aperture is the camera lens aperture formed by tight blades that can change the size of the aperture, and the blades form the shape of a polygon. Figure 3.4 shows an example of the pentagonal, heptagonal and nonagonal aperture shapes of ordinary camera lenses used in the WILLIAM experimental camera [39], e.g. Canon EF 50 mm f/1,8 II, Nikkor AF-S 18-70 mm f/3,5-4,5 DX and Nikkor AF 85 mm f/1,8 D. As has been mentioned, published works have described the expression of analytic orthonormal polynomials over symmetric aperture shapes, e.g., the square or the hexagon. However, for applications such as WILLIAM and the Calomel crystal, it is required the orthonormal polynomials of a general regular polygon. Moreover, it is required an analytic solution for odd-sided regular aperture shapes such as pentagons, heptagons, and nonagons. However, the analytic solution of odd-sided (x and y non-symmetrical N-gon) aperture shapes produces laborious, complex polynomials. It is therefore

(a) The pentagonal aperture.   (b) The heptagonal aperture.   (c) The nonagonal aperture.

Figure 3.4: An example ofWILLIAM lenses: (**a**) The pentagon lens aperture (Canon EF 50 mm f/1,8 II), (**b**) the heptagon lens aperture (Nikkor AF-S 18-70 mm f/3,5-4,5 DX) and (**c**) the nonagon lens aperture (Nikkor AF 85 mm f/1,8 D).

analyzed a numerical solution of the orthonormalization process, and it is proposed as an efficient numerical approximation of the orthonormal polynomials for general aperture shapes including non-symmetrical, odd-sided aperture shapes. Table 3.1 lists 45 circle Zernike polynomials up to 8th order aberrations and relates the two indices Z_n^m polynomials and single index Z_j polynomials. The Z_j follows Mahajan's single index scheme.

Table 3.1: Table of Zernike circle polynomials $Z_n^m(x, y)$, related notation $Z_j(x, y)$ according to Mahajan in Cartesian coordinates, where $\rho^2 = x^2 + y^2$.

$Z_n^m(x, y)$	$Z_j(x, y)$	Polynomial
Z_0^0	Z_1	1
Z_1^1	Z_2	$2x$
Z_1^{-1}	Z_3	$2y$
Z_2^0	Z_4	$\sqrt{3}(2\rho^2 - 1)$
Z_2^{-2}	Z_5	$2\sqrt{6}xy$
Z_2^2	Z_6	$\sqrt{6}(x^2 - y^2)$
Z_3^{-1}	Z_7	$\sqrt{8}y(3\rho^2 - 2)$
Z_3^1	Z_8	$\sqrt{8}x(3\rho^2 - 2)$
Z_3^{-3}	Z_9	$\sqrt{8}y(3x^2 - y^2)$
Z_3^3	Z_{10}	$\sqrt{8}x(x^2 - 3y^2)$
Z_4^0	Z_{11}	$\sqrt{5}(6\rho^4 - 6\rho^2 + 1)$
Z_4^2	Z_{12}	$\sqrt{10}(x^2 - y^2)(4\rho^2 - 3)$
Z_4^{-2}	Z_{13}	$2\sqrt{10}xy(4\rho^2 - 3)$
Z_4^4	Z_{14}	$\sqrt{10}(\rho^4 - 8x^2y^2)$
Z_4^{-4}	Z_{15}	$4\sqrt{10}xy(x^2 - y^2)$
Z_5^1	Z_{16}	$\sqrt{12}x(10\rho^4 - 12\rho^2 + 3)$
Z_5^{-1}	Z_{17}	$\sqrt{12}y(10\rho^4 - 12\rho^2 + 3)$
Z_5^3	Z_{18}	$\sqrt{12}x(x^2 - 3y^2)(5\rho^2 - 4)$
Z_5^{-3}	Z_{19}	$\sqrt{12}y(3x^2 - y^2)(5\rho^2 - 4)$
Z_5^5	Z_{20}	$\sqrt{12}x(16x^4 - 20(x^2)\rho^2 + 5\rho^4)$
Z_5^{-5}	Z_{21}	$\sqrt{12}y(16y^4 - 20y^2\rho^2 + 5\rho^4)$
Z_6^0	Z_{22}	$\sqrt{7}(20\rho^6 - 30\rho^4 + 12\rho^2 - 1)$
Z_6^{-2}	Z_{23}	$2\sqrt{14}xy(15\rho^4 - 20\rho^2 + 6)$
Z_6^2	Z_{24}	$\sqrt{14}(x^2 - y^2)(15\rho^4 - 20\rho^2 + 6)$

Continued on next page

Table 3.1 – continued from previous page

$Z_n^m(x,y)$	$Z_j(x,y)$	Polynomial
Z_6^{-4}	Z_{25}	$4\sqrt{14}xy(x^2-y^2)(6\rho^2-5)$
Z_6^4	Z_{26}	$\sqrt{14}(8x^4-8x^2\rho^2+rho^4)(6\rho^2-5)$
Z_6^{-6}	Z_{27}	$\sqrt{14}xy(32x^4-32x^2\rho^2+6\rho^4)$
Z_6^6	Z_{28}	$\sqrt{14}(32x^6-48x^4\rho^2+18x^2\rho^4-\rho^6)$
Z_7^{-1}	Z_{29}	$4y(35\rho^6-60\rho^4+30\rho^2-4)$
Z_7^1	Z_{30}	$4x(35\rho^6-60\rho^4+30\rho^2-4)$
Z_7^{-3}	Z_{31}	$4y(3x^2-y^2)(21\rho^4-30\rho^2+10)$
Z_7^3	Z_{32}	$4x(x^2-3y^2)(21\rho^4-30\rho^2+10)$
Z_7^{-5}	Z_{33}	$4(7\rho^2-6)(4x^2y(x^2-y^2)+y(\rho^4-8x^2y^2))$
Z_7^5	Z_{34}	$4(7\rho^2-6)(x(\rho^4-8x^2y^2)-4xy^2(x^2-y^2))$
Z_7^{-7}	Z_{35}	$8x^2y(3\rho^4-16x^2y^2)+4y(x^2-y^2)(\rho^4-16x^2y^2)$
Z_7^7	Z_{36}	$4x(x^2-y^2)(\rho^4-16x^2y^2)-8xy^2(3\rho^4-16x^2y^2)$
Z_8^0	Z_{37}	$3(70\rho^8-140\rho^6+90\rho^4-20\rho^2+1)$
Z_8^2	Z_{38}	$\sqrt{18}(56\rho^6-105\rho^4+60\rho^2-10)(x^2-y^2)$
Z_8^{-2}	Z_{39}	$2\sqrt{18}xy(56\rho^6-105\rho^4+60\rho^2-10)$
Z_8^4	Z_{40}	$\sqrt{18}(28\rho^4-42\rho^2+15)(\rho^4-8x^2y^2)$
Z_8^{-4}	Z_{41}	$4\sqrt{18}xy(28\rho^4-42\rho^2+15)(x^2-y^2)$
Z_8^6	Z_{42}	$\sqrt{18}(7x^6-105x^4y^2+105x^2y^4-7y^6-8x^8\ldots$ $+112x^6y^2-112x^2y^6+8y^8)$
Z_8^{-6}	Z_{43}	$\sqrt{18}(-42x^5y+140x^3y^3-42xy^5+48x^7y\ldots$ $-112x^5y^3-112x^3y^5+48xy^7)$
Z_8^8	Z_{44}	$\sqrt{18}(x^8-28x^6y^2+70x^4y^4-28x^2y^6+y^8)$
Z_8^{-8}	Z_{45}	$\sqrt{18}(-8x^7y+56x^5y^3-56x^3y^5+8xy^7)$

3.4 N-gon basis decomposition to Zernike polynomials

As mentioned, a wavefront aberration $W(x, y)$ over a circular aperture of unit radius can be expanded as the sum of the Zernike polynomials [15, 42, 76–78, 86], as

$$W(x, y) = \sum_{j=1}^{J} a_j Z_j(x, y), \tag{3.16}$$

using single index scheme, where j is the order of the polynomial (according to Table 3.1) of J circle polynomials, and a_j is the coefficient of the Z_j mode in the expansion. Using of the single index is appropriate for decomposition of the circular polynomials to another aperture shapes. The generalized aperture function is described by Equation (3.4).

Because the circular Zernike polynomials do not fulfill the orthogonal condition over a non-circular aperture, the wavefront aberration over a general polygon must be written as the expansion

$$W(x, y) = \sum_{j=1}^{J} a_j P_j(x, y), \tag{3.17}$$

where $P_j(x, y)$ are orthonormal polynomials obtained as the expansion

$$P_j(x, y) = \sum_{j=1}^{J} g_j Z_j(x, y), \tag{3.18}$$

where g_j is the weight of the relevant Zernike polynomial $Z_j(x, y)$. The orthonormality condition of polynomials $P_j(x, y)$ is described as

$$\frac{1}{A} \int_{N-gon} P_j(x, y) P_{j'}(x, y) dx dy = \delta_{jj'}, \tag{3.19}$$

where $\delta_{jj'}$ is the Kronecker delta function. The area A of the N-gon inscribed inside a unit circle is represented by

$$A = \frac{R^2 N \sin \frac{2\pi}{N}}{2}, \tag{3.20}$$

where R is the radius equal to 1, and N is the number of vertices. As described in [33], the GSOP [80] can be used to obtain the orthonormal polynomials $P_j(x, y)$ from the circle Zernike polynomials $Z_j(x, y)$, e.g.

$$P_{j+1}(x,y) = \frac{G_{j+1}(x,y)}{\|G_{j+1}(x,y)\|} = \frac{G_{j+1}(x,y)}{\left[\frac{1}{A}\int_{N-gon} G_{j+1}^2(x,y)dxdy\right]^{1/2}}, \tag{3.21}$$

where

$$G_{j+1}(x,y) = \sum_{k=1}^{j} d_{j+1,k}(x,y)P_k(x,y) + Z_{j+1}(x,y), \quad j \in \langle 1,2,...,J\rangle, \tag{3.22}$$

$$G_1(x,y) = Z_1(x,y) = 1, \tag{3.23}$$

$$d_{j+1,k}(x,y) = -\frac{1}{A}\int_{N-gon} Z_{j+1}(x,y)P_k(x,y)dxdy. \tag{3.24}$$

It is evident that $d_{j+1,k}(x,y)$, $P_{j+1}(x,y)$ and $G_{j+1}(x,y)$ polynomials are obtained recursively. When the $d_{j+1,k}(x,y)$ polynomial is equal to zero, the relevant Zernike polynomial is not dependent, and g_j is therefore equal to zero.

The equations described above contain an integral over an N-gon with N-vertices. The analytic solution begins with the expression of $(s_i, c_i) \in (x,y)$ positions of the vertices as

$$s_i = R\sin\left(\frac{2\pi i}{N}\right), \tag{3.25a}$$

$$c_i = R\cos\left(\frac{2\pi i}{N}\right), \tag{3.25b}$$

where s_i and c_i are coordinates of the indexed vertex $i \in \langle 1,2,...,N\rangle$ and the symbols $(A, B, C, ..., Z)$ are used for labeling N vertices. The indexing of the vertices is illustrated in Figure 3.5 to Figure 3.9. The next step is to express the integration limits of the N-gon. Let's assume that the N-gon is described by a set of linear functions

$$y_i = n_i x_i + q_i, \quad i \in \langle 1,2,...,N\rangle, \tag{3.26}$$

where y and x are Cartesian coordinates, n is the slope, and q is the y-intercept of a linear function. Then, using s_i and c_i vertex positions, it can be obtained

$$n_i = \frac{c_i - c_{i-1}}{s_i - s_{i-1}}, \quad \text{where} \quad \begin{matrix} s_{i-1} = s_N \\ c_{i-1} = c_N \end{matrix} \quad , \quad \text{if } i = 1, \tag{3.27}$$

$$q_i = c_{i-1} - n_i s_{i-1}, \quad \text{where} \quad \begin{matrix} s_{i-1} = s_N \\ c_{i-1} = c_N \end{matrix} \quad , \quad \text{if } i = 1. \tag{3.28}$$

Substituting Equation (3.27) and Equation (3.28) into Equation (3.26), the N-gon limits illustrated in Figure 3.7 to Figure 3.9 are obtained as numbered sides $\langle 1, 2, ..., N \rangle$ of the N-gon. Then the N-gon is divided into sections illustrated by dashed lines. The number of sections is given by

$$M = \left\lfloor \frac{N}{2} \right\rfloor. \tag{3.29}$$

Then we can write

$$d_{j+1,k}(x,y) = \underbrace{\int_{\frac{y-q_N}{n_N}}^{\frac{y-q_1}{n_1}} \int_{s_1}^{s_N} Z_{j+1}(x,y) P_k(x,y) dx dy}_{I_1} + \cdots$$

$$\cdots \underbrace{\sum_{m=2}^{M} \int_{\frac{y-q_o}{n_o}}^{\frac{y-q_m}{n_m}} \int_{s_m}^{s_{m-1}} Z_{j+1}(x,y) P_k(x,y) dx dy}_{I_m}, \tag{3.30}$$

where the index $o = N + 1 - m$. Equation (3.30) has two parts. The part labeled as I_1 describes the integral over the top triangle of the polygon. The second part of Equation (3.30), labeled as I_m, describes the sum of the integrals over the remaining sections of the polygon. Figure 3.5 shows an example of the division of a nonagon into four sections. Similarly to separation in Equation (3.30), the integral inside Equation (3.21) can be expressed as
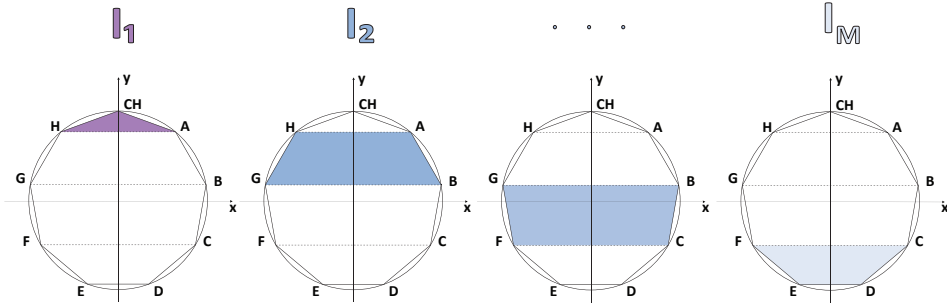
Figure 3.5: An example of nonagonal polygon section division used as the limits of the integration. The nonagon is divided into 4 sections (Equation (3.29)) and the boundaries are used in Equation (3.30) and Equation (3.31).

$$
\int_{N-gon} G_{j+1}^2(x,y)dxdy = \int_{\frac{y-q_N}{n_N}}^{\frac{y-q_1}{n_1}} \int_{s_1}^{s_N} G_{j+1}^2(x,y)dxdy \ + \cdots
$$

$$
\cdots \sum_{m=2}^{M} \int_{\frac{y-q_o}{n_o}}^{\frac{y-q_m}{n_m}} \int_{s_m}^{s_{m-1}} G_{j+1}^2(x,y)dxdy.
$$

(3.31)

Then $G_j(x,y)$ and $P_j(x,y)$ polynomials up to J can be recursively to obtained. Using the procedure described above, we can obtain orthonormal polynomials for a generalized N-gon. The results for square and hexagonal polynomials obtained by this procedure are in good agreement with Mahajan's results for square and hexagonal aperture shapes [33]. However, we should pay attention to the orientation of the polygon. The procedure always orients the polygon in such a way that the top vertex is $(0,1)$ in Cartesian coordinates. Rotating the polygon to another orientation causes changes in polynomials containing cos or sin. The next section provides the results for pentagonal, heptagonal and nonagonal aperture polynomials.

3.5 N-gon polynomials

The procedure mentioned above describes the GSOP [80,87]. By using this process, we can obtain an analytical solution for a square aperture and a hexagonal aperture that is in good agreement with the results for Mahajan's hexagonal and square polynomials [33]. However, an analytic solution for a pentagonal, heptagonal and nonagonal polygon is more complex. This is due to their non-symmetry along the x and y axis. As a consequence, the calculation of the higher order polynomials becomes ineffective, computationally complex and time-consuming. The polynomials of the pentagon, heptagon, and nonagon are therefore given in analytical form up

to P_{11}, H_9 and N_{10}, and these polynomials with $j > (11, 9, 10)$ are written only in the form of expressions of finite precision, because of the increasing complexity. An analysis of the consequences of using finite numeric precision follows. Figure 3.6 illustrates all mentioned aperture shapes Coma interferograms (red), The 10λ Coma PSF (violet) and corresponding PSF of the aberration-free system. It can be seen that odd-sided aperture shapes provide PSF with multiple arms and these PSFs are more similar to circle aperture PSF. The next subsection begins with a description and an enumeration of the pentagonal polynomials.
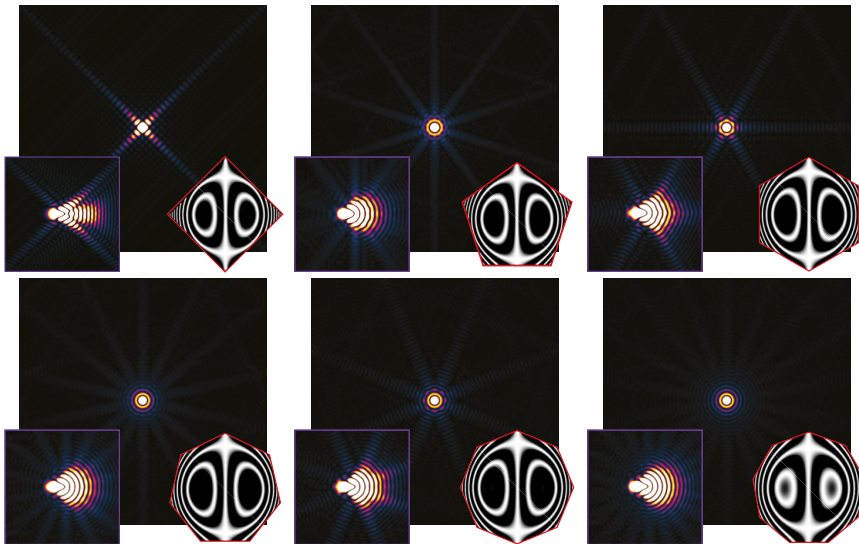
Figure 3.6: The example of the square, pentagon, hexagon, heptagon, octagon and nonagon aberration-free PSF, 3λ Coma PSF and interferogram of Coma aberration.

3.5.1   Pentagonal aperture

Figure 3.7 illustrates the coordinate system of a pentagon with its center at $O(0, 0)$, enumeration of the sides, labeling of the vertices and division of the N-gon into sections (dashed lines). As can be seen, the pentagonal pupil can be divided by the line labeled as F into two sections, consisting of the top triangle DAE and the bottom trapezoid CBAD. The integration is then carried out over these two regions, with the limits given by Equation (3.26).

It can be seen from Table 3.2 that all $P_j(x, y)$ polynomials are dependent on each other, except for $P_1(x, y), P_2(x, y), P_3(x, y), P_5(x, y)$ and $P_6(x, y)$. Table 3.2 lists only primary aberrations up to $P_{11}(x, y)$. They are written in their numerical form, due to the complexity of the coefficients. However, a publicly available Dataset 1 (Ref. [69]), contains all pentagonal polynomials up to $P_{45}(x, y)$ and their numerical form is expressed in Table A.2. Pentagonal polynomials up to $P_{11}(x, y)$ are provided in analytical form. Polynomials where $j > 11$ are provided in their numerical form,

i.e. they are expressed with finite precision. Section 3.6 provides an analysis of the use of finite precision.
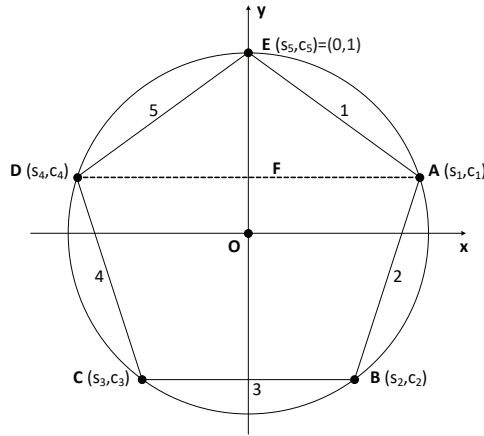
Figure 3.7: A unit pentagon in the Cartesian coordinate system inscribed inside a unit circle.

Table 3.2: Zernike circle polynomials $Z_j(x,y)$ and pentagon polynomials $P_j(x,y)$ in Cartesian coordinates, where $\rho^2 = x^2 + y^2$.

j	$Z_j(x,y)$	$P_j(x,y)$	Aberration
1	1	$\mathbf{1}$	Piston
2	$2x$	$\mathbf{1.1398 Z_2}$	x Tilt
3	$2y$	$\mathbf{1.1398 Z_3}$	y Tilt
4	$\sqrt{3}(2\rho^2 - 1)$	$\mathbf{0.5007 Z_1 + 1.2551 Z_4}$	Defocus
5	$2\sqrt{6}xy$	$\mathbf{1.2878 Z_5}$	Astigmatism at 45°
6	$\sqrt{6}(x^2 - y^2)$	$\mathbf{1.2878 Z_6}$	Astigmatism at 0°
7	$\sqrt{8}y(3\rho^2 - 2)$	$\mathbf{0.8252 Z_3 + 1.3473 Z_7}$	y Coma
8	$\sqrt{8}x(3\rho^2 - 2)$	$\mathbf{0.8252 Z_2 + 1.3473 Z_8}$	x Coma
9	$\sqrt{8}y(3x^2 - y^2)$	$\mathbf{-0.4142 Z_6 + 1.5144 Z_9}$	y Trefoil
10	$\sqrt{8}x(x^2 - 3y^2)$	$\mathbf{-0.4142 Z_5 + 1.5144 Z_{10}}$	x Trefoil
11	$\sqrt{5}(6\rho^4 - 6\rho^2 + 1)$	$\mathbf{0.7142 Z_1 + 0.9995 Z_4 + 1.3696 Z_{11}}$	Primary spherical

3.5.2 Heptagonal aperture

As was mentioned above, a heptagonal aperture is often used in ordinary camera lenses. Figure 3.8 shows that the lines labeled H and I can divide the heptagon into the three sections, consisting of the top triangle FAG, the middle trapezoid EBAF, and the bottom trapezoid DCBE. The integration is then carried out over these three regions, with the limits described by Equation (3.26).

The resulting polynomials listed in Table 3.3 show a different kind of polynomial dependency. Only $Hp_4(x,y), H_7(x,y), H_8(x,y)$ and $Hp_{11}(x,y)$ contain another polynomial. All other heptagon polynomials listed in Table 3.3 stand alone. Table 3.3 lists only primary aberrations up to $Hp_{11}(x,y)$. They are written in their

35

numerical form, due to the complexity of the coefficients. However, the publicly available Dataset 1 (Ref. [69]) contains all heptagon polynomials up to $Hp_{45}(x, y)$ and their numerical form is expressed in Table A.4. Heptagon polynomials up to $Hp_9(x, y)$ are provided in their analytical form. Polynomials where $j > 9$ are provided in their numerical form, i.e., they are expressed with finite precision.
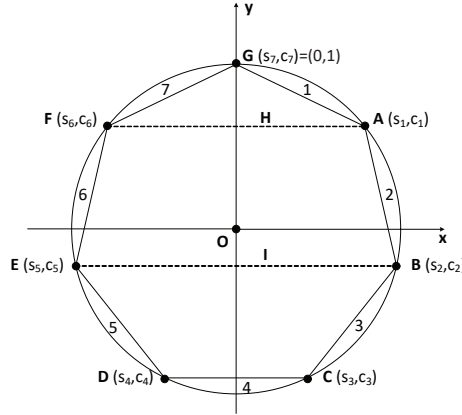
Figure 3.8: A unit heptagon in the Cartesian coordinate system inscribed inside a unit circle.

Table 3.3: Zernike circle polynomials $Z_j(x, y)$ and heptagon polynomials $Hp_j(x, y)$ in Cartesian coordinates, where $\rho^2 = x^2 + y^2$.

j	$Z_j(x, y)$	$Hp_j(x, y)$	Aberration
1	1	**1**	Piston
2	$2x$	$\mathbf{1.0694 Z_2}$	x Tilt
3	$2y$	$\mathbf{1.0694 Z_3}$	y Tilt
4	$\sqrt{3}(2\rho^2 - 1)$	$\mathbf{0.2465 Z_1 + 1.1342 Z_4}$	Defocus
5	$2\sqrt{6}xy$	$\mathbf{1.1412 Z_5}$	Astigmatism at $45°$
6	$\sqrt{6}(x^2 - y^2)$	$\mathbf{1.1411 Z_6}$	Astigmatism at $0°$
7	$\sqrt{8}y(3\rho^2 - 2)$	$\mathbf{0.4121 Z_3 + 1.1952 Z_7}$	y Coma
8	$\sqrt{8}x(3\rho^2 - 2)$	$\mathbf{0.4121 Z_2 + 1.1952 Z_8}$	x Coma
9	$\sqrt{8}y(3x^2 - y^2)$	$\mathbf{1.2152 Z_9}$	y Trefoil
10	$\sqrt{8}x(x^2 - 3y^2)$	$\mathbf{1.2152 Z_{10}}$	x Trefoil
11	$\sqrt{5}(6\rho^4 - 6\rho^2 + 1)$	$\mathbf{0.3621 Z_1 + 0.5489 Z_4 + 1.2385 Z_{11}}$	Primary spherical

3.5.3 Nonagonal aperture

A nonagonal aperture - a nine-bladed aperture - can be found in the higher class of camera lenses. Figure 3.9 illustrates the coordinate system that is used for the nonagon. Lines labeled J, K and L divide the nonagon into four sections, consisting of the top triangle HAI, the trapezoid GBAH, the trapezoid FCBG, and the bottom trapezoid EDCF.

As can be seen from Table 3.4, the resulting polynomials $N_j(x,y)$ indicate a kind of dependence similar to that for heptagonal polynomials. Thus, $N_4(x,y)$, $N_7(x,y)$, $N_8(x,y)$ and $N_{11}(x,y)$ contain another polynomial. All other listed nonagonal polynomials stand alone. Table 3.4 lists only primary aberrations up to $N_{11}(x,y)$. They are written in their numerical form, due to the complexity of the coefficients. However, the publicly available '.mat' Dataset 1 (Ref. [69]) contains all heptagonal polynomials up to $N_{45}(x,y)$ and their numerical form is expressed in Table A.6. Heptagonal polynomials up to $N_{10}(x,y)$ are provided in their analytical form. Polynomials where $j > 10$ are provided in their numerical form, i.e., they are expressed with finite precision.
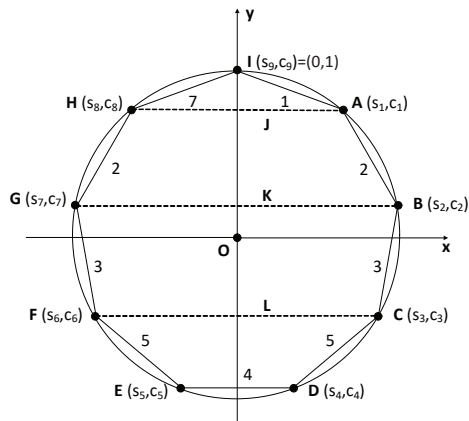
Figure 3.9: A unit nonagon in the Cartesian coordinate system inscribed inside a unit circle.

Table 3.4: Zernike circle polynomials $Z_j(x,y)$ and nonagon polynomials $N_j(x,y)$ in terms of circular polynomials in Cartesian coordinates, where $\rho^2 = x^2 + y^2$.

j	$Z_j(x,y)$	$N_j(x,y)$	Aberration
1	1	**1**	Piston
2	$2x$	$\mathbf{1.0414 Z_2}$	x Tilt
3	$2y$	$\mathbf{1.0414 Z_3}$	y Tilt
4	$\sqrt{3}(2\rho^2 - 1)$	$\mathbf{0.1460 Z_1 + 1.0814 Z_4}$	Defocus
5	$2\sqrt{6}xy$	$\mathbf{1.0838 Z_5}$	Astigmatism at 45°
6	$\sqrt{6}(x^2 - y^2)$	$\mathbf{1.0838 Z_6}$	Astigmatism at 0°
7	$\sqrt{8}y(3\rho^2 - 2)$	$\mathbf{0.2430 Z_3 + 1.1206 Z_7}$	y Coma
8	$\sqrt{8}x(3\rho^2 - 2)$	$\mathbf{0.2430 Z_2 + 1.1206 Z_8}$	x Coma
9	$\sqrt{8}y(3x^2 - y^2)$	$\mathbf{1.1271 Z_9}$	y Trefoil
10	$\sqrt{8}x(x^2 - 3y^2)$	$\mathbf{1.1271 Z_{10}}$	x Trefoil
11	$\sqrt{5}(6\rho^4 - 6\rho^2 + 1)$	$\mathbf{0.2082 Z_1 + 0.3306 Z_4 + 1.1541 Z_{11}}$	Primary spherical

3.6   An analysis of the finite precision calculation

Previous sections have mentioned issues in expressing the analytical form of the odd-sided N-gon polynomials. The use of symbolic expressions when calculating higher order orthonormal polynomials is highly demanding and inefficient. Numerical finite precision expressions solve this issue. However, the sufficient precision has to be considered, i.e., the number of digits in the polynomial coefficients. It has been prepared series of calculations, in which can be observed the dependence of the orthonormality on the decimal precision, see Figure 3.10. The second series of calculations compares the wavefronts of the analytical form polynomials with the wavefronts obtained from the numerical form polynomials.
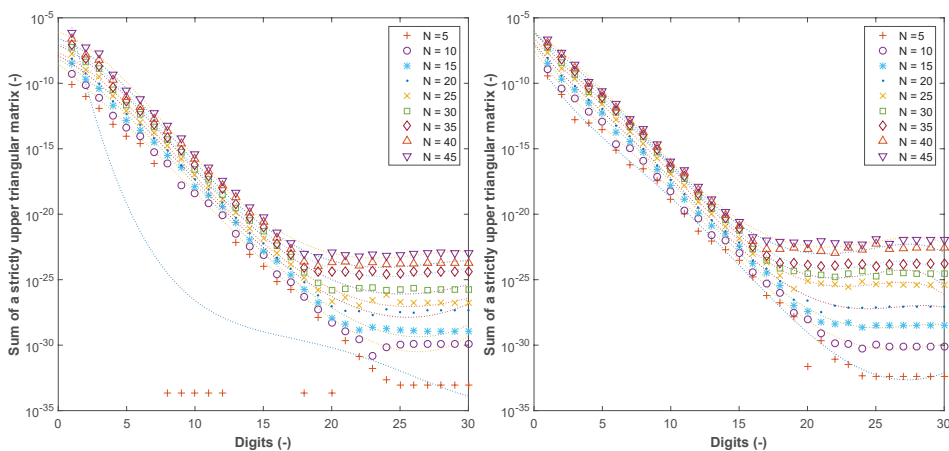
(a) The square aperture.

(b) The pentagonal aperture.

(c) The hexagonal aperture.

(d) The heptagonal aperture.
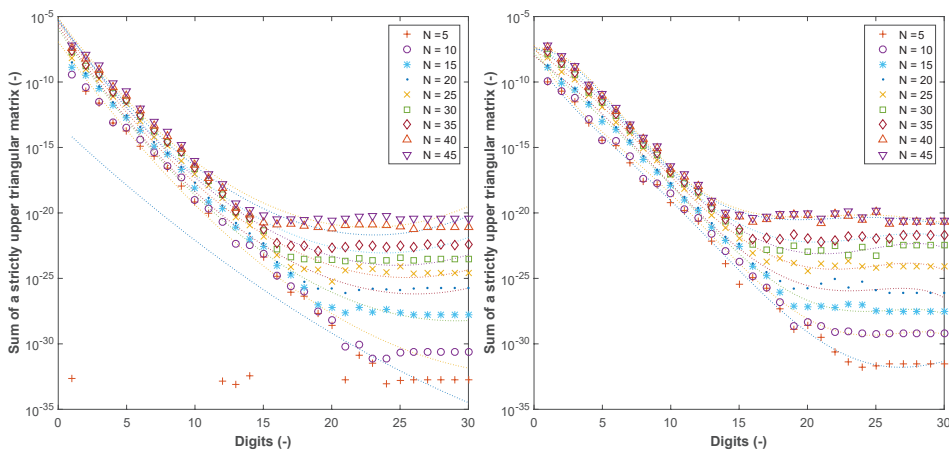
(e) The octagonal aperture.

(f) The nonagonal aperture.
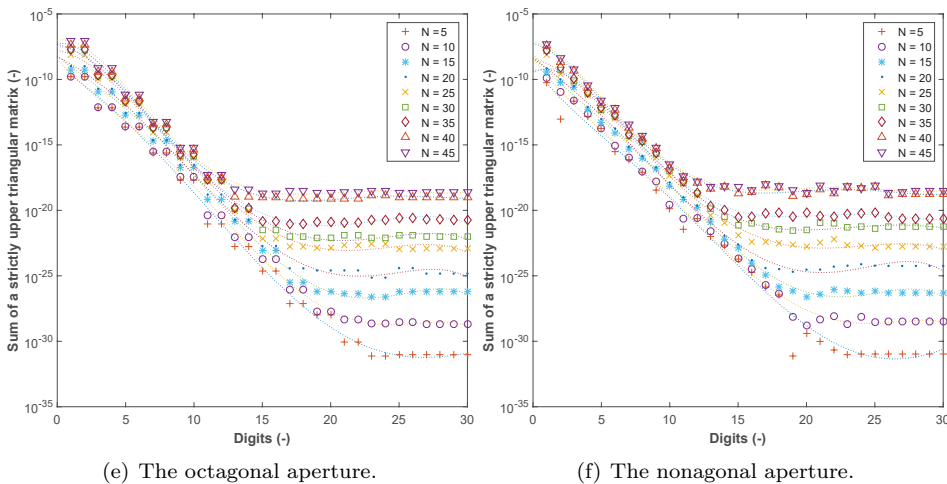
Figure 3.10: An analysis of enumerated cross-polynomial matrix U according to Equation (3.19) and Equation (3.32). The resulting matrix should satisfy Equation (3.19), i.e. $\delta_{jj'} = 0$ for $j \neq j'$ and 1 for $j = j'$. The y axis has a logarithmic scale.

Figure 3.10 shows graphs enumerated for square, pentagonal, hexagonal, heptagonal, octagonal and nonagonal aperture shapes. The even-sided N-gons were enumerated for the purposes of comparison. The GSOP requires that the condition given by Equation (3.19), be met, where the Kronecker delta function is equal to 1, when two involved polynomials have the same index ($j = j'$), and 0 else. However, the numerical form of the N-gon polynomials does not fully satisfy the condition given by Equation (3.19). The matrices of the N-gon numerical polynomials have 1 on the diagonal, but the matrices contain small values ($10^{-30} < k_{jj'} < 10^{-5}$) off-diagonal. We therefore introduce

$$\frac{1}{A} \int_{N-gon} P_j(x,y) P_{j'}(x,y) dx dy = k_{jj'},$$
(3.32)

where function $k_{jj'}$ has a value of 1 on diagonal and values of ≈ 0 off-diagonal. Using Equation (3.32) over all N-gon polynomials, the cross-polynomial matrix U is obtained with 1 on the diagonal and $k_{jj'}$ anywhere else. This matrix can be described as

$$U = \begin{bmatrix} 1 & k_{1,2} & \cdots & k_{1,n} \\ k_{2,1} & 1 & \cdots & k_{2,n} \\ \vdots & \vdots & \ddots & \vdots \\ k_{1,n} & k_{2,n} & \cdots & 1 \end{bmatrix}.$$
(3.33)

39

Then we can write

$$u = \frac{1}{2}\sum_{j=1}^{N}\sum_{j'}^{N}k_{jj'} - \sum_{j=1}^{N}\sum_{j'}^{N}\delta_{jj'}, \tag{3.34}$$

where u is the sum of the off-diagonal values and N describes the number of polynomials involved. Then they were enumerated the cross-polynomial matrices U of all mentioned aperture shapes and obtained the sum defined by Equation (3.34). The values obtained by summing the off-diagonal values define the amount of mutual energy of the polynomials for $j \neq j'$. As can be seen from Figure 3.10, the matrices of all aperture shapes were enumerated for the $N = 5$ to $N = 45$ involved polynomials with the precision of 1 to 30 decimal points. Involving only 5 polynomials increases the precision efficiency, and these polynomials give a residuum less than 10^{-30}. Increasing the number of involved polynomials to $N = 45$ reveals decreasing efficiency, and these polynomials stop reducing the orthonormality residuum at around 10^{-20}. Involving fewer polynomials (lower order polynomials) implies using greater precision, i.e., more decimal places. This analysis concludes that the use of more than 25 digits does not improve the results of a cross-polynomial orthonormality check. It is therefore sufficient and computationally efficient to use 25-digit precision.

As has been introduced above, the second analysis is devoted to differences between the wavefront enumerated by analytical polynomials and by numerical polynomials. By comparing these two wavefronts, we can obtain the direct difference, and we can calculate the Root Mean Square Error (RMSE) of the differential wavefront. The wavefronts of 4 to 9 gons were calculated from polynomials with $j = 1$ up to $j = 11$, i.e. the primary aberrations, see Figure 3.11. For the case of the heptagon this comparison is up to $j = 9$, and for the nonagon, the comparison is up to $j = 10$.

(a) The square aperture.   (b) The pentagonal aperture.

(c) The hexagonal aperture.

(d) The heptagonal aperture.
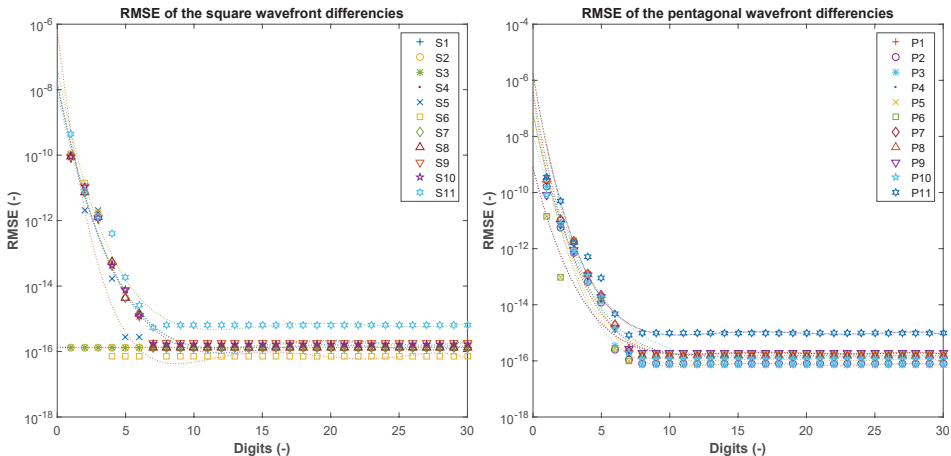
(e) The octagonal aperture.

(f) The nonagonal aperture.
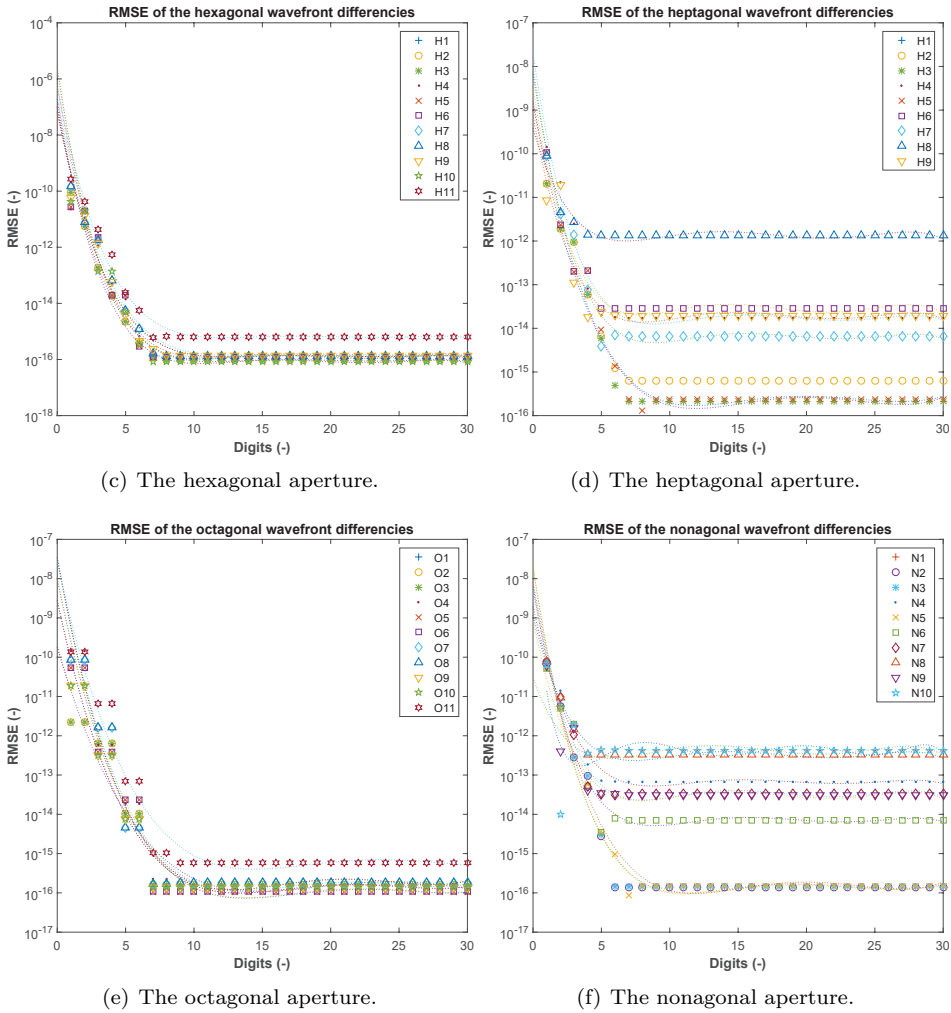
Figure 3.11: The differences between wavefronts calculated from analytical polynomials and the numerical polynomials. The y-axis has a logarithmic scale.

Figure 3.11 shows that the differences in the wavefronts of all aperture shapes change up to the level of 10 digits. Then, the differences between the more complex analytical form and the numerical form of the polynomials achieve values of around 10^{-15} for the heptagon and 10^{-12} for the nonagon. The use of more than 10 digits does not improve the results, and the residuum remains constant. However, it can be seen that the direct difference between the analytical wavefront and numerical polynomial wavefront shows great similarity.

The last graph compares the values of the cross-polynomials given by Equation 3.34 for the analytical polynomials and the values given by the numerical polynomials. As can be seen from Figure 3.12, where the red bars represent analytical

polynomials, the matrix of the square, the hexagon, and the octagon contain 0 off-diagonal values, i.e., they are orthonormal. However, the matrices of the pentagon, the heptagon, and the nonagon contain very small ($< 10^{-68}$) off-diagonal values, even for the analytical polynomials. The blue bars represent numerical polynomials, and it can be seen that the values of their off-diagonal coefficients achieve $10^{-21}; 10^{-25}$. This graph provides a direct comparison of the analytical and numerical polynomials. It can be seen that, especially for odd-sided N-gons, the numerical polynomials provide an appropriate and efficient solution.
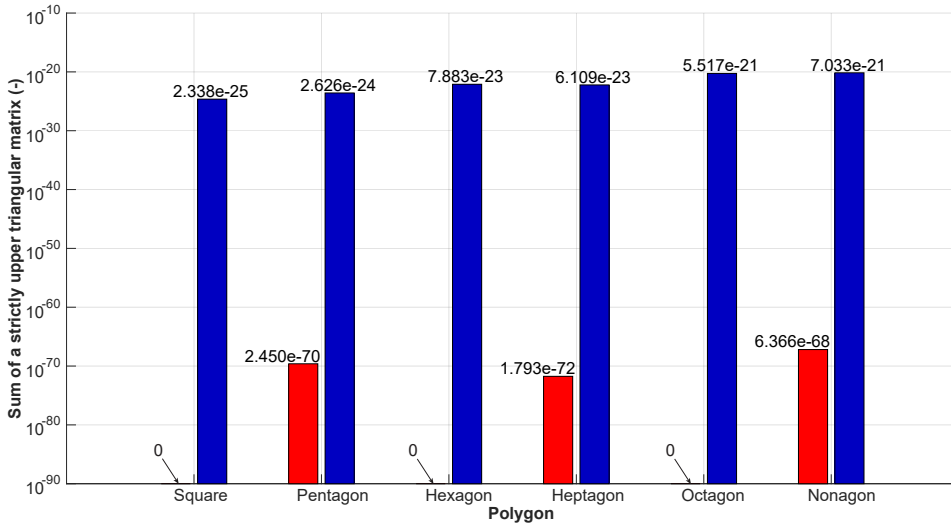
Figure 3.12: A graph comparing the cross-polynomial matrix of the analytical polynomials (red) and the numerical polynomials (blue). The y-axis has a logarithmic scale.

Following up on previous works mentioned above, the orthonormal polynomials of hexagonal and square aperture shapes has been verified by the orthonormal polynomials of these aperture shapes provided in [33], and they are in good agreement. The polynomials can be expressed for any regular N-gon on the basis of the Gram-Schmidt orthogonalization process. As an example, it is proposed the orthonormal polynomials of pentagonal, heptagonal and nonagonal lens apertures. Because of the complexity of odd-sided N-gon analytical polynomials, an orthonormality analysis of numerical polynomials (the numerical form of the analytical polynomials) was performed. The analysis showed the influence of the decimal precision. The second analysis showed the dependency of numerical precision on the wavefront divergence against the analytically enumerated wavefront. This analysis showed that the numerical form polynomials provide wavefronts similar to those of the analytical polynomials. The final analysis provided by the graph in Figure 3.12 is a combination of the two previous analyses. It compares the analytical and numerical cross-polynomial matrix residuals. While the symmetrical, even-sided N-gons are perfectly orthonormal (the off-diagonal values are 0), the odd-sided polynomials show small residuals, even in their analytical form. N-gons with 4 to 9 sides

were enumerated to show their similarities in some aspects, e.g., their dependency on decimal precision, and their differences when a comparison is made of the orthonormality. Due to the complexity of the odd-sided polynomials, they are used in their numerical form.

Examining Tables 3.2 to 3.4, it can be observed an analogy with the results in [33] for a hexagon. The pentagon needs more polynomials for balancing aberrations, e.g. $P_4, P_6 - P_{11}$, because of the poor approximation of the circle. However, the way that the heptagonal and nonagonal polynomials are balanced is similar to the way that the polynomials of the hexagon provided in [33] are balanced. The process described above, and the enumerated polynomials, can be used for an aberration description of N-gon apertures. Tables of square, pentagon, hexagon, heptagon, octagon and nonagon polynomials in their numerical form up to 8th order are listed in Appendix (Tables A.1, A.2, A.3, A.4, A.5, A.6).

Space-Variant optical model

The following chapter focuses on the introduction of the field dependency of the used polynomials. The first section describes the expressions leading to space-variant polynomials. The SVPSF model proposal follows. Parts of this chapter were published in [42].

4.1 Field Dependency in the image plane

A description of the wavefront aberration of a circular rotationally symmetric optical system can be adopted from [21], originally from [18] as

$$W(\rho, \theta; H, \varphi) = \sum_{p}^{\infty} \sum_{n}^{\infty} \sum_{m}^{\infty} W_{klm} H^k \rho^l \cos^m(\varphi - \theta), \qquad (4.1)$$

where $k = 2p + m$ and $l = 2n + m$. Symbol W_{klm} is used for the expansion coefficients; the coordinates are defined in Figure 3.1c. The field dependency of $a_n^m(H, \varphi)$ can be solved by comparing wavefront aberrations using Equations (3.15) and (4.1) as

$$\sum_{n=0}^{k} \sum_{m=-n}^{n} a_n^m (H, \varphi) Z_n^m(\rho, \varphi - \theta) = \sum_{p}^{\infty} \sum_{n}^{\infty} \sum_{m}^{\infty} W_{klm} H^k \rho^l \cos^m(\varphi - \theta). \qquad (4.2)$$

Equation (4.2) can be obtained by expanding Equation (3.15) and rewriting terms $\cos^m(\theta, \varphi)$ into terms containing a set of goniometric functions $\cos(m\theta)$, $\sin(m\theta)$, $r \in N$ and comparing the coefficients in this form with expanded Zernike polynomials (as in Table 4.1). The resulting coefficients $a_n^m(H, \varphi)$ describing the space variation of Zernike polynomials are presented in [21]. Coefficients W_{klm} are then used for describing the aberration of the space-variant optical system. The order of the aberration terms is defined by Hopkins in [18] as

$$order = (sum\ of\ the\ powers\ of\ \rho\ and\ \theta) - 1. \tag{4.3}$$

4.2   Proposed Method

The method proposed in this paper is based on modeling the PSF of the system, and comparing it with real image data without requiring measurements of the wavefront aberrations. The fitting of the model takes place in the image plane.

There are three conditions for acquiring the set of calibration images. The first criterion is that FWHM of the image of the light source should be sufficient for PSF estimation. The experimental results show that FWHM size greater than 5 px is enough for the algorithm. FWHM of the diffractive image of the source should be smaller than 1 px. Otherwise, the diffractive function has to be added to the model of the system. The image of the 200 μm pinhole has FWHM size 0.6 μm which is less than the size of the pixel of our camera. The influence of the source shape has to be taken into account. The second criterion is the Signal-to-Noise Ratio (SNR), which should be greater than 20 dB. Section 4.4.1 contains a comparison of results obtained with different SNR. The third criterion is that the number of test images depends on the spatial variance of the system, i.e., a heavily distorted optical system will require more test images to satisfy this criterion. We have to choose the distance between two different PSFs in such a way that

$$RMSE_{IN}(f_i, f_{i+1}) = \sqrt{\frac{1}{M \times N} \sum_{u=0}^{N-1} \sum_{v=0}^{M-1} (f_i - f_{i+1})^2} < 5\%, \tag{4.4}$$

where f_i and f_{i+1} are the images of the point light source in the image plane. M and N are the sizes of the f_i and f_{i+1} images. In our example, a grid of 24 positions of the PSFs in one quadrant of the optical system is sufficient to estimate the model. The wavefront is modeled using Zernike polynomials and known optical parameters. In addition to the input image data, we need to know camera sensor parameters such as resolution, the size of the sensor and optical parameters such as the focal length (crop factor, if included), the F-number and the diameter of the exit pupil. The obtained model of the PSF of the optical system is based on the assessment of differential metrics.

We can describe the modeling of real UWFOV systems as a procedure with three main parts: the optical part, the image sensor, and the influence of the sensor noise. The space-variant impulse response $h(u, v; \xi, \eta)$ can include the influence of the image sensor (e.g., pixel shape and sensitivity profile, noise or quantization error). The sensor has square pixels with uniform sensitivity. Then, the PSF of the imaging system can be described as

Table 4.1: The relation between indices and coefficients of the Zernike polynomials.

$Z_n^m(\rho,\theta)$	a_n^m	Expansion Coefficient Function	Name
$Z_0^0(\rho,\theta)$	a_0^0	$\frac{1}{2}\left[\frac{5}{9}W_{0,10,0}+\frac{2}{5}W_{080}+\frac{1}{2}W_{060}+\frac{2}{3}W_{040}+W_{020}+H^6\left(W_{620}+\frac{1}{2}W_{622}\right)\cdots\right.$ $+H^4\left(W_{420}+\frac{1}{2}W_{422}+\frac{2}{3}W_{440}+\frac{1}{3}W_{442}+\frac{1}{4}W_{444}\right)\cdots$ $\left.+H^2\left(W_{220}+\frac{1}{2}W_{222}+\frac{2}{3}W_{240}+\frac{1}{3}W_{242}+\frac{1}{2}W_{260}+\frac{1}{4}W_{262}\right)\right]\cdots$ $+W_{800}H^8+W_{600}H^6+W_{400}H^4+W_{200}H^2+W_{000}$	Piston
$Z_1^1(\rho,\theta)$	a_1^1	$\left[-\frac{16}{35}W_{171}+\frac{1}{2}W_{151}+\frac{2}{3}W_{131}+W_{111}+H^6W_{171}+H^4\left(W_{511}+\frac{2}{3}W_{531}+\frac{1}{2}W_{533}+\right)\cdots\right.$ $\left.+H^2\left(W_{311}+\frac{1}{2}W_{351}-\frac{9}{40}W_{533}+\frac{2}{3}W_{331}+\frac{1}{2}W_{333}+\frac{3}{5}W_{353}\right)\right]H\cos(\varphi)$	Tilt
$Z_1^{-1}(\rho,\theta)$	a_1^{-1}	$\left[-\frac{16}{35}W_{171}+\frac{1}{2}W_{151}+\frac{2}{3}W_{131}+W_{111}+H^6W_{171}+H^4\left(W_{511}+\frac{2}{3}W_{531}+\frac{1}{2}W_{533}+\right)\cdots\right.$ $\left.+H^2\left(W_{311}+\frac{1}{2}W_{351}-\frac{9}{40}W_{533}+\frac{2}{3}W_{331}+\frac{1}{2}W_{333}+\frac{3}{5}W_{353}\right)\right]H\sin(\varphi)$	
$Z_2^0(\rho,\theta)$	a_2^0	$\frac{1}{2}\left[\frac{20}{21}W_{0,10,0}+\frac{4}{5}W_{080}+\frac{9}{10}W_{060}+W_{040}+W_{020}+H^6\left(W_{620}+\frac{1}{2}W_{622}\right)\cdots\right.$ $+H^4\left(W_{420}+\frac{1}{2}W_{422}+W_{440}+\frac{1}{2}W_{442}+\frac{3}{8}W_{444}\right)\cdots$ $\left.+H^2\left(W_{220}+\frac{1}{2}W_{222}+W_{240}+\frac{1}{2}W_{242}+\frac{9}{10}W_{260}+\frac{9}{20}W_{262}\right)\right]$	Focus
$Z_2^2(\rho,\theta)$	a_2^2	$\frac{1}{2}\left[\frac{3}{5}W_{262}+\frac{3}{4}W_{242}+W_{222}+H^4W_{622}+H^2\left(W_{422}+\frac{3}{4}W_{444}+\frac{3}{4}W_{442}\right)\right]H^2\cos(2\varphi)$	Astigmatism
$Z_2^{-2}(\rho,\theta)$	a_2^{-2}	$\frac{1}{2}\left[\frac{3}{5}W_{262}+\frac{3}{4}W_{242}+W_{222}+H^4W_{622}+H^2\left(W_{422}+\frac{3}{4}W_{444}+\frac{3}{4}W_{442}\right)\right]H^2\sin(2\varphi)$	
$Z_3^1(\rho,\theta)$	a_3^1	$\frac{1}{3}\left[\frac{6}{5}W_{171}+\frac{6}{5}W_{151}+W_{131}+H^4\left(W_{531}+\frac{3}{4}W_{533}\right)\cdots\right.$ $\left.+H^2\left(W_{531}+\frac{3}{4}W_{333}+\frac{6}{5}W_{351}+\frac{9}{10}W_{353}\right)\right]H\cos(\varphi)$	Coma
$Z_3^{-1}(\rho,\theta)$	a_3^{-1}	$\frac{1}{3}\left[\frac{6}{5}W_{171}+\frac{6}{5}W_{151}+W_{131}+H^4\left(W_{531}+\frac{3}{4}W_{533}\right)\cdots\right.$ $\left.+H^2\left(W_{531}+\frac{3}{4}W_{333}+\frac{6}{5}W_{351}+\frac{9}{10}W_{353}\right)\right]H\sin(\varphi)$	
$Z_4^0(\rho,\theta)$	a_4^0	$\frac{1}{6}\left[\frac{25}{14}W_{0,10,0}+\frac{12}{7}W_{080}+\frac{3}{2}W_{060}+W_{040}+H^4\left(W_{440}+\frac{1}{2}W_{442}+\frac{3}{8}W_{444}\right)\cdots\right.$ $\left.+H^2\left(W_{240}+\frac{1}{2}W_{242}+\frac{3}{2}W_{260}+\frac{3}{4}W_{262}\right)\right]$	Spherical
$Z_3^3(\rho,\theta)$	a_3^3	$\frac{1}{4}\left(W_{333}+\frac{1}{20}W_{353}+H^2W_{533}\right)H^3\cos(3\varphi)$	Elliptical
$Z_3^{-3}(\rho,\theta)$	a_3^{-3}	$\frac{1}{4}\left(W_{333}+\frac{1}{20}W_{353}+H^2W_{533}\right)H^3\sin(3\varphi)$	Coma
$Z_4^2(\rho,\theta)$	a_4^2	$\frac{1}{4}\left[\frac{1}{2}W_{242}+\frac{2}{3}W_{262}+H^2\frac{1}{2}\left(W_{444}+W_{442}\right)\right]H^2\cos(2\varphi)$	Oblique
$Z_4^{-2}(\rho,\theta)$	a_4^{-2}	$\frac{1}{4}\left[\frac{1}{2}W_{242}+\frac{2}{3}W_{262}+H^2\frac{1}{2}\left(W_{444}+W_{442}\right)\right]H^2\sin(2\varphi)$	Spherical
$Z_5^1(\rho,\theta)$	a_5^1	$\frac{1}{10}\left[\frac{12}{7}W_{171}+W_{151}+H^2\left(W_{351}+\frac{3}{4}W_{353}\right)\right]H\cos(\varphi)$	5th Coma
$Z_5^{-1}(\rho,\theta)$	a_5^{-1}	$\frac{1}{10}\left[\frac{12}{7}W_{171}+W_{151}+H^2\left(W_{351}+\frac{3}{4}W_{353}\right)\right]H\sin(\varphi)$	
$Z_6^0(\rho,\theta)$	a_6^0	$\frac{1}{20}\left[\frac{25}{9}W_{0,10,0}+2W_{080}+W_{060}+H^2\left(W_{260}+\frac{1}{2}W_{262}\right)\right]$	5th Spherical
$Z_5^3(\rho,\theta)$	a_5^3	$\frac{1}{20}W_{353}H^3\cos(3\varphi)$	
$Z_5^{-3}(\rho,\theta)$	a_5^{-3}	$\frac{1}{20}W_{353}H^3\sin(3\varphi)$	
$Z_4^4(\rho,\theta)$	a_4^4	$\frac{1}{8}W_{444}H^4\cos(4\varphi)$	
$Z_4^{-4}(\rho,\theta)$	a_4^{-4}	$\frac{1}{8}W_{444}H^4\sin(4\varphi)$	
$Z_7^1(\rho,\theta)$	a_7^1	$\frac{1}{35}W_{171}H\cos(\varphi)$	
$Z_7^{-1}(\rho,\theta)$	a_7^{-1}	$\frac{1}{35}W_{171}H\sin(\varphi)$	
$Z_6^2(\rho,\theta)$	a_6^2	$\frac{1}{30}W_{262}H^2\cos(2\varphi)$	
$Z_6^{-2}(\rho,\theta)$	a_6^{-2}	$\frac{1}{30}W_{262}H^2\sin(2\varphi)$	
$Z_8^0(\rho,\theta)$	a_8^0	$\frac{1}{28}W_{0,10,0}+\frac{1}{70}W_{080}$	7th Spherical
$Z_{10}^0(\rho,\theta)$	a_{10}^0	$\frac{1}{252}W_{0,10,0}$	9th Spherical

$$h(u, v; \xi, \eta) = h_{opt}(u, v; \xi, \eta) * h_{sen}(u, \ v), \tag{4.5}$$

where $h_{sen}(u, v)$ is the PSF of the sensor and $h_{opt}(u, v; \xi, \eta)$ is the PSF of the optical part. The symbol * describes the convolution. $h_{sen}(u, v)$ can be measured from the sensor, and the influence of the spatial sampling is discussed later. $h_{opt}(u, v; \xi, \eta)$ can be calculated from the system parameters and wavefront deformations using the Fourier transform as described in Equation (3.6). The wavefront deformation is modeled using Zernike polynomials for the target position in the image plane (see Equation (3.15)). Ultra-wide field images typically have angular dependent PSF. High orders of Zernike polynomials are therefore used in the approximation. The wavefront approximation is used up to the 8th order plus the 9[th]spherical aberration of the expansion function. The field dependence of the coefficients is formulated in [21]. In our work, the set of field-dependent coefficients was expanded up to the 8th order plus the 9[th]spherical aberration. Table 4.1 provides the expressions of the used W_{klm} coefficients according to the Zernike polynomials.

Let's assume an imaging system with an unknown aberration model. We then obtain with this system a grid of K test images of point light sources covering the entire FOV as

$$\{f_i(u, v)\}_{i=1}^{K} . \tag{4.6}$$

Then, let

$$\{f_d(\hat{u}, \hat{v})\}_{d=1}^{L} , \tag{4.7}$$

be the d-th realization of the model in the corresponding position in the image as the original object. Sub-matrix f_i is the image of the point light source in the image plane, while matrix f_d is the sub-image model computed by our method. The size of the sub-arrays must be sufficient to cover the whole neighborhood of the point light object on the positions $\{u_{0i}, v_{0i}\}_{i=1}^{K}$.

As was mentioned above, symbols $\hat{u}, \hat{v}$ are used for image plane coordinates in the normalized optimization space, and u, v are image plane coordinates. Note that f_i and f_d can be located at any point over the entire field of view. The step between the positions of the point light source has to be chosen to cover the observable difference of the acquired point. The positions of the point light source in the field of view play an important role in the convergence efficiency. In our example, we divided the field of view each 10 degrees uniformly horizontally and vertically. We, therefore, obtain a matrix of PSFs sufficient for a description of the model. It turned out that finer division of the FOV is not necessary and does not improve the accuracy of the model and it satisfies the condition in Equation (4.4).

The algorithm uses two evaluation methods. The first method is based on calculating the RMSE over the difference matrix in Equation (4.10) and optimizing the

Table 4.2: An example of estimated W_{klm} coefficients and resulting set of coefficients. d stands for numbering of a realization.

d	W_{111}	W_{020}	W_{040}	W_{131}	W_{220}	W_{222}	W_{311}	$\cdots$	W_{0100}
1	-1.6308	2.5148	4.6706	1.2561	0.2444	-0.3173	1.8344	$\cdots$	0.0725
2	-1.7982	2.5301	4.6656	1.2627	0.2441	-0.3179	1.2103	$\cdots$	0.0727
3	-1.4990	2.5439	4.9892	1.0591	0.3155	-0.2575	1.2050	$\cdots$	-0.1780
4	-1.7029	2.4587	3.7209	1.8654	0.3559	-0.2148	1.7499	$\cdots$	-0.0686
5	-1.5539	2.6428	4.5441	2.2722	0.3194	-0.1695	1.0072	$\cdots$	-0.0439
6	-1.5539	2.6428	4.5441	2.2722	0.3194	-0.1695	1.0072	$\cdots$	-0.0439
$\vdots$	$\vdots$	$\vdots$	$\vdots$	$\vdots$	$\vdots$	$\vdots$	$\vdots$	$\ddots$	$\vdots$
L	-1.7916	2.6058	4.5781	1.4836	0.3025	-0.2439	1.7116	$\cdots$	-0.0667
Resulting coefficients	-1.6308	2.5301	4.5781	1.2674	0.3025	-0.2439	1.4581	$\cdots$	-0.0596

W_{klm} parameters and the $\Delta\hat{u}, \Delta\hat{v}$ positions for decreasing residuals. The second method is based on deducting the original and model matrix to obtain the Maximum Difference (MD). Then, the residuals of this method indicate the deviation against the original matrix. The first method with RMSE calculation provides a better shape description. However, this method can result in local extremes. The reduction can be resolved by using the MD calculation method. This method minimizes the local extremes, because it is focused on minimizing the maximum difference between the f_i and f_d object matrices, but the output can be a more general shape of PSF.

Let's now introduce operators $RMSE(f_i, f_d)$ and $MD(f_i, f_d)$, which are used as descriptors of the differences between the original PSF and the model of PSF (f_i and f_d).

$$RMSE(f_i, f_d) = \sqrt{\frac{1}{M \times N} \sum_{\tilde{u}=0}^{N-1} \sum_{\tilde{v}=0}^{M-1} (f_i(u,v) - f_d(\hat{u}, \hat{v}))^2}. \qquad (4.8)$$

$$MD(f_i, f_d) = \max_{(u,v)} \left(|f_i(u,v) - f_d(\hat{u}, \hat{v})| \right). \qquad (4.9)$$

M and N are the sizes of the f_i and f_d sub-arrays. The optimization parameter of the W_{klm} coefficients uses the Nelder-Mead optimizing algorithm, which is described in detail in [88]. Let R_{f_i, f_d} be the optimizing operator, then

$$R_{f_i, f_d}(\hat{u}, \hat{v}) = \min_{W_{klm}, \Delta u, \Delta v} \left[RMSE(f_i, f_d) \vee MD(f_i, f_d) \right], \qquad (4.10)$$

The table inside the figure:

d	W131	W040	W020	...
1	3.14	8.94	3.24	...
2	2.75	7.42	1.85	...
⋮	⋮	⋮	⋮	⋮
L-2	2.83	7.82	1.57	...
L-1	2.95	8.41	1.72	...
L	2.73	7.43	1.86	...
median	2.77	7.92	1.67	...
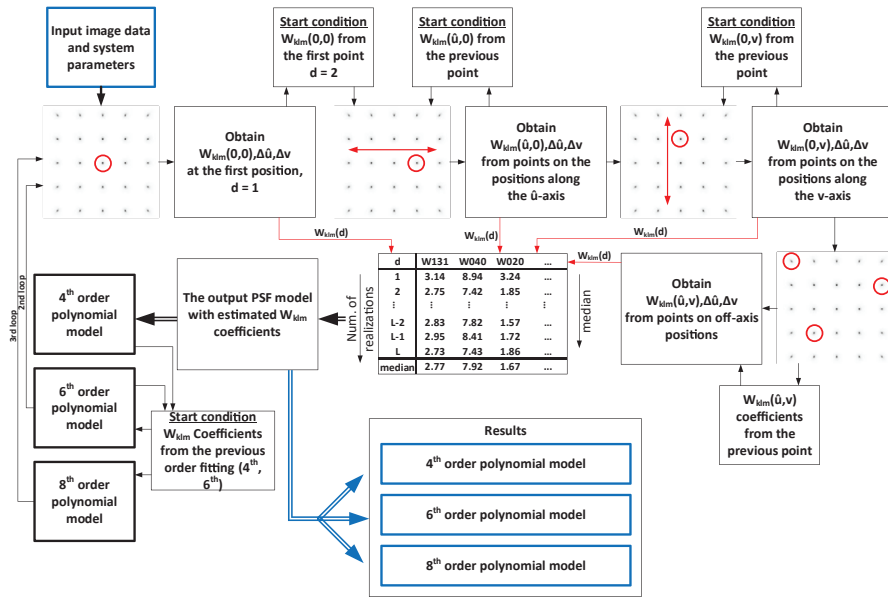
Figure 4.1: Diagram of the proposed algorithm. Note that the W_{klm} coefficients from 4th order estimate are used as a start condition for the 6th order estimate, and the 6th order W_{klm} coefficients are used as a start condition for an estimate of the 8th order W_{klm} coefficients.

where $W_{klm}, \Delta \hat{u}, \Delta \hat{v}$ are variables for minimizing the cost function. For multi-parameter optimization tasks, the challenge is to find the global minimum of the function. Considering this issue, we can find an appropriate set of starting parameters of the fit algorithm by smart selection of on-axis points (PSFs) on which we will obtain appropriate $W_{klm}, \Delta \hat{u}, \Delta \hat{v}$ variables, and we will then increase the precision of our model by selecting off-axis points and improving $W_{klm}, \Delta \hat{u}, \Delta \hat{v}$ variables. The process of point selection is illustrated in Figure 4.1, and the steps in the algorithm are as follows:

- Select a point placed on the optical axis (this point is considered as SV aberration free).

- The W_{klm} optimization coefficient is based on minimizing RMSE or the MD metrics. Then we obtain

$$R_{f_i,f_d}(0,0) \Rightarrow W_{klm}(1), \Delta \hat{u}, \Delta \hat{v}, \tag{4.11}$$

where $W_{klm}(1)$ is the first realization of the fit, and $\Delta \hat{u}, \Delta \hat{v}$ represent the displacement of the object point in the image plane.

- The next calibration point will be placed on the $\hat{u}$-axis and next to the first point.

- All W_{klm} coefficients from the first point fit will be used as start conditions in the next step of the fit.

- In the next step, we will fit all the points along the $\hat{u}$-axis by increasing distance H.

- The previous result is used as the start condition for the next point.

$$R_{f_i, f_d}(\hat{u}, 0) \Rightarrow W_{klm}(d), \Delta\hat{u}, \Delta\hat{v}. \tag{4.12}$$

- Then, we can continue along the $\hat{v}$-axis by increasing distance H. This procedure gives the first view of the model.

$$R_{f_i, f_d}(0, \hat{v}) \Rightarrow W_{klm}(d), \Delta\hat{u}, \Delta\hat{v}, \tag{4.13}$$

where $W_{klm}(d)$ is the d-th realization of the fit.

- After fitting all the on-axis points, we will start to fit all the off-axis points.

$$R_{f_i, f_d}(\hat{u}, \hat{v}) \Rightarrow W_{klm}, \Delta\hat{u}, \Delta\hat{v}. \tag{4.14}$$

- After fitting all the points, we need to evaluate the output W_{klm} coefficients which can describe the field dependency of our model.

- It was verified experimentally that the median applied to the set of estimated W_{klm} coefficients provides better results of the output model than other statistical methods. Thus, we need to find the median of every W_{klm} coefficient over all fit realizations (the number of realizations is L) of the used points. This step will eliminate extreme values of W_{klm} coefficients which can occur at some positions of the PSF due to convergence issues caused by sampling of the image or overfitting effects caused by high orders polynomials. Extreme values indicate that the algorithm found some local minimum of the cost function and not the global minimum. The values of the W_{klm} coefficients are then significantly different from the coefficients obtained in the previous position. These variations are given by the goodness of fit.

- The output set of W_{klm} coefficients then consists of values verified over the field.

As is illustrated in Figure 4.1, the described procedure repeats in every order (as defined in Equation (4.3)) of W_{klm} coefficients. The estimates of higher order coefficients (6th and 8th) come from lower order coefficients that have already been estimated from lower orders. If we want to describe our optical system with coefficients up to the 8th order, we will first need to obtain coefficients of the 4th order. Then, it is necessary to repeat the procedure from Equation (4.11) to Equation

(4.14) of the previously described procedure assuming 4th order W_{klm} coefficients as a starting condition. Following the whole procedure, we will estimate the 6th order coefficients. Then, repeating the procedure again with 6th order coefficients as a starting condition, we can finally calculate 35 coefficients of the 8th order. The result is a set of coefficients (the number of coefficients depends on the order that is used) related to the optical system with the field dependency described in Section 4.1.
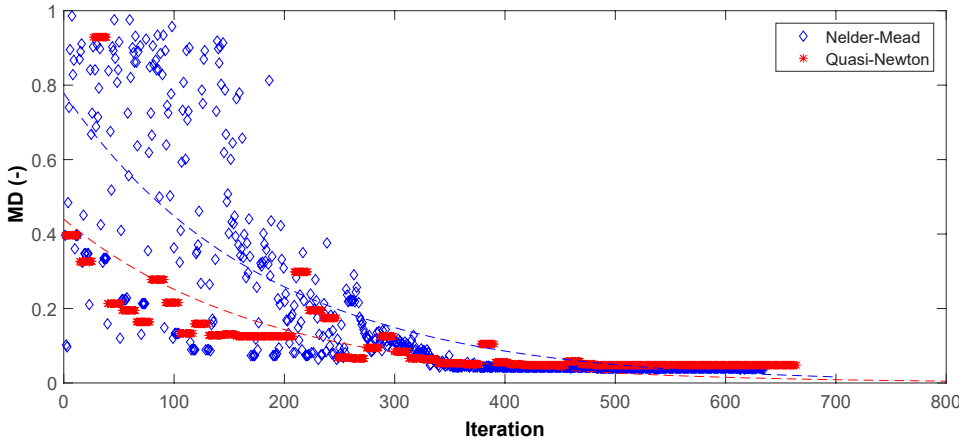
Figure 4.2: A graph comparing the performance of Nelder-Mead and Quasi-Newton optimization methods.

4.2.1 Optimization

As mentioned, the model uses the Nelder-Mead [88,89] optimization. However, the algorithm can find many local minimums during the optimization. The existence of many local minimums is a common issue of optimization. According to this obvious issue, it was defined as the calibration algorithm, described in the previous section. Following the prescribed steps leads to a successful finding of W_{klm} coefficients. However, the Nelder-Nead optimizing method can be time-consuming and leads to a high number of iterations. The Quasi-Newton optimization method, described by Bonnas [90], Press [91] and others, shows to be the promising alternative. Figure 4.2 shows comparison of Nelder-Mead (blue) and Quasi-Newton (red) optimization of MD parameter. As can be seen, the Quasi-Newton method provides straightforward optimization, when finding minimum of MD parameter. On the other side, the Nelder-Mead obviously tests many combinations (left part of the graph, blue markers) providing initially inappropriate results. However, after several iterations, a suitable optimization is found, and as can be seen, the model providing the $MD = 7\%$, as for the Quasi-Newton optimization. From this perspective, the Quasi-Newton optimization method indicates to be better tool. However, the Nelder-Mead method proved to be more robust method on large number of tests. It can be concluded, that Quasi-Newton method can be used for initial estimation of parameters, but for searching for a complicated model, the Nelder-Mead method proved to be the suitable method.

4.3 Sampling

An important part of the SVPSF model that has to be considered is the sampling of the exit pupil (in order to the wavefront sampling) and the image plane sampling. The Fourier transform (FT) is involved in calculations of the pupil function and corresponding transfer function, as illustrates Figure 4.3. In practical calculations the FFT is used. However, we have to fulfill the Nyquist-Shannon theorem where the sampling frequency $f_s = 1/\Delta x = 1/\Delta y$ must be more than two times higher than the cutoff frequency

$$\Delta x = \Delta y \leq \frac{1}{2 f_{cutoff}}.$$ (4.15)

The cutoff frequency can be expressed as

$$f_{cutoff} = \frac{D}{\lambda f},$$ (4.16)

where D is the diameter of the exit pupil, λ is the wavelength and f is the focal length. Then we can express the sampling distances as

$$\Delta x = \Delta y = \frac{\lambda f m}{D},$$ (4.17)

where is used the scaling factor m, that can affect the size of PSF in the image plane. As can be seen from Figure 4.3, the spatial frequency coordinates of image plane are expressed as $\Delta u = \Delta v = \frac{x}{\lambda f} = \frac{y}{\lambda f}$.
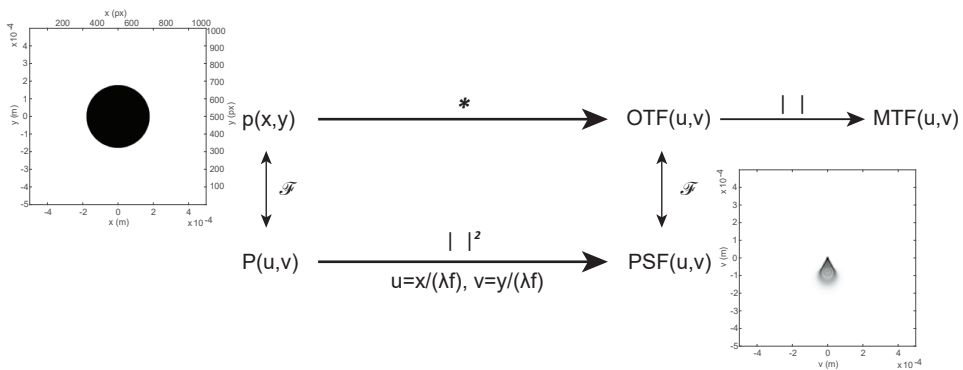
Figure 4.3: Illustration of the aperture function, PSF, MTF and OTF functions relations. Illustrated PSF of the 10λ Coma aberration shows the size of the PSF according to the aperture size (black circle).

4.4 Quality of the model

This section aims to verify the method for estimating the W_{klm} coefficients. We, therefore, simulated an artificial imaging system and tested the convergence of the introduced algorithm to find proper W_{klm} parameters. The second subsection of results involves modeling real imaging systems with the results of different orders of the Zernike polynomials. The input conditions, such as SNR > 20 dB (peak to noise) of all considered PSFs, the number of calibration images and FWHM, mentioned in Section 4.2 have to be taken into account before acquiring the calibration images and applying the algorithm of the PSF estimate.

4.4.1 Numerical Stability Verification

This section deals with verifying the stability of the optimization convergence. The test pattern, used for verifying the functionality of the algorithm was an image obtained by generating random W_{klm} coefficients (i.e., random power of optical aberrations) and placing PSFs in locations covering the entire field of view (see Figure 4.4), assuming a rotational symmetric imaging system. To verify the algorithm, we test PSFs in the locations marked with red circles.

Table 4.3: The sensor size, the resolution and the optical parameters of the simulated artificial imaging system.

Resolution	3358×2536 px
Sensor size	$18.1 \times 13.7\ mm$
Pixel size	$5.39\ \mu m$
Lens focus distance	$10\ mm$
FOV	$110°$

Table 4.3 summarizes the parameters of the simulated system. Table 4.4, Figures 4.5 and 4.6 show successive verification of the proposed algorithm by values of MD and the RMSE operator, a fitted curve illustrating the trend of the results, and standard deviation error bars. We can see that the difference between the original and the model is within the order of thousandths. The difference is given only by quantization noise and the sampling of the test pattern. The sampling of the original PSF appears as a serious issue, and low resolution causes problems within the convergence in the optimization of the W_{klm} parameters. The resolution of the image may affect the accurate positioning of the PSF. For an explanation, we can find the maximum of the PSF by calculating the center of the mass precisely, if the sampling of the pattern is finer. Therefore, if we can find the maximum precisely, we can use precise positioning $\hat{u}, \hat{v}$ for calculating the PSF of the system.

The graphs mentioned above provide information about the accuracy of the model against the positioning of the PSF in the image. However, it can also be useful to mention the accuracy of the model when the original image includes noise. For this reason, we performed a test where one PSF, in the center of the image,
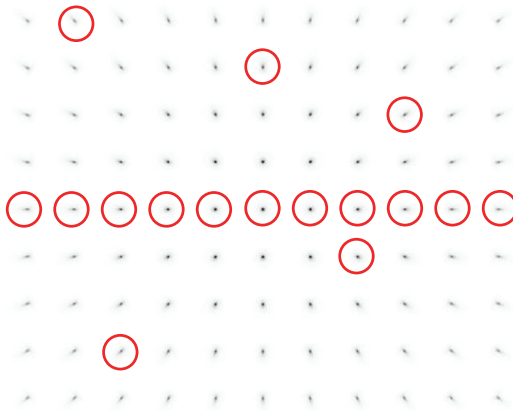
Figure 4.4: Field of simulated PSFs with randomly generated W_{klm} coefficients. We consider the simulated imaging system as rotationally symmetric. The points in the red circle were used for verifying the algorithm.

Table 4.4: Selected on-axis points results of verification of the algorithm, where normalized distance H is from 0 to 0.83 and ϕ is equal to zero. Image distance H is normalized according to the sensor, and it is related to a FOV of 110°; all optical parameters are summarized in Table 4.3. Differences between the original PSF and the model are within the order of thousandths. Thus, the proposed algorithm can find the exact W_{klm} coefficients used for generating the test pattern illustrated in Figure 4.4.

Metrics	Normalized Image Distance H (-)					
	0	0.17	0.33	0.50	0.67	0.83
RMSE (10^{-5})	8.2	7.3	8.8	16	57	270
MD (‰)	0.14	0.13	0.16	0.36	2.1	6.4

was affected by additional Gaussian noise. A test was performed in which the SNR in the image under test was from 28 dB to 9 dB (see Figure 4.7). We can see that the algorithm works quite well from 28 dB to 20 dB, and MD is less than 3%. However, when SNR is below 20 dB, the error decreases rapidly. This is due to the fact that our model focuses on optical aberrations, not on modeling the noise.

Figure 4.8 illustrates a direct comparison between the original PSF, the obtained model and the difference between them in relation to RMSE and the MD operator. This verification process was performed to verify whether the algorithm can find the model W_{klm} parameters that are closest to the W_{klm} coefficients used in generating the pattern illustrated in Figure 4.4.
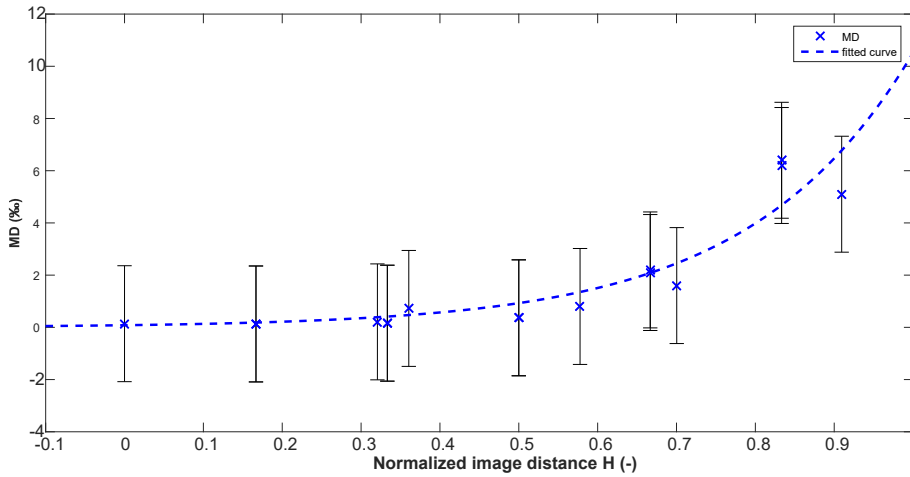
Figure 4.5: The verification results contain all points used in the verification. The positions of all points are illustrated in Figure 4.4. MD according to the normalized image distance.
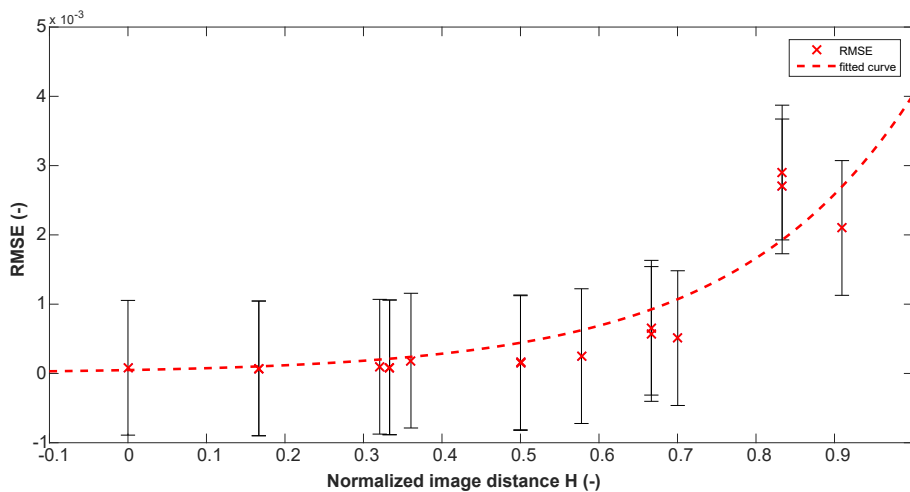
Figure 4.6: The verification results contain all points used in the verification. The positions of all points are illustrated in Figure 4.4. RMSE according to the normalized image distance.
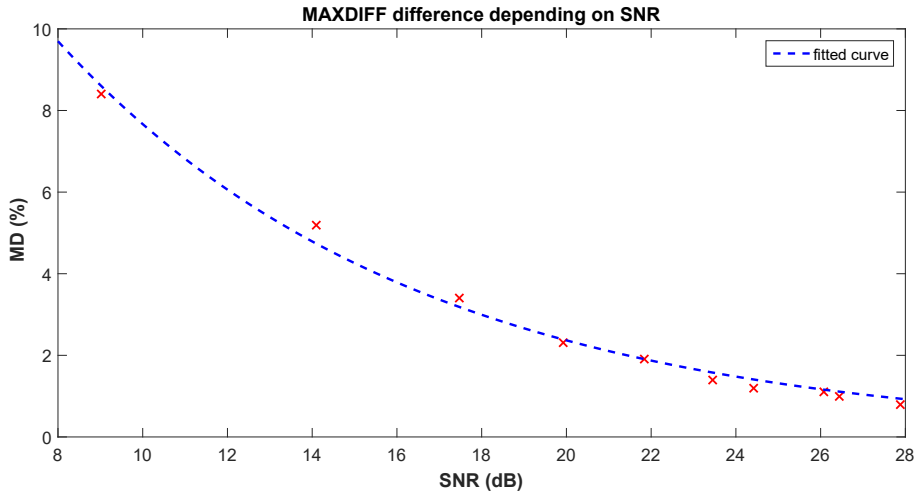
Figure 4.7: The dependence of SNR on MD. When SNR is lower than 20 dB, the error of the model increases rapidly.
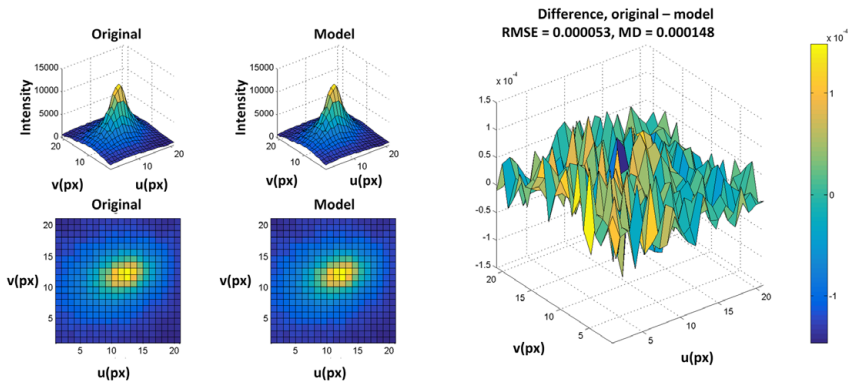
Figure 4.8: The result of fitting. A comparison between the original PSF and the PSF model of the system. The graph on the right shows the intensity of the difference between the original PSF and the model; it indicates a very good result for the goodness of fit.

Verification of the SVPSF model

This chapter is structured to the sections covering an application of the introduced SVPSF model on simulated data; experimental laboratory-acquired data and real all-sky image data acquired by the WILLIAM imaging system. Within all results, the specifics of the concrete imaging system are mentioned. The polynomial model was applied and successfully verified on image datasets acquired by G2-8300[1], ASI 1600MM-Cool, and Nikon D5100 cameras. The last image dataset was simulated in Zemax OpticStudio. This diversity of used imaging systems proves the versatility of the model according to different types of sensors (CCD vs. CMOS) cooled/uncooled systems and presence of the filtering mask (Bayer RGB mask).

5.1 Laboratory experiments

The first section describes the performance of the proposed model when dealing with real data acquired in the laboratory. The experimental images were obtained with the setup illustrated in Figure 5.1. A small white LED diode was used as a light source, together with a pinhole 200 μm in diameter. The first image dataset was acquired with a G2-8300 astronomical camera, providing a 3358×2536 pixel CCD sensor, corresponding to a size of $18.1 \times 13.7\ mm$, which gives a pixel size of 5.39 μm. The camera was equipped with a Sigma 10 mm EX DC HSM fisheye lens [2], which is the diagonal type of fisheye lens. A camera was mounted on a 2D rotational stage. This configuration, together with an observation distance of 5 m, gives the FWHM size of a PSF of around 6 pixels. Different positions of the light source, to cover the entire FOV, were achieved by rotating the camera in both, x and y axes. The advantage of this approach is that the same distance is kept between the light source and the camera, assuming that nodal mounting[3] has been used.

---

[1]http://www.gxccd.com/art?id=374& lang=405
[2]http://www.sigmaphoto.com/10mm-f2-8-ex-dc-hsm-fisheye
[3]http://nodalninja.com
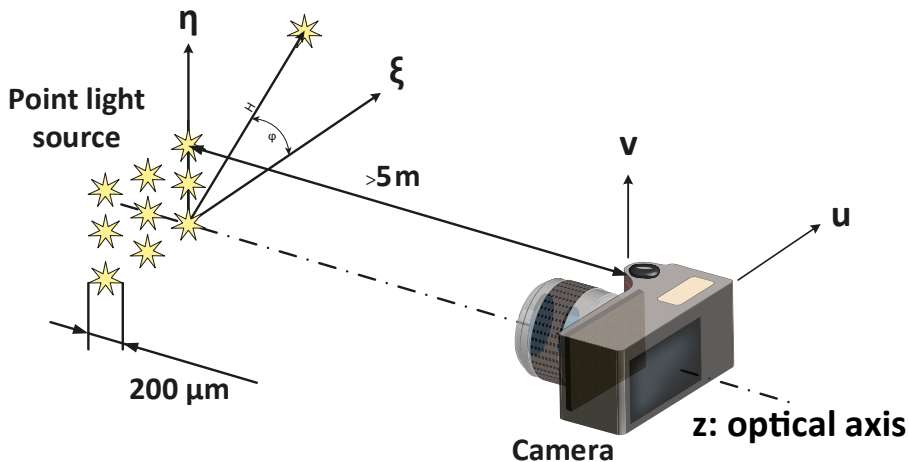
Figure 5.1: The experimental setup, consisting of a camera stage and a light source with a small aperture.

5.1.1 G2-8300 camera

The parameters of the imaging system based on G2-8300 camera are summarized in Table 5.1 and they are the same as for the simulated system in the previous chapter. However, it is necessary to take into account that the optical aberrations are different, according to the real imaging system using the G2-8300 astronomical cooled camera. The G2-8300 camera includes cooling that has been set down to $-15°C$ during acquiring of the image dataset. A corresponding MTF function is illustrated in Figure 5.2.

Table 5.1: The sensor size, the resolution and the optical parameters of the experimental imaging system used for acquiring the image dataset.

Resolution	3358×2536 px
Sensor size	$18.1 \times 13.7\ mm$
Pixel size	$5.39\ \mu m$
Lens focus distance	$10\ mm$
FOV	$110°$

Figure 5.3 provides the illustration of the estimated W_{klm} coefficients. The graphs in Figures 5.4 - 5.6 and Table 5.2 show the results of the fit with a different order of W_{klm} coefficients, a fitted curve illustrating the trend of the results, and standard deviation error bars. Figure 5.7 shows a comparison of the results with other PSF modeling methods. It can be seen, that the best result is obtained with coefficients up to the 4th order. Then, with a higher order of the coefficients, we obtain slightly worse results, even for the PSFs placed on the optical axis. With

increasing image distance, the situation seems to deteriorate, and the difference increases. One reason for this is the optimization convergence, which is worse for the more involved W_{klm} coefficients in 6th and 8th orders. Another explanation is provided by Figure 5.8 and Table 5.3. It can be seen that the absolute difference is slightly worse for higher orders of W_{klm} coefficients, but that the shape of the model or the precision of the obtained shape of the PSF is better. The image of the differences in Figure 5.8 provides information proving that the maximum of the difference is located in a smaller number of pixels in the central part of the PSF. Thus the model seems to be well described in terms of the shape description. It can be concluded that the higher order (6th and 8th) W_{klm} coefficients provide better parameters of the model in terms of the shape description and better localization of aberrations, but sometimes at the cost of a slightly worse absolute difference. Table 5.2 shows another interesting phenomenon. The results obtained by 8th order fitting are slightly better than the results obtained by 6th order fitting. It was observed that the 6th order model aberrations are overfitted; the model adds aberrations which are actually not present. However, use of the 8th order model compensates these overfitting effects. Finally, it has to be admitted that it is not always necessary to use high order Zernike polynomials, and our results illustrate that a simple solution including only basic aberrations (up to the 4th order) provides results of several percents.
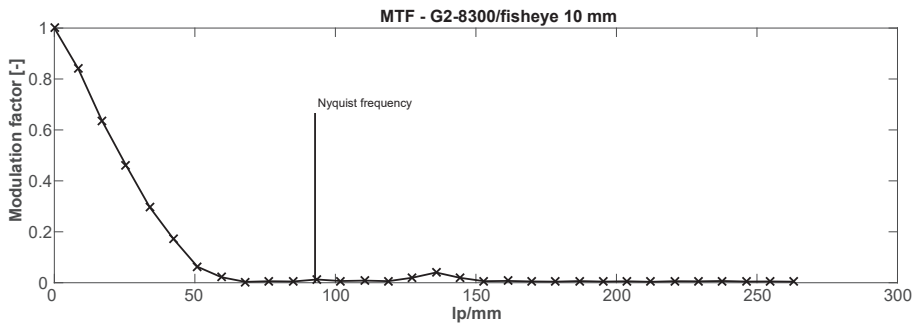
Figure 5.2: Graph of the MTF function of the G2-8300 camera.

Table 5.2: Selected on-axis point results for the MD difference between the original and the estimated model, where H is from 0 to 0.83 and ϕ is equal to zero. The MD differences of the polynomial orders are given as a percentage. Highlighted columns contain results used later in the comparison.

Metrics	Normalized Image Distance H (-)					
	0	0.17	0.33	0.50	0.67	0.83
4th order	4.6	5.1	5.3	7.8	7.5	9.4
6th order	5.4	7.7	6.5	9.4	7.7	12.5
8th order	5	6.4	6.1	7.7	7.6	10
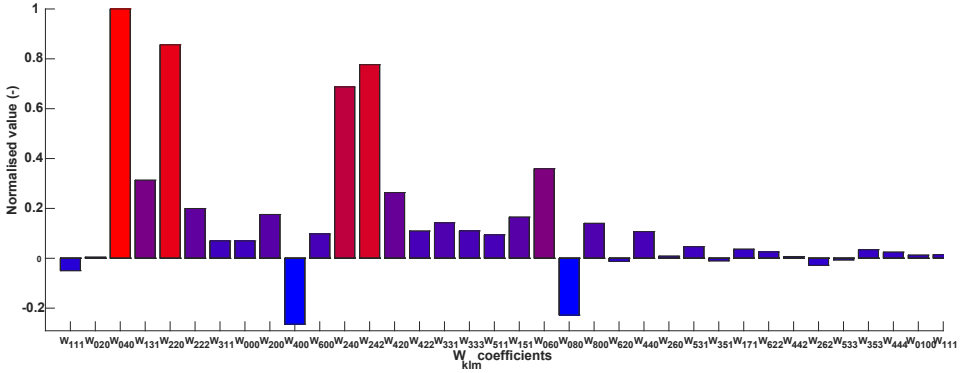
Figure 5.3: Illustration of the all W_{klm} coefficients up to 8th order of the G2-8300 cooled CCD camera. W_{040} coefficient is contained in the piston and the defocus Zernike polynomials. W_{220}, W_{240}, W_{242} relates to the Astigmatism and Oblique Spherical. W_{klm} coefficients are normalized for the purpose of the illustration.
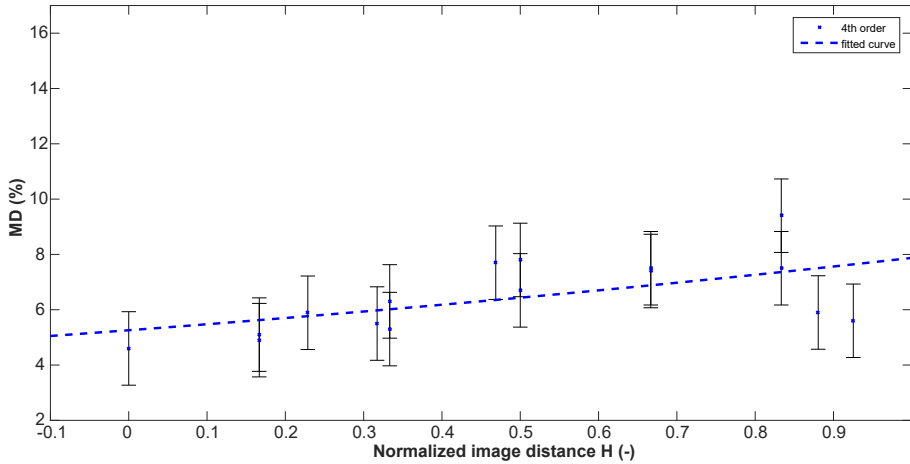
Figure 5.4: Experimental results for the MD difference up to the 4th order. The graph contains results from Table 5.2 and ten other points according to the normalized image distance *H*. The points which are not mentioned in Table 5.2 are selected similarly as illustrated in Figure 4.4. The angle ϕ of these points differs from zero. These points are placed at positions covering the entire FOV.

When we compare the method for estimating field-dependent PSF with other approaches mentioned in the introduction, we obtain similar results. Results from all implemented approaches are illustrated in Figure 5.7. An approach based on work by Piotrowski [1], labeled as the Interpolated model, provide results of the MD operator from 7.8% to 9.9% over the FOV. Another approach based on Weddell's method [23], labeled as the Sectorized model, which divides the image into smaller
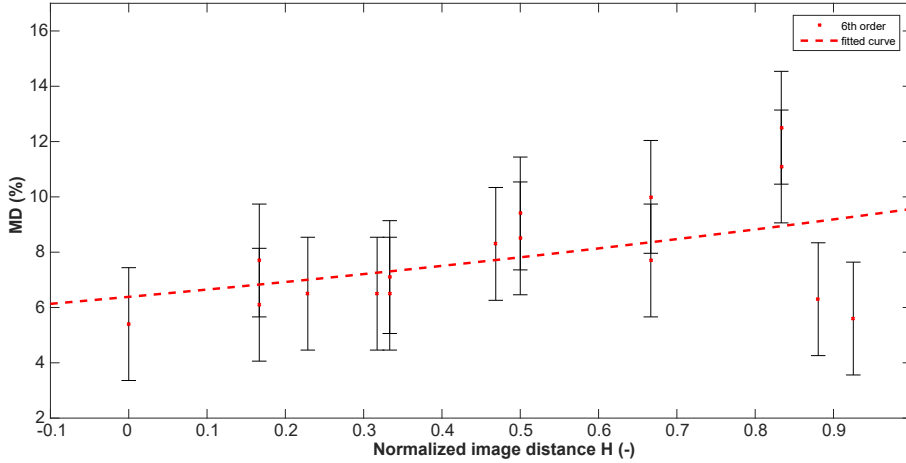
Figure 5.5: Experimental results for the MD difference up to the 6th order.

invariant parts, provides similar results to the Interpolated model. However, it can be seen that the Sectorized model may fail when the PSF model in one sector does not precisely fit to all PSFs inside the sector. This can be seen in Figure 5.7, where the results for the Sectorized model (marked with a black+) at $H = 0.83$, 0.88, and 0.92 vary from 8% to 17%. The last method included here is fitting the PSFs with a Gaussian function [92] which was chosen because it can be used as a model of the diffraction limited optical system. This approach provides results from 14% to 22%; however, we had not expected very good results from this method. The Gaussian model was used as a complement to the space-variant methods. We also implemented an approach that uses the Moffat function [92]. However, the results provided by fitting the Moffat function start from 20% and go up to 40%. We therefore concluded that the Moffat model is inappropriate, and we did not include these results in Figure 5.7.

Table 5.3: A direct comparison of results estimated by 4th, 6th and 8th order polynomials. This table is related to Figure 5.8. The results are calculated for one position of the light source at $H = 0.33$. The total flux difference was calculated for enumerating the overall intensity difference between the original PSF and the model.

Metrics	4th Order	6th Order	8th Order
RMSE (-)	0.032	0.039	0.036
MD (%)	5.3	6.5	6.1
Total flux difference (‰)	0.31	0.35	0.37
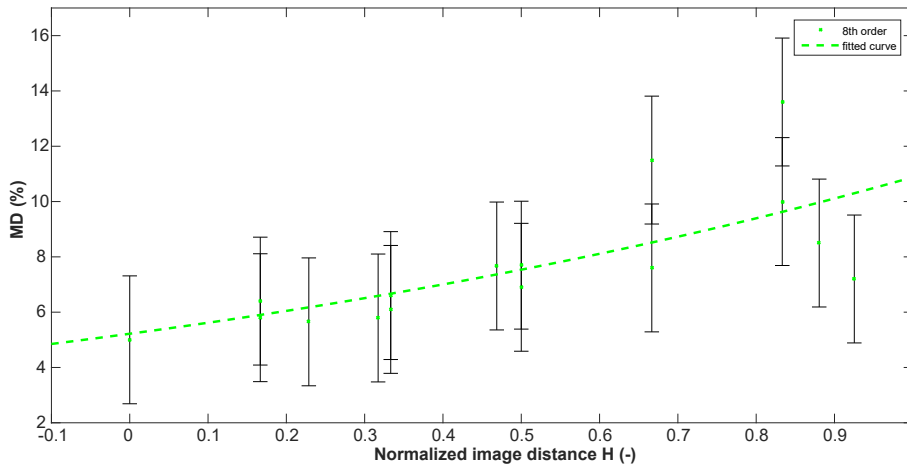
Figure 5.6: Experimental results for the MD difference up to the 8th order. The graph contains results from Table 5.2 and ten other points according to the normalized image distance *H*. The points which are not mentioned in Table 5.2 are selected similarly as illustrated in Figure 4.4. The angle ϕ of these points differs from zero. These points are placed at positions covering the entire FOV.
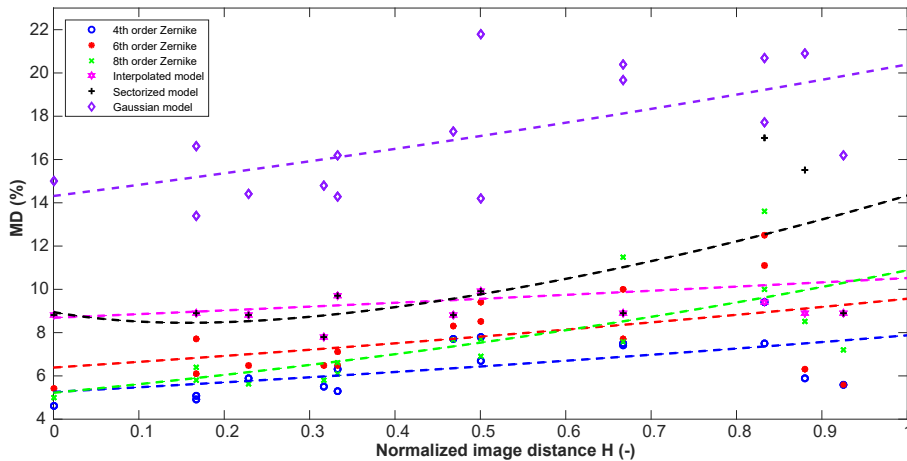
Figure 5.7: A comparison of different modeling of a single optical system. All models were fitted with the same set of PSFs.
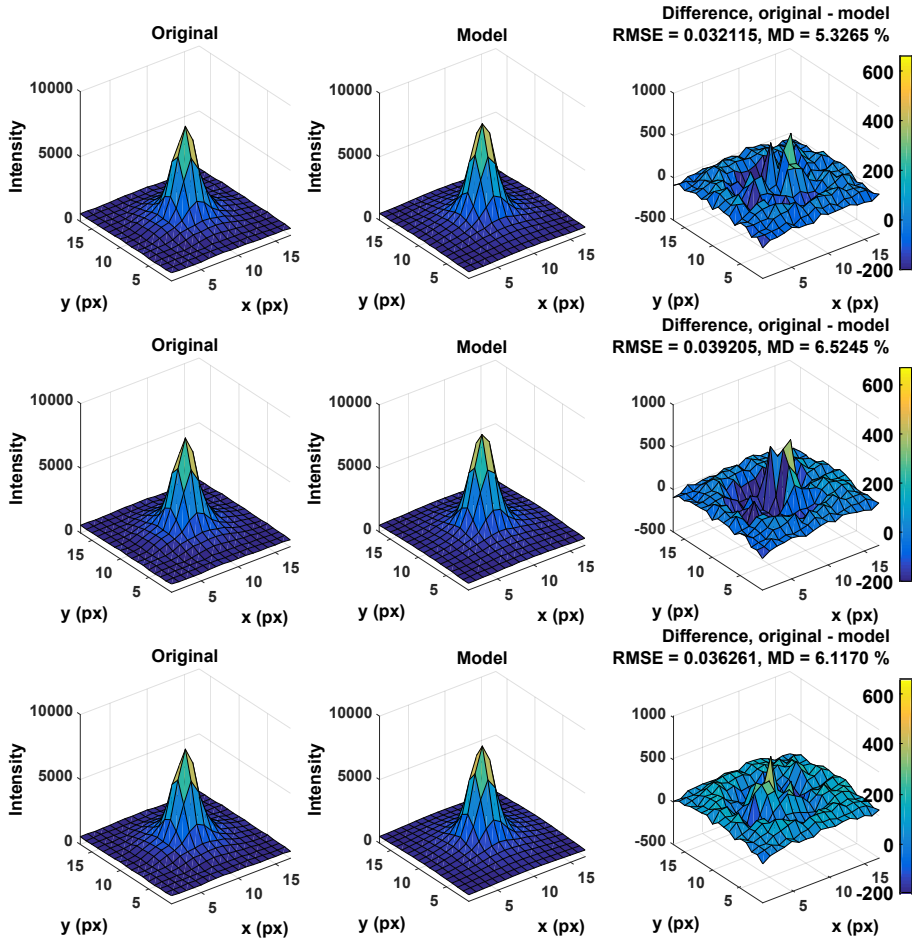
Figure 5.8: Results of the fitting. The PSF model is shown with different orders of polynomials. The object was placed at 20° with respect to the optical axis (H = 0.33). In Table 5.2 this PSF is marked with the blue column. The first row relates to the 4th order results, the second row relates to the 6th order results and the third row relates to the 8th order results.

5.1.2 ASI1600MM-Cool camera

The second laboratory image dataset was acquired by ZWO ASI1600MM-Cool CMOS camera using the same model of the fisheye lens - Sigma 10 mm EX DC HSM. All details of this camera setup are summarized in Table 5.4. As can be seen, the ASI1600MM-Cool camera provides higher resolution then G2-8300 camera, and due to the larger sensor, the ASI1600MM-Cool provides larger FOV. Both mentioned cameras include cooling and for the purpose of the experiment were both cooled down to $-15°C$. A comparison of Figure 5.9 and Figure 5.2 indicates the similarity of spatial resolution of both cameras.

Table 5.4: The sensor size, the resolution and the optical parameters of the experimental imaging system used for acquiring the image dataset.

Resolution	4656×3520 px
Sensor size	17.6×13.3 mm
Pixel size	3.8 μm
Lens focus distance	10 mm
FOV	$160°$

As can be seen from Figure 5.10, dominant coefficients such as W_{040}, W_{400}, W_{600}, W_{060} indicate a strong influence of defocus, spherical and piston aberration. Another strong coefficients such as W_{020}, W_{200}, W_{151}, W_{533} indicate influence of the piston, the coma and the elliptical coma. Corresponding coefficients of Zernike polynomials can be found in Table 4.1.
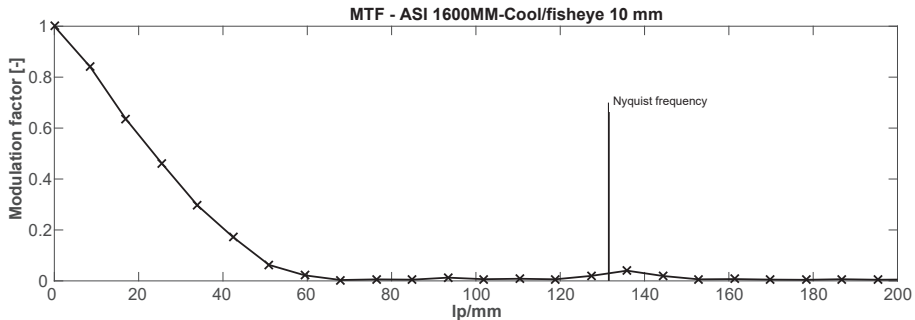
Figure 5.9: Graph of the MTF function of the ASI 1600MM-Cool camera.

The laboratory image dataset was acquired using the same scenario, i.e., we have obtained a series of a laboratory image data of a white point light source that was placed behind pinhole with 200 μm diameter. The ASI1600MM-Cool was mounted on the nodal stage that guarantees to keep a focused distance from the object to camera sensor. The acquired image data were then used for evaluation of the UWFOV model of the imaging system. The image data contains point

light source at different distances from the Optical axis (OA) assuming rotational symmetric optical system, as illustrates Figure 5.1.
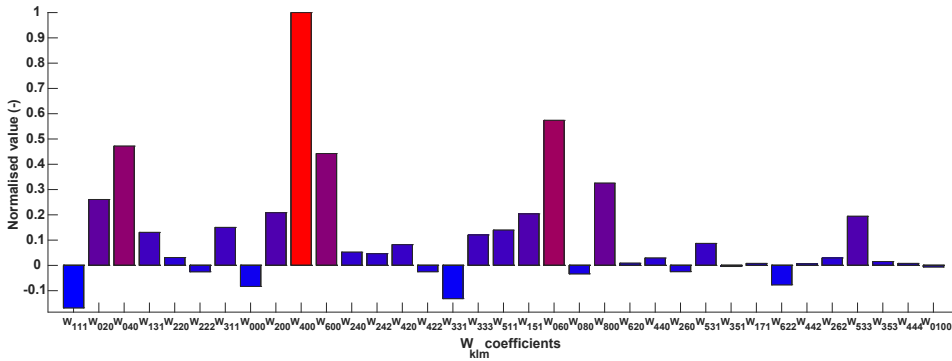
Figure 5.10: Illustration of the W_{klm} coefficients of the WILLIAM imaging system with ASI 1600MM-Cool camera. The W_{400} coefficient, as the dominant coefficient, is contained in piston, spherical aberration and defocus Zernike polynomials.
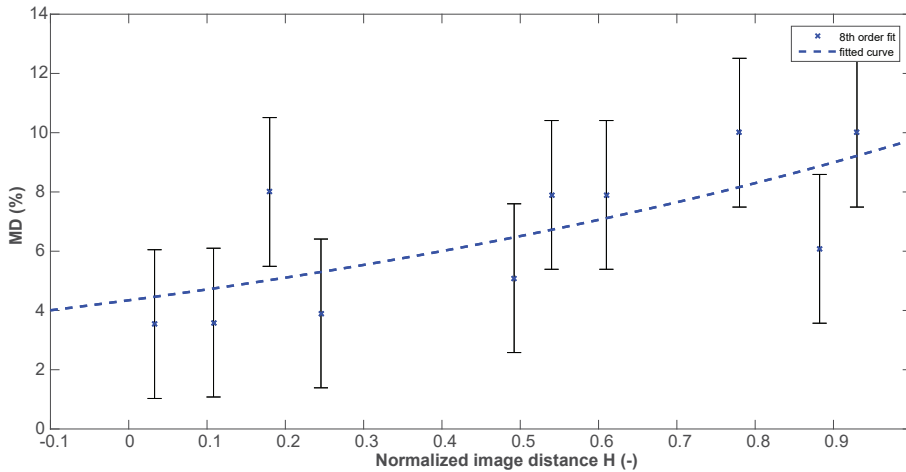
Figure 5.11: Results for the MD difference of the ASI1600MM-Cool camera.

The graph in Figure 5.11 provides results of the ASI1600MM-Cool image data fitting by SVPSF model. As can be seen, obtained W_{klm} coefficients and therefore the model provides the precision of 3.5% in the central part. Moving away from the optical axis, the precision of the model slightly decries to 6.5%. However, overall the model of the ASI1600MM-Cool camera provides very good results, partially thanks to the size of the PSF that achieves 15 px in diameter. This size reduces the issue with sampling and possible interference with sensor's pixel grid. As can be seen from Figure 5.12 the model indicate good agreement with the originally acquired PSF.
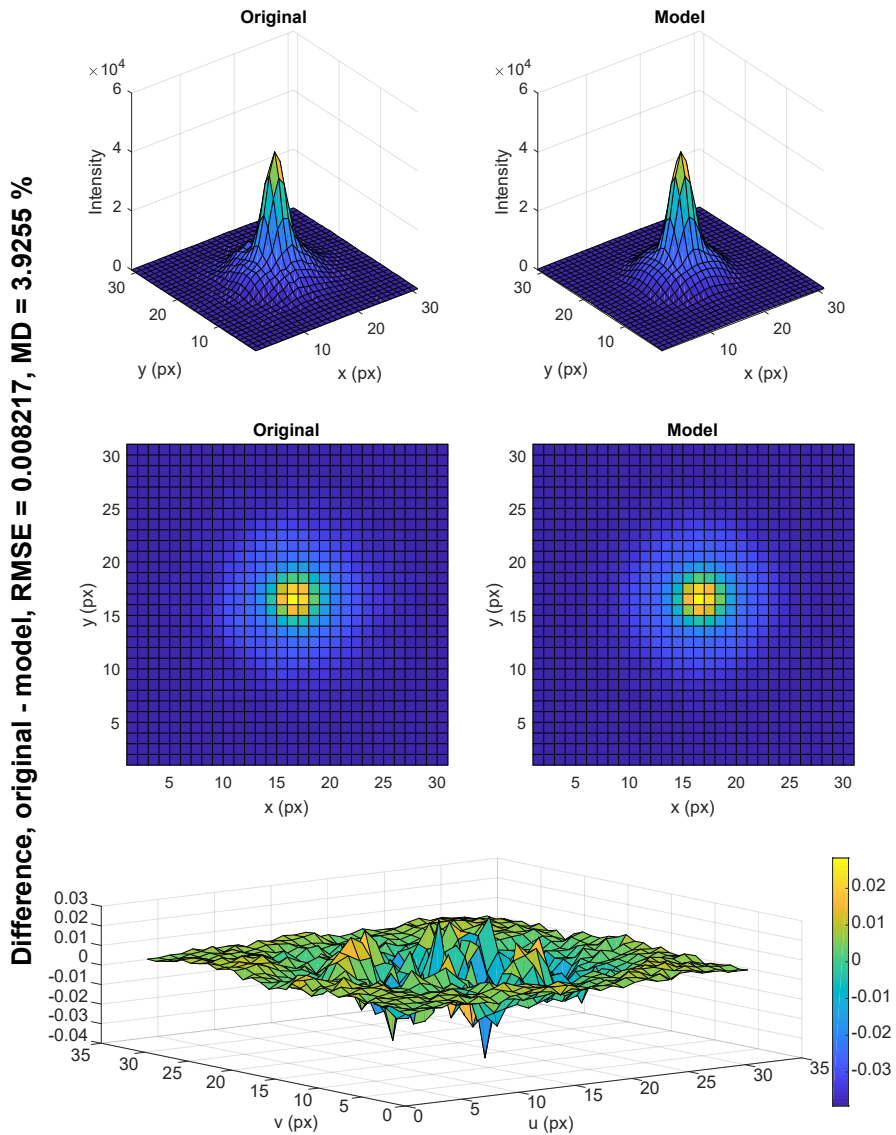
Figure 5.12: An example of the original and estimated PSFs related to the image dataset acquired by ASI1600MM-Cool. As can be seen, their difference reach 3.9%, and these PSFs are almost identical.

5.2 Real sky image data fitting

5.2.1 Camera Nikon D5100

The third dataset represents the image data acquired by the first generation of the system WILLIAM equipped by the camera Nikon D5100. As has been mentioned, the WILLIAM system is an all-sky camera, and the acquired dataset contains night sky images with stellar objects. Since the projection of these objects has a size similar to the pixel size, we assume the stellar object as a point source of the light, that can be considered as system's PSF. Here mentioned results of fit are calculated using one stellar object at several images acquired during one night. Then the object covers almost the entire field of view as it is acquired at different positions during the night. Nevertheless, image data from WILLIAM system include various types of distortions. Except for optics aberrations, it is blurring caused by atmosphere turbulence. However, more complicated issue causes the interpolation of RGB channels from Bayer mask mentioned above. Even when we use the advanced method of interpolation (Laroche-Prescot), the PSF model of such a system cannot describe this type of distortion. As has been seen from Figure 2.2, using the Bayer mask in high precision scientific systems (according to precise photometry, for meteorology clouds clustering is using of the Bayer mask suitable) seems to be the risky and inappropriate solution. The object is sampled in different color channels, and output interpolation of channels misrepresents the object shape.

Table 5.5: The sensor size, the resolution and the optical parameters of the experimental imaging system used for acquiring the image dataset.

Resolution	4928×2448 px
Sensor size	23.6×15.7 mm
Pixel size	5.39 μm
Lens focus distance	10 mm
FOV	$170°$ (diagonally)

As for the previous cameras, the specifications of the Nikon D5100 are provided in Table 5.5, and measured MTF can be seen from Figure 5.13, including the modulation function for red, blue and green channel and the luminosity. As can be seen, the DSLR camera provides slightly higher resolution than the ASI1600MM-Cool camera. However, this small disadvantage is compensated by the high gain and the sensitivity of the astronomical camera sensor. Figure 5.14 illustrates estimated W_{klm} coefficients. The graph shows the strong influence of W_{220} that indicates the power of the piston and the defocus. However, other strong coefficients arose, such as W_{240}, W_{331}, W_{333}, W_{551} or W_{171}. These coefficients indicate the influence of the spherical, the tilt, the coma, and the 5$^{\text{th}}$ coma aberrations.

The estimation complexity can be seen in Figure 5.15, where are illustrations of different stellar object profiles at various positions in the FOV. We can see how
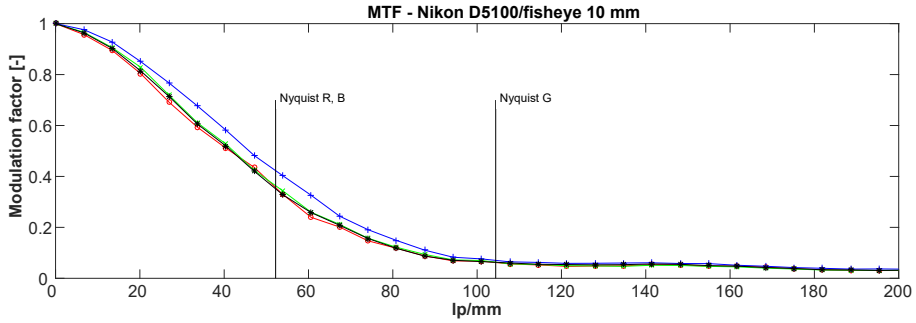
Figure 5.13: Graph of the MTF function. The upper graph shows Nikon D5100 camera (RGB channels and grayscale plots including the Nyquist frequency for R, B, and G channel), lower graph is the ASI 1600MM-Cool camera plot.

complicated these profiles can be and how important is to have a high-resolution sensor for acquiring night sky image data. Then we have to realize; these profiles are already interpolated data. That means, in fact, RGB channels are even more undersampled. This leads to a conclusion about the wise decision of choosing a sensor for scientific or other precise observation and measurement. As can be seen from our results, the monochromatic camera (in fact, we can use the color camera, but equipped with color wheel) provide better results, when we try to model such an imaging system.
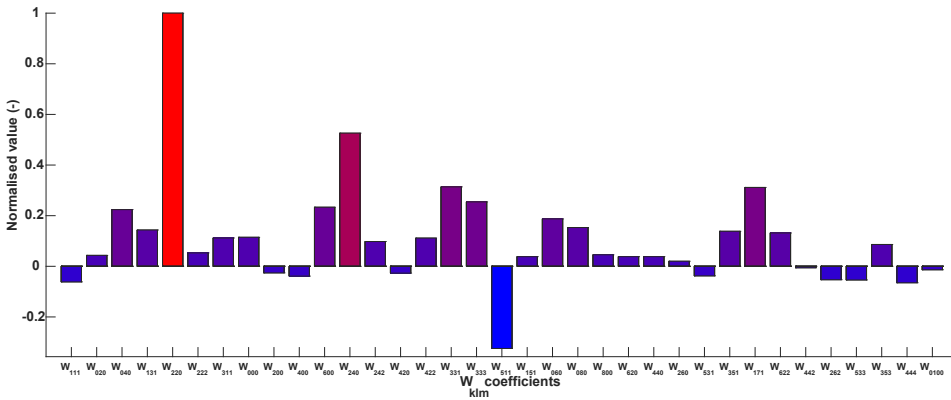
Figure 5.14: Illustration of the W_{klm} coefficients of the WILLIAM imaging system with Nikon D5100 camera. W_{220} indicates the power of the Piston and the Defocus. However, other strong coefficients arose, such as W_{240}, W_{331}, W_{333}, W_{551} or W_{171}. These coefficients indicate the influence of the Spherical, the Tilt, the Coma, and the 5$^{\text{th}}$ Coma aberrations.

Resulting precision of the estimated PSF model can be seen from Figure 5.16. At a glance can be seen that resulting precision is worse than for previous datasets. Namely 10% at the OA up to 20% at the edge of the FOV. One of the explanation
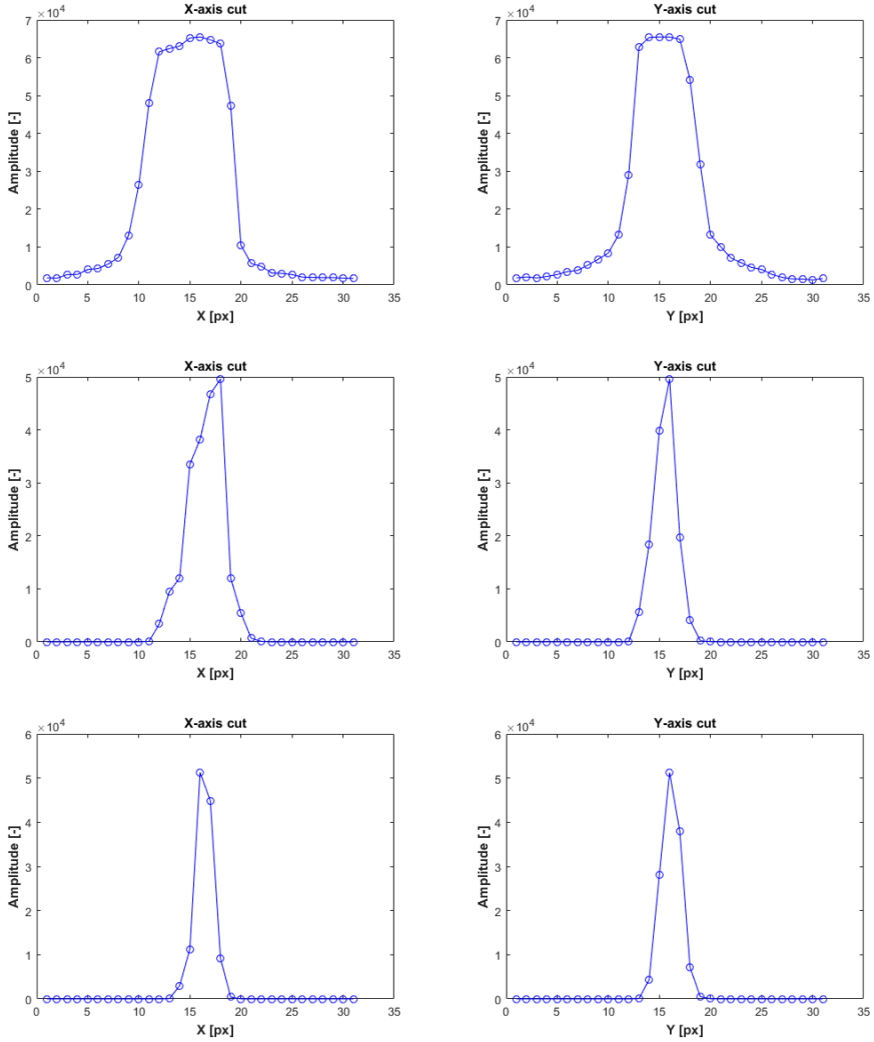
Figure 5.15: Three stellar objects profiles. Cuts in x and y-axis show complicated profiles of the PSFs acquired by the WILLIAM imaging system.
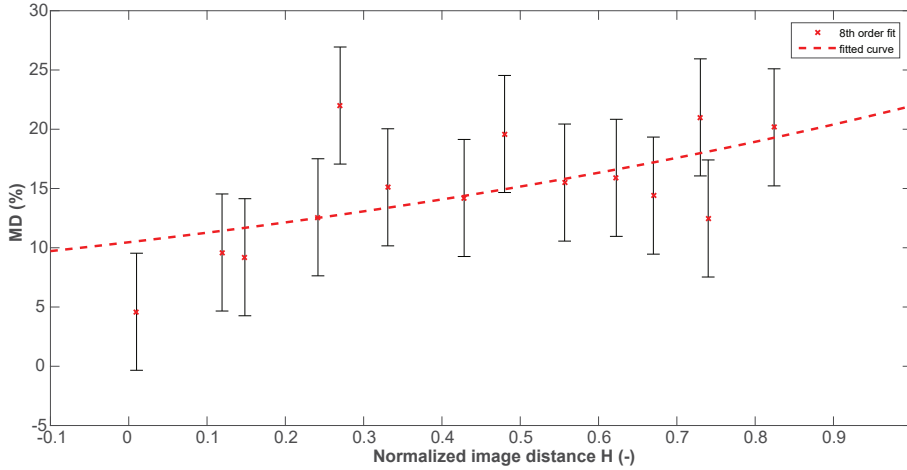
Figure 5.16: Results for the MD difference of the Nikon D5100 camera.
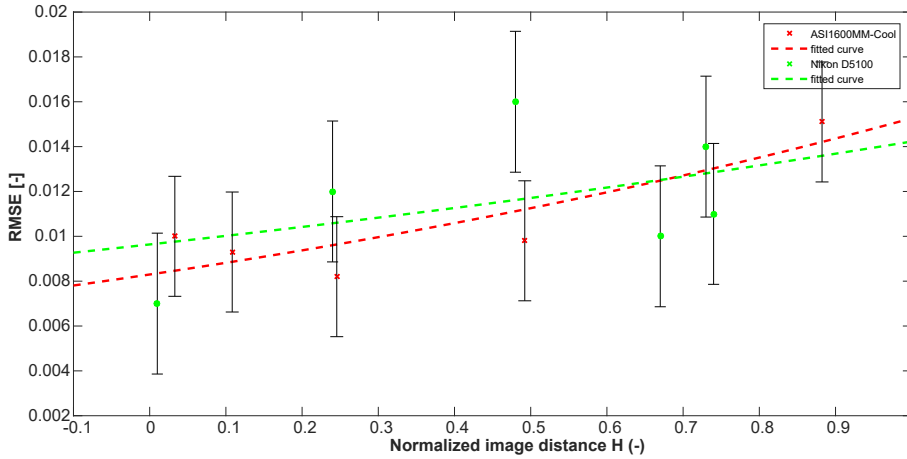
Figure 5.17: A comparison of the RMSE difference of the ASI1600MM-Cool and Nikon D5100 cameras.

is the noise, because the Nikon D5100 camera has no cooling, and processed image dataset was calibrated by not the up-to-date dark frame. However, as has been mentioned in Section 5, the noise tolerance should be sufficient. The explanation has to take into consideration the acquiring conditions that the stellar object was not perfectly focused. Whether by the influence of the atmospheric turbulence or by overexposing. These facts, which can be simply eliminated in laboratory acquirement, can cause the issues during the PSF estimation and the resulting model of PSF cannot precisely describe. However, when the MD metrics exhibits single (one pixel) errors that cause large percentage differences, we can use the second metrics, RMSE, that is not sensitive to extremal singular errors. By the

RMSE metrics, the model can be compared with the original PSF in the meaning of the overall intensity error.

Figure 5.17 show the comparison of the RMSE values of the Nikon D5100 and the ASI1600MM-Cool cameras PSF fitting. As can be seen, the calculated RMSE results of differences are similar to each other. It should be noted that the size of the PSF of both cameras is approximately the same. It can be concluded, that modeling of the real-sky images complicates the modeling task by another phenomenon such as the atmosphere turbulence or time-shift, but it can be modeled with desired precision. However the much difficult issue is the mentioned influence of the Bayer mask, and further research should address this part of the model.

5.3 Image data simulated by Zemax

The previous sections described the performance of the model on the acquired image datasets. The last dataset was simulated in Zemax OpticStudio[4], that is broadly used for designing the optics. The optics used for the simulation was a simple doublet with aperture diameter 20 mm and focal length 100 mm, illustrated in Figure 5.18. As can be seen from Figure 5.19 and Figure 5.20, PSFs of the doublet optics are for image height 5 mm distorted by the sum of aberrations. However, uncompensated aberrations of the doublet example are suitable for the SVPSF model testing. The image data with an obvious SVPSF represents suitable input for the model verification. However, the change between the central PSF and the marginal PSF sets a high demand on the model estimation.
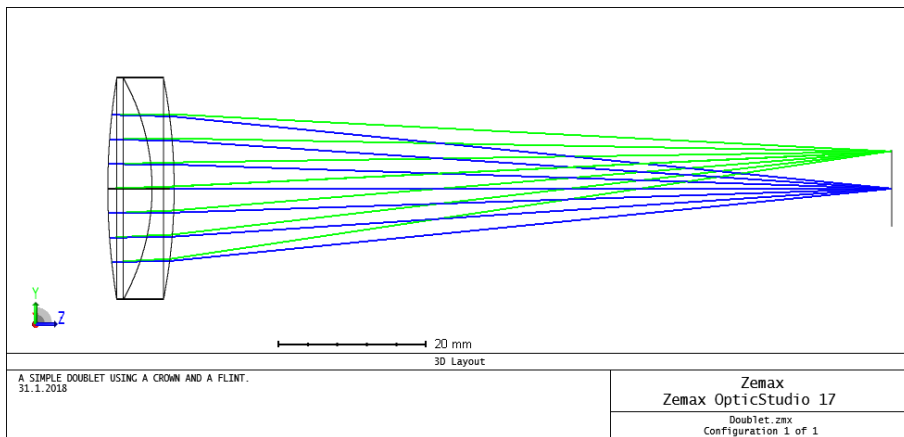
Figure 5.18: The layout of the simulated doublet. The aperture has 20 mm diameter, and the focal length is 100 mm.

Figure 5.19 illustrates the grid and also the size of the simulated PSFs. Three PSF are shown in detail. As can be seen, the violet square illustrates the central PSF of the size of only one pixel, which indicates perfect PSF. However, the yellow

---

[4]https://www.zemax.com/opticstudio

square and the red square show two marginal PSFs, that indicate strong aberrations. As can be seen, the size of PSF is only several pixels. This small size of the PSF can cause issues during the estimation of the W_{klm} coefficients as for the case of Nikon D5100 camera coefficients estimate. However, we have to realize, that the dataset simulated in the Zemax does not contain the noise and it is not time-shifted due to the overexposure. The set of estimated W_{klm} coefficients is illustrated in Figure 5.21, where can be seen the dominant W_{131} coefficient that relates to the coma aberration. The other strong coefficients W_{220}, W_{240}, W_{420}, W_{331} and W_{620} show the dependence on the piston, the defocus and the tilt aberrations.
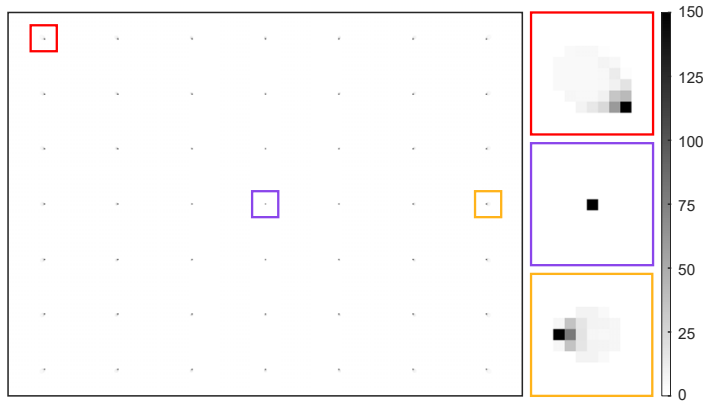
Figure 5.19: Illustration of the simulated grid of PSFs by Zemax. The details on the right side show the amount of aberrations.

Resulting SVPSF model provides precision of the MD metrics below 5% at the OA and up to 10% at the edge of the FOV. Taking into account the small size of the provided PSFs, the resulting model provides a fairly good estimation of the simulated system.

(a) PSF at optical axis.

(b) PSF at 5 mm image height.
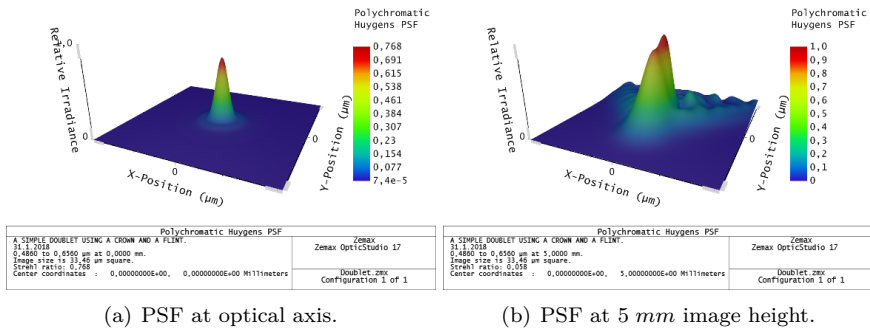
Figure 5.20: An example of a) on-axis PSF and b) off-axis PSF. As can be seen, the system produces heavily aberrated impulse response.
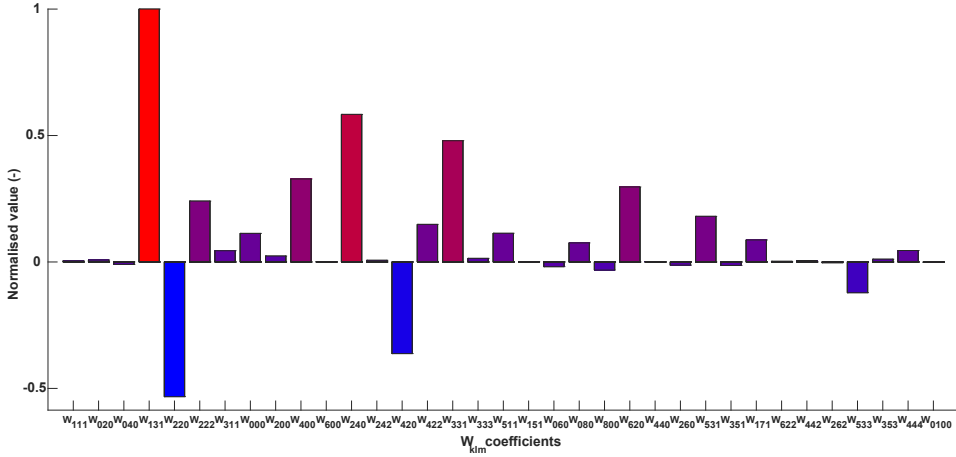
Figure 5.21: Illustration of the W_{klm} coefficients of the doublet simulated by Zemax. W_{131} coefficient that relates to the coma aberration. The other strong coefficients W_{220}, W_{240}, W_{420}, W_{331} and W_{620} show the dependence on the piston, the defocus and the tilt aberrations. W_{klm} coefficients are normalized for the purpose of the illustration.
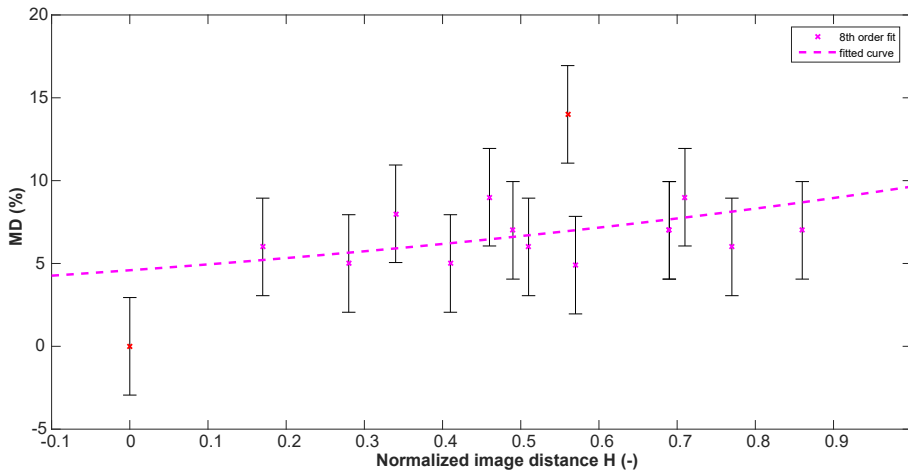
Figure 5.22: The precision of the PSF model for the doublet image data achieves 4% in the central part and 7% at the edge of the FOV.

5.3.1 Summary of results

The proposed method includes detailed information about the shape of the PSF of the imaging system. Information about the shape of the PSF can be important for PSF fitting photometry in astronomy [93], for deconvolution algorithms in microscopy [94] [95] and for other applications. The model of the UWFOV system was successfully used by Fliegel [56] for a comparison of the deconvolution methods.

In this context, a direct estimate of field-dependent Zernike polynomials brings a new approach to the description of space-variant imaging systems. The method was also used for modeling the WILLIAM all-sky camera [55], where the modeling method faced the issue of the presence of the Bayer mask in the system.

The proposed method for estimating PSF from an optical system is novel in a direct estimate of optical aberrations of the optical system. It is a difficult task to describe a system of this type, and UWFOV systems further greatly complicate this situation, since they are heavily aberrated. By this method, it is summarized a complex mathematical approach, and provides an algorithm for modeling the PSF of space-variant optical systems. The proposed algorithm has been verified with simulated data, and has been applied to real image data, showing the error of the model around 5%. A comparison of images with different SNR provide MD results around 3% for images with SNR greater than 20 dB. The algorithm has been compared with other space-variant modeling methods. It has been shown to be competitive since the results are better than or equal to the results provided by other modeling methods. Other space-variant models provide accuracy around 8.5%. The results demonstrate that the approach described here is also suitable for UWFOV systems. The results compare models of imaging systems of 4th, 6th, and 8th orders of Zernike polynomials and show some benefits of using different orders. The accuracy of the results of different cameras varies from 3% to 10% in the central part of FOV and from 8% to 20% at the margin. However, we have to distinguish between better results of fit for cameras without Bayer mask and slightly worse results for the Nikon camera with the Bayer mask. The average precision of the model is below 10% precision. The contribution to the description of aberration is via a method for obtaining aberration coefficients in an unknown optical system and for using them in the model of space-variant PSF. The algorithm was used to model the WILLIAM system [55], and the model provided by the approach described here was used in a comparison [56] of deconvolution methods.

Conclusions

Modeling of Space Variant Optical Systems focuses on methods for describing imaging systems. The model is based on the implementation of Zernike polynomials and their field-dependent a_n^m coefficients. The thesis presents the search for a model that can describe the UWFOV imaging system or generally a SVPSF system, for which the PSF has not been adequately described. Improperly modeled PSF limits further processing of the images, e.g., deconvolution, astrometry, and photometry.

6.1 Summary

The thesis is divided into six parts, covering the theoretical research necessary to address the aim, the adaptation of known modeling techniques (Zernike polynomials), and the proposal of a model.

Chapter 1 introduces known contributions to the design and the description of an optical system. Three major works, by Weddell, Piotrowski, and Zheng, were identified as convincing, and they provided the inspiration for the thesis. However, each of these works contains blind spots, which have been resolved in this thesis.

Chapter 2 introduces the SVPSF imaging systems that the author of this thesis has been involved in as a team member. In the case of the WILLIAM project, the author is the principal designer. In 2018, the THETIS project is in the phase of preparing a breadboard, and further work will address the performance of the Calomel crystal in acousto-optic tunable filters.

The theoretical background in Chapter 3 addresses the expressions leading to a description of the wavefront. An important part of this chapter is the adaptation of Zernike polynomials to a non-circular aperture. This step allows the model to be used in various kinds of specialized optical systems.

Chapter 4 starts on the main idea of the thesis, i.e., the field dependency of polynomials. A described set of field-dependent coefficients connects the polynomials and the position of the PSF in the FOV. However, a description of the field

dependency is useless without an algorithm for obtaining the coefficients. Chapter 4 presents the necessary steps in detail, and also the accuracy of the model.

Verification of the proposed model is presented in Chapter 5. The model is subjected to a quantitative analysis, which demonstrates the versatility of the approach. The coefficients of the model are estimated for CCD, for CMOS astronomical cooled cameras, for the DSLR camera and for the optical model simulated in Zemax OpticStudio. The results of the estimated model are successfully compared with the approaches introduced in Chapter 1.

6.2 Contributions of the Thesis

- The novel PSF model with space-variant coefficients of the Zernike polynomials describing the field dependency of PSF is described in Chapter 4.

- An algorithm for estimating the field-dependent coefficients is proposed, together with two evaluation methods.

- A novel set of N-gon polynomials is introduced in Chapter 3. This chapter includes an analytic description and a performance analysis of the proposed polynomials.

- The proposed model of the SVPSF is verified on a series of simulated laboratory acquired and real-sky image data. The results are faced with results obtained by other PSF estimation methods, and they demonstrate the suitability of the solution. Optimization of the coefficients is identified as a weak point of the model, due to difficulty with finding the global minimum of the function. An algorithm that helps to find a suitable set of coefficients is proposed.

6.3 Future Work

The thesis provides a workbench for modeling a complicated imaging system with SVPSF. Further work should address the influence of sensor grid sampling, and implementation of interpolation methods suitable for small objects. The model can be extended to different evaluation methods that meet specific requirements.

Furthermore, the PSF model can be extended in a part of noise modeling, e.q. [96] and [97]. Because in a present form, the model expects the robustness up to the noise level (see Chapter 4). Implementation of mentioned techniques can improve the model for real scenes including a significant level of noise.

The model introduced in the thesis can be operated for the opposite purpose, i.e., as a simulator. It can be used for simulating PSF fields, according to the work of Blažek [98]. A simulation of the PSF grid was used in the Chapter 4, where the simulated dataset was obtained by creating a PSF with random coefficients. Using the simulator and the principle introduced by Blažek [98], the field of space-variant objects can, therefore, be simulated (Figure 6.1).
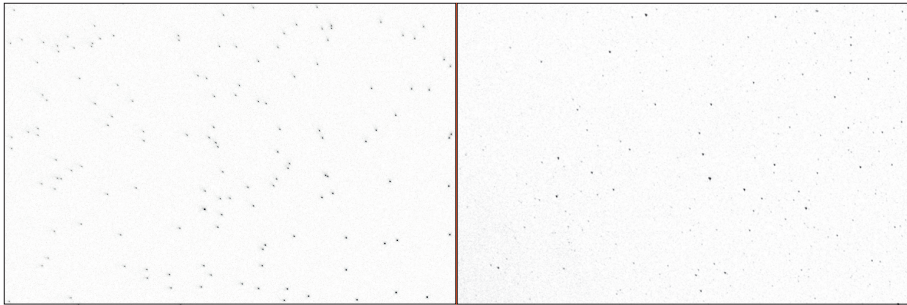
Figure 6.1: An example of the top-left quadrant of the simulated field of objects in comparison to a real-sky image.

Tables of N-gon polynomials

Table A.1: Table of square polynomials $S_j(x, y)$ in Cartesian coordinates.

$S_j(x, y)$	Polynomial
S_1	1
S_2	$6^{1/2}x$
S_3	$6^{1/2}y$
S_4	$10^{1/2}((3x^2)/2 + (3y^2)/2 - 1/2)$
S_5	$310^{1/2}xy$
S_6	$3x^2 - 3y^2$
S_7	$(651^{1/2}y(15x^2 + 15y^2 - 7))/31$
S_8	$(651^{1/2}x(15x^2 + 15y^2 - 7))/31$
S_9	$(2155^{1/2}y(33x^2 + 2y^2 - 3))/31$
S_{10}	$-(2155^{1/2}x(2x^2 + 33y^2 - 3))/31$
S_{11}	$(215^{1/2}67^{1/2}(5^{1/2}(6(x^2 + y^2)^2 - 6x^2 - 6y^2 + 1) + (5^{1/2}(150x^2 + 150y^2 - 43))/105))/268$
S_{12}	$16.202x^4 - 9.7211x^2 + 9.7211y^2 - 16.202y^4$
S_{13}	$(53033xy(7.0x^2 + 7.0y^2 - 3.0))/5000$
S_{14}	$9.7185x^2 - 106.9x^2y^2 - 10.042x^4 + 9.7185y^2 - 10.042y^4 - 0.71269$
S_{15}	$32.404xy(x^2 - 1.0y^2)$
S_{16}	$0.000017405x(730366.0x^2 + 1.1532E6y^2 - 360388.0) + 5.2687x(10.0(x^2 + y^2)^2 - 12.0x^2 - 12.0y^2 + 3.0)$
S_{17}	$0.000017405y(1.1532E6x^2 + 730366.0y^2 - 360388.0) + 5.2687y(10.0(x^2 + y^2)^2 - 12.0x^2 - 12.0y^2 + 3.0)$
S_{18}	$-(x(1.0123E7x^2y^2 - 498566.0x^2 + 197911.0x^4 - 5.2574E6y^2 + 9.9254E6y^4 + 221100.0))/50000$
S_{19}	$(y(1.0123E7x^2y^2 - 5.2574E6x^2 + 9.9254E6x^4 - 498566.0y^2 + 197911.0y^4 + 221100.0))/50000$
S_{20}	$-(x(3.0399E7x^2y^2 - 2.5502E6x^2 + 2.4306E6x^4 - 5.6194E6y^2 + 4.7054E6y^4 + 372377.0))/100000$
S_{21}	$-(y(3.0399E7x^2y^2 - 5.6194E6x^2 + 4.7054E6x^4 - 2.5502E6y^2 + 2.4306E6y^4 + 372377.0))/100000$
S_{22}	$59.144x^2y^2 - 119.84(x^2 + y^2)^2 + 79.896(x^2 + y^2)^3 + 31.336x^2 + 21.271x^4 + 31.336y^2 + 21.271y^4 - 2.1444$
S_{23}	$(xy(3.803E6x^2y^2 - 1.6134E6x^2 + 1.9015E6x^4 - 1.6134E6y^2 + 1.9015E6y^4 + 311155.0))/5000$
S_{24}	$4.8151(x^2 - 1.0y^2)(15.0(x^2 + y^2)^2 - 20.0x^2 - 20.0y^2 + 6.0) + 0.0045858(x^2 - 1.0y^2)(2800.0x^2 + 2800.0y^2 - 1590.0)$

Table A.1 – continued from previous page

$S_j(x,y)$	Polynomial
S_{25}	$-0.001xy(142177.0x^2 - 255911.0x^4 - 142177.0y^2 + 255911.0y^4)$
S_{26}	$574.9x^2y^2 - 1079.7x^2y^4 - 1079.7x^4y^2 - 25.933x^2 + 76.512x^4 - 53.964x^6 - 25.933y^2 + 76.512y^4 - 53.964y^6 + 1.0511$
S_{27}	$-(xy(1.285E7x^2y^2 - 2.53E6x^2 + 2.5686E6x^4 - 2.53E6y^2 + 2.5686E6y^4 + 350200.0))/10000$
S_{28}	$338.14x^2y^4 - 338.14x^4y^2 - 3.6832x^2 + 29.042x^4 - 28.114x^6 + 3.6832y^2 - 29.042y^4 + 28.114y^6$
S_{29}	$6.3607y(35.0(x^2 + y^2)^3 - 60.0(x^2 + y^2)^2 + 30.0x^2 + 30.0y^2 - 4.0) + 0.00098845y(190233.0x^2y^2 - 91815.0x^2 + 118900.0x^4 - 57515.0y^2 + 57165.0y^4 + 11787.0)$
S_{30}	$6.3607x(35.0(x^2 + y^2)^3 - 60.0(x^2 + y^2)^2 + 30.0x^2 + 30.0y^2 - 4.0) + 0.00098845x(190233.0x^2y^2 - 57515.0x^2 + 57165.0x^4 - 91815.0y^2 + 118900.0y^4 + 11787.0)$
S_{31}	$(y(1.0572E8x^2y^4 - 9.9281E7x^2y^2 + 2.092E8x^4y^2 + 2.4831E7x^2 - 1.0364E8x^4 + 1.0422E8x^6 + 2.315E6y^2 - 2.641E6y^4 + 749799.0y^6 - 614766.0))/100000$
S_{32}	$-(x(2.092E8x^2y^4 - 9.9281E7x^2y^2 + 1.0572E8x^4y^2 + 2.315E6x^2 - 2.641E6x^4 + 749799.0x^6 + 2.4831E7y^2 - 1.0364E8y^4 + 1.0422E8y^6 - 614766.0))/100000$
S_{33}	$-(y(2.9204E8x^2y^4 - 1.8201E8x^2y^2 + 3.0121E8x^4y^2 + 1.682E7x^2 - 4.1429E7x^4 + 2.2686E7x^6 + 8.1479E6y^2 - 2.0458E7y^4 + 1.3512E7y^6 - 678777.0))/100000$
S_{34}	$-(x(3.0121E8x^2y^4 - 1.8201E8x^2y^2 + 2.9204E8x^4y^2 + 8.1479E6x^2 - 2.0458E7x^4 + 1.3512E7x^6 + 1.682E7y^2 - 4.1429E7y^4 + 2.2686E7y^6 - 678777.0))/100000$
S_{35}	$-(y(2.3543E7x^2y^4 - 2.6723E7x^2y^2 + 9.1688E7x^4y^2 + 3.6004E6x^2 - 1.7595E7x^4 + 1.6378E7x^6 + 779988.0y^2 - 1.1926E6y^4 + 481666.0y^6 - 92317.0))/25000$
S_{36}	$(x(9.1688E7x^2y^4 - 2.6723E7x^2y^2 + 2.3543E7x^4y^2 + 779988.0x^2 - 1.1926E6x^4 + 481666.0x^6 + 3.6004E6y^2 - 1.7595E7y^4 + 1.6378E7y^6 - 92317.0))/25000$
S_{37}	$441.04x^2y^4 - 339.59x^2y^2 + 441.04x^4y^2 + 428.07(x^2 + y^2)^2 - 665.89(x^2 + y^2)^3 + 332.94(x^2 + y^2)^4 - 55.321x^2 - 118.78x^4 + 91.668x^6 - 55.321y^2 - 118.78y^4 + 91.668y^6 + 2.3448$
S_{38}	$7.9915E - 13(x^2 - 1.0y^2)^2(1.1398E14x^2y^2 - 8.125E13x^2 + 7.2915E13x^4 - 8.125E13y^2 + 7.2915E13y^4 + 1.9811E13) + 5.54(x^2 - 1.0y^2)(56.0(x^2 + y^2)^3 - 105.0(x^2 + y^2)^2 + 60.0x^2 + 60.0y^2 - 10.0)$
S_{39}	$0.015156xy(151977.0x^2y^2 - 69060.0x^2 + 70161.0x^4 - 69060.0y^2 + 70161.0y^4 + 14610.0) + 32.509xy(56.0(x^2 + y^2)^3 - 105.0(x^2 + y^2)^2 + 60.0x^2 + 60.0y^2 - 10.0)$
S_{40}	$6329.5x^2y^4 - 1573.1x^2y^2 + 6329.5x^4y^2 - 6587.7x^2y^6 - 12734.0x^4y^4 - 6587.7x^6y^2 + 45.422x^2 - 235.7x^4 + 408.22x^6 - 220.95x^8 + 45.422y^2 - 235.7y^4 + 408.22y^6 - 220.95y^8 - 1.2159$
S_{41}	$50.344xy(x^2 - 1.0y^2)(28.0(x^2 + y^2)^2 - 42.0x^2 - 42.0y^2 + 15.0) + 0.0011176xy(x^2 - 1.0y^2)(494800.0x^2 + 494800.0y^2 - 309022.0)$
S_{42}	$1981.5x^2y^4 - 1981.5x^4y^2 - 3540.5x^2y^6 + 3540.5x^6y^2 - 9.1219x^2 + 110.48x^4 - 263.86x^6 + 167.76x^8 + 9.1219y^2 - 110.48y^4 + 263.86y^6 - 167.76y^8$
S_{43}	$-(xy(7.7562E7x^2y^4 - 4.9849E7x^2y^2 + 7.7562E7x^4y^2 + 4.9476E6x^2 - 1.2864E7x^4 + 8.8896E6x^6 + 4.9476E6y^2 - 1.2864E7y^4 + 8.8896E6y^6 - 404522.0))/5000$
S_{44}	$1026.4x^2y^2 - 5077.3x^2y^4 - 5077.3x^4y^2 + 4863.1x^2y^6 + 16190.0x^4y^4 + 4863.1x^6y^2 - 25.294x^2 + 152.32x^4 - 256.58x^6 + 130.03x^8 - 25.294y^2 + 152.32y^4 - 256.58y^6 + 130.03y^8 + 0.58427$
S_{45}	$-0.002xy(1.7919E6x^2y^4 - 1.7919E6x^4y^2 - 62170.0x^2 + 389600.0x^4 - 381111.0x^6 + 62170.0y^2 - 389600.0y^4 + 381111.0y^6)$

Table A.2: Table of pentagon polynomials $P_j(x, y)$ in Cartesian coordinates.

$P_j(x,y)$	Polynomial
P_1	1
P_2	$(233^{1/2}x(7 - 5^{1/2})^{1/2})/11$
P_3	$(233^{1/2}y(7 - 5^{1/2})^{1/2})/11$
P_4	$-(246^{1/2}(13 - 5^{1/2})^{1/2}((73^{1/2})/12 + 15^{1/2}/12 - 23^{1/2}x^2 - 23^{1/2}y^2))/41$
P_5	$(610^{1/2}xy(5 - 5^{1/2})^{1/2})/5$
P_6	$(310^{1/2}(x^2 - y^2)(5 - 5^{1/2})^{1/2})/5$
P_7	$-(4346899^{1/2}y(433 - 345^{1/2})^{1/2}(152^{1/2} + 10^{1/2} - 332^{1/2}x^2 - 332^{1/2}y^2))/181709$
P_8	$-(4346899^{1/2}x(433 - 345^{1/2})^{1/2}(152^{1/2} + 10^{1/2} - 332^{1/2}x^2 - 332^{1/2}y^2))/181709$
P_9	$-(23649^{1/2}(235 - 865^{1/2})^{1/2}(302^{1/2}x^2 - 610^{1/2}x^2 - 302^{1/2}y^2 + 702^{1/2}y^3 + 610^{1/2}y^2 - 2102^{1/2}x^2y))/18245$
P_{10}	$-(43649^{1/2}x(235 - 865^{1/2})^{1/2}(302^{1/2}y - 610^{1/2}y - 352^{1/2}x^2 + 1052^{1/2}y^2))/18245$
P_{11}	$36.751x^2y^2 - 14.913x^2 + 18.375x^4 - 14.913y^2 + 18.375y^4 + 2.0455$
P_{12}	$19.307x^4 - 11.148x^2 - 5.1382x^2y + 11.148y^2 + 1.7127y^3 - 19.307y^4$
P_{13}	$(x(3.8614E6x^2y - 2.2297E6y - 171277.0x^2 + 513822.0y^2 + 3.8614E6y^3))/100000$
P_{14}	$1.8935y - 45.897x^2y^2 + 5.7371(x^2 + y^2)^2 - 4.9845x^2y - 4.9845y^3$
P_{15}	$-0.00001x(498455.0x^2 - 2.2948E6x^2y + 498455.0y^2 + 2.2948E6y^3 - 189355.0)$
P_{16}	$1.4836E - 32x(8.0651E32x^2 - 6.0477E32x^2y + 8.0651E32y^2 + 6.0477E32y^3 - 3.5335E32) + 5.1395x(10.0(x^2 + y^2)^2 - 12.0x^2 - 12.0y^2 + 3.0)$
P_{17}	$10.176y + 13.459x^2y^2 + 102.79x^2y^3 - 49.708x^2y + 51.395x^4y - 2.2432x^4 - 49.708y^3 - 2.2432y^4 + 51.395y^5$
P_{18}	$-0.0001x(616166.0x^2y^2 - 103155.0y + 220866.0x^2y + 185688.0x^2 - 308088.0x^4 - 557055.0y^2 + 220866.0y^3 + 924244.0y^4)$
P_{19}	$61.616x^2y^3 - 55.705x^2y + 92.424x^4y + 5.1576x^2 - 11.043x^4 - 5.1576y^2 + 18.568y^3 + 11.043y^4 - 30.808y^5$
P_{20}	$35.908xy^4 - 71.816x^3y^2 + 7.1816x^5$
P_{21}	$40.016x^4y - 80.031x^2y^3 - 28.24x^2y^2 + 8.4576x^2 - 14.12x^4 + 8.4576y^2 - 14.12y^4 + 8.0031y^5 - 0.79777$
P_{22}	$46.991x^2y^2 + 40.562x^2y^3 - 122.45(x^2 + y^2)^2 + 81.632(x^2 + y^2)^3 - 20.281x^4y + 32.579x^2 + 23.496x^4 + 32.579y^2 + 23.496y^4 - 4.0562y^5 - 2.274$
P_{23}	$3.338E - 32x(1.0774E33x^2y^2 - 8.1575E32y + 1.5614E33x^2y + 2.86E32x^2 - 5.3871E32x^4 - 8.58E32y^2 + 1.5614E33y^3 + 1.6161E33y^4) + 12.49xy(15.0(x^2 + y^2)^2 - 20.0x^2 - 20.0y^2 + 6.0)$
P_{24}	$93.673x^4y^2 - 93.673x^2y^4 - 35.965x^2y^3 + 28.64x^2y - 53.947x^4y + 23.854x^2 - 98.838x^4 + 93.673x^6 - 23.854y^2 - 9.5467y^3 + 98.838y^4 + 17.982y^5 - 93.673y^6$
P_{25}	$-0.0001x(722399.0x^2y^2 + 1.1603E6x^2y - 1.8733E6x^4y - 279499.0x^2 + 361200.0x^4 - 279499.0y^2 - 1.1603E6y^3 + 361200.0y^4 + 1.8733E6y^5 + 43638.0)$
P_{26}	$174.04x^2y^2 - 4.3638y - 72.239x^2y^3 - 234.17x^2y^4 - 234.17x^4y^2 + 27.949x^2y - 36.12x^4y - 29.007x^4 + 46.833x^6 + 27.949y^3 - 29.007y^4 - 36.12y^5 + 46.833y^6$
P_{27}	$-0.00001x(7.0243E6x^2y^2 + 1.9989E7x^2y^3 + 1.1644E6x^2y - 8.6276E6x^4y - 2.5956E6x^2 + 3.5122E6x^4 - 2.5956E6y^2 - 1.1644E6y^3 + 3.5122E6y^4 - 3.3656E6y^5 + 386244.0)$
P_{28}	$3.8624y - 17.466x^2y^2 + 70.243x^2y^3 + 182.8x^2y^4 - 117.03x^4y^2 - 25.956x^2y + 35.122x^4y + 2.9109x^4 + 3.4168x^6 - 25.956y^3 + 2.9109y^4 + 35.122y^5 - 16.572y^6$
P_{29}	$192.26x^2y^4 - 94.297x^2y^2 - 641.77x^2y^3 - 14.439y + 82.905x^4y^2 + 704.15x^2y^5 + 704.15x^4y^3 + 130.54x^2y - 320.88x^4y + 234.72x^6y + 15.716x^4 - 23.872x^6 + 130.54y^3 + 15.716y^4 - 320.88y^5 - 31.162y^6 + 234.72y^7$

Continued on next page

Table A.2 – continued from previous page

$P_j(x,y)$	Polynomial
P_{30}	$6.7062x(35.0(x^2+y^2)^3 - 60.0(x^2+y^2)^2 + 30.0x^2 + 30.0y^2 - 4.0) + 3.3531E-32x(4.8604E33x^2y^2 + 2.1743E33x^2y^3 + 1.8748E33x^2y - 3.9349E33x^4y - 2.1068E33x^2 + 2.4302E33x^4 - 2.1068E33y^2 - 1.8748E33y^3 + 2.4302E33y^4 + 2.6303E33y^5 + 3.6937E32)$
P_{31}	$68.805x^2y^4 - 356.44x^2y^3 - 68.805x^4y^2 + 159.5x^2y^5 + 797.52x^4y^3 + 141.38x^2y - 534.67x^4y + 478.51x^6y - 12.612x^2 + 62.731x^4 - 68.805x^6 + 12.612y^2 - 47.126y^3 - 62.731y^4 + 178.22y^5 + 68.805y^6 - 159.5y^7$
P_{32}	$7.5954x(x^2 - 3.0y^2)(21.0(x^2+y^2)^2 - 30.0x^2 - 30.0y^2 + 10.0) - 1.8989E-31x(1.3284E32y + 5.2285E32x^2y^2 + 1.4494E33x^2y^3 - 6.6072E32x^2y + 7.247E32x^4y + 1.5182E32x^2 - 2.6143E32x^4 - 4.5547E32y^2 - 6.6072E32y^3 + 7.8428E32y^4 + 7.247E32y^5)$
P_{33}	$205.35x^2y^2 + 459.43x^2y^3 - 314.89x^2y^4 - 314.89x^4y^2 - 689.59x^2y^5 - 383.1x^4y^3 - 229.71x^4y - 383.1x^6y - 26.254x^2 + 102.68x^4 - 104.96x^6 - 26.254y^2 + 102.68y^4 - 45.943y^5 - 104.96y^6 + 76.621y^7 + 1.354$
P_{34}	$-0.0004x(799611.0x^2y^4 - 1.0529E6x^2y^2 + 1.4393E6x^4y^2 + 105299.0x^4 - 159922.0x^6 + 526444.0y^4 - 799611.0y^6)$
P_{35}	$70.557x^2y^4 - 36.875x^2y^3 - 4.788E-39x^2y^2 - 70.557x^4y^2 + 298.46x^2y^5 - 332.51x^4y^3 + 8.8852x^2y - 55.312x^4y + 165.45x^6y - 10.843x^2 + 58.969x^4 - 70.557x^6 + 10.843y^2 - 2.9617y^3 - 58.969y^4 + 18.437y^5 + 70.557y^6 - 37.771y^7$
P_{36}	$-(x(3.6875E6x^2y^2 - 2.1687E6y - 2.8223E7x^2y^3 - 5.7988E7x^2y^4 + 2.4898E7x^4y^2 + 1.1794E7x^2y - 1.4111E7x^4y + 296177.0x^2 - 1.8437E6x^4 + 1.1703E6x^6 - 888522.0y^2 + 1.1794E7y^3 + 5.5312E6y^4 - 1.4111E7y^5 + 1.7029E6y^6))/100000$
P_{37}	$469.56x^2y^4 - 343.09x^2y^3 - 346.19x^2y^2 + 469.56x^4y^2 + 518.47x^2y^5 + 288.04x^4y^3 + 477.19(x^2+y^2)^2 - 742.29(x^2+y^2)^3 + 371.15(x^2+y^2)^4 + 171.55x^4y - 288.04x^6y - 55.81x^2 - 173.1x^4 + 156.52x^6 - 55.81y^2 - 173.1y^4 + 34.309y^5 + 156.52y^6 - 57.608y^7 + 2.3539$
P_{38}	$241.8x^2y^3 + 651.88x^2y^4 - 651.88x^4y^2 - 213.25x^2y^5 - 443.62x^4y^3 - 878.49x^2y^6 + 878.49x^6y^2 - 84.357x^2y + 362.7x^4y - 390.7x^6y - 41.051x^2 + 300.2x^4 - 651.88x^6 + 439.25x^8 + 41.051y^2 + 28.119y^3 - 300.2y^4 - 120.9y^5 + 651.88y^6 + 124.3y^7 - 439.25y^8$
P_{39}	$1.8488E-31x(4.0444E32y - 1.3079E33x^2y^2 + 3.715E33x^2y^3 + 4.0834E33x^2y^4 + 1.4313E32x^4y^2 - 1.8436E33x^2y + 1.8575E33x^4y - 1.5209E32x^2 + 6.5395E32x^4 - 6.2424E32x^6 + 4.5628E32y^2 - 1.8436E33y^3 - 1.9618E33y^4 + 1.8575E33y^5 + 1.7765E33y^6) + 15.687xy(56.0(x^2+y^2)^3 - 105.0(x^2+y^2)^2 + 60.0x^2 + 60.0y^2 - 10.0)$
P_{40}	$7.3894y - 507.51x^2y^2 + 488.49x^2y^3 + 1473.8x^2y^4 + 1555.8x^4y^2 - 620.38x^2y^5 - 620.38x^4y^3 - 1046.3x^2y^6 - 2615.7x^4y^4 - 1046.3x^6y^2 - 83.093x^2y + 244.24x^4y - 206.79x^6y + 84.585x^4 - 305.69x^6 + 261.57x^8 - 83.093y^3 + 84.585y^4 + 244.24y^5 - 300.23y^6 - 206.79y^7 + 261.57y^8$
P_{41}	$37.367xy(x^2 - 1.0y^2)(28.0(x^2+y^2)^2 - 42.0x^2 - 42.0y^2 + 15.0) - 4.4037E-32x(1.2409E33x^2y^3 - 1.1093E34x^2y^2 + 1.4088E34x^2y^4 + 1.4088E34x^4y^2 + 5.0449E33x^2y - 8.492E33x^4y + 1.8869E33x^2 - 5.5463E33x^4 + 4.6959E33x^6 + 1.8869E33y^2 - 5.0449E33y^3 - 5.5463E33y^4 + 7.7475E33y^5 + 4.6959E33y^6 - 1.678E32)$
P_{42}	$8.2665y - 42.523x^2y^2 + 597.48x^2y^3 + 1180.8x^2y^4 - 762.91x^4y^2 - 792.61x^2y^5 - 792.61x^4y^3 - 1652.9x^2y^6 - 530.59x^4y^4 + 1228.4x^6y^2 - 97.224x^2y + 298.74x^4y - 264.2x^6y + 7.0872x^4 + 23.005x^6 - 49.844x^8 - 97.224y^3 + 7.0872y^4 + 298.74y^5 - 106.57y^6 - 264.2y^7 + 155.96y^8$
P_{43}	$-0.00002x(3.963E7x^2y^4 - 6.4789E7x^2y^3 - 2.9874E7x^2y^2 + 3.963E7x^4y^2 + 8.2644E7x^2y^5 + 6.142E7x^4y^3 - 1.4174E6x^2y + 2.7793E7x^4y - 4.1483E7x^6y + 4.8612E6x^2 - 1.4937E7x^4 + 1.321E7x^6 + 4.8612E6y^2 + 1.4174E6y^3 - 1.4937E7y^4 + 1.108E7y^5 + 1.321E7y^6 - 2.0259E7y^7 - 413333.0)$

Continued on next page

$P_j(x,y)$	Polynomial
P_{44}	$69.451x^4y^2 - 236.14x^2y^3 - 69.451x^2y^4 - 3.3307E - 39x^2y^2 + 160.32x^2y^5 + 602.68x^4y^3 - 325.8x^2y^6 + 1183.8x^4y^4 - 621.26x^6y^2 + 73.637x^2y - 354.21x^4y + 401.39x^6y + 1.0461x^2 - 17.792x^4 + 69.451x^6 - 56.954x^8 - 1.0461y^2 - 24.546y^3 + 17.792y^4 + 118.07y^5 - 69.451y^6 - 131.9y^7 + 90.778y^8$
P_{45}	$-(x(1.4043E7x^2y^4 - 4.7228E6x^2y^2 - 5.5561E6x^2y^3 - 41843.0y + 2.0129E6x^4y^2 + 2.7805E7x^2y^5 - 1.0077E7x^4y^3 + 711677.0x^2y - 2.778E6x^4y + 5.6605E6x^6y - 490922.0x^2 + 2.3614E6x^4 - 2.5812E6x^6 + 1.4728E6y^2 + 711677.0y^3 - 7.0843E6y^4 - 2.778E6y^5 + 7.6299E6y^6 + 248766.0y^7))/20000$

Table A.3: Table of hexagon polynomials $Hx_j(x,y)$ in Cartesian coordinates.

$Hx_j(x,y)$	Polynomial
Hx_1	1
Hx_2	$(230^{1/2}x)/5$
Hx_3	$(230^{1/2}y)/5$
Hx_4	$215^{1/2}((12x^2)/43 + (12y^2)/43 - 5/43)$
Hx_5	$(4105^{1/2}xy)/7$
Hx_6	$(6^{1/2}7^{1/2}10^{1/2}(x^2 - y^2))/7$
Hx_7	$(4154770^{1/2}y(25x^2 + 25y^2 - 14))/3685$
Hx_8	$(4154770^{1/2}x(25x^2 + 25y^2 - 14))/3685$
Hx_9	$(47210^{1/2}y(3x^2 - y^2))/103$
Hx_{10}	$(410^{1/2}x(x^2 - 3y^2))/3$
Hx_{11}	$(1443^{1/2}4987^{1/2}(5^{1/2}(6(x^2 + y^2)^2 - 6x^2 - 6y^2 + 1) + (5^{1/2}(2640x^2 + 2640y^2 - 799))/3010))/4987$
Hx_{12}	$16.756x^4 - 10.643x^2 + 10.643y^2 - 16.756y^4$
Hx_{13}	$(3xy(55853.0x^2 + 55853.0y^2 - 35478.0))/5000$
Hx_{14}	$10.085x^4 - 2.6291x^2 - 28.75x^2y^2 + 2.6291y^2 - 0.50191y^4$
Hx_{15}	$(xy(857944.0x^2 - 2.9754E6y^2 + 525811.0))/100000$
Hx_{16}	$0.00014843x(49168.0x^2 + 49168.0y^2 - 22493.0) + 4.5944x(10.0(x^2 + y^2)^2 - 12.0x^2 - 12.0y^2 + 3.0)$
Hx_{17}	$0.00014843y(49168.0x^2 + 49168.0y^2 - 22493.0) + 4.5944y(10.0(x^2 + y^2)^2 - 12.0x^2 - 12.0y^2 + 3.0)$
Hx_{18}	$5.4489x(x^2 - 3.0y^2) + 6.3571x(x^2 - 3.0y^2)(5.0x^2 + 5.0y^2 - 4.0)$
Hx_{19}	$1.7612y(3.0x^2 - 1.0y^2) + 4.2296y(3.0x^2 - 1.0y^2)(5.0x^2 + 5.0y^2 - 4.0)$
Hx_{20}	$-0.0001x(272822.0x^2y^2 + 132366.0x^2 - 221155.0x^4 + 132366.0y^2 - 459522.0y^4 - 21760.0)$
Hx_{21}	$-0.0001y(919044.0x^2y^2 - 132366.0x^2 - 136411.0x^4 - 132366.0y^2 + 101966.0y^4 + 21760.0)$
Hx_{22}	$23.893x^2y^2 - 105.03(x^2 + y^2)^2 + 70.017(x^2 + y^2)^3 + 33.148x^2 + 11.947x^4 + 33.148y^2 + 11.947y^4 - 2.4706$
Hx_{23}	$(xy(1.5702E6x^2y^2 - 934144.0x^2 + 785122.0x^4 - 879288.0y^2 + 785122.0y^4 + 237299.0))/5000$
Hx_{24}	$78.512x^4y^2 - 78.512x^2y^4 - 8.2298x^2y^2 + 23.729x^2 - 89.3x^4 + 78.512x^6 - 23.729y^2 + 92.043y^4 - 78.512y^6$
Hx_{25}	$-0.0001xy(1.5183E6x^2y^2 + 344399.0x^2 - 816822.0x^4 - 1.7896E6y^2 + 2.3351E6y^4 + 151066.0)$
Hx_{26}	$160.05x^2y^2 - 234.95x^2y^4 - 159.04x^4y^2 + 7.5528x^2 - 62.805x^4 + 77.356x^6 - 7.5528y^2 + 9.4554y^4 + 1.4422y^6$
Hx_{27}	$40.855xy^5 - 136.18x^3y^3 + 40.855x^5y$

Table A.3 – continued from previous page

$Hx_j(x, y)$	Polynomial
Hx_{28}	$229.43x^2y^4 - 77.426x^2y^2 - 5.7698x^4y^2 + 10.448x^2 - 38.713x^4 + 45.117x^6 + 10.448y^2 - 38.713y^4 + 29.437y^6 - 0.56537$
Hx_{29}	$5.4564y(35.0(x^2 + y^2)^3 - 60.0(x^2 + y^2)^2 + 30.0x^2 + 30.0y^2 - 4.0) + 9.9215E - 11y(8.7273E11x^2y^2 - 3.388E11x^2 + 2.9388E11x^4 - 3.388E11y^2 + 3.5087E11y^4 + 6.306E10)$
Hx_{30}	$5.4564x(35.0(x^2 + y^2)^3 - 60.0(x^2 + y^2)^2 + 30.0x^2 + 30.0y^2 - 4.0) + 9.9215E - 11x(5.8776E11x^2y^2 - 3.388E11x^2 + 3.7937E11x^4 - 3.388E11y^2 + 4.3636E11y^4 + 6.306E10)$
Hx_{31}	$2.4846E - 21y(3.0x^2 - 1.0y^2)(4.7119E21x^2 + 4.7119E21y^2 - 2.9756E21) + 4.8994y(3.0x^2 - 1.0y^2)(21.0(x^2 + y^2)^2 - 30.0x^2 - 30.0y^2 + 10.0)$
Hx_{32}	$7.7733E - 6x(x^2 - 3.0y^2)(6.5082E6x^2 + 6.5082E6y^2 - 3.8839E6) + 8.4476x(x^2 - 3.0y^2)(21.0(x^2 + y^2)^2 - 30.0x^2 - 30.0y^2 + 10.0)$
Hx_{33}	$-0.00005y(1.5547E7x^2y^4 - 1.2312E7x^2y^2 + 1.1163E7x^4y^2 + 836855.0x^2 + 1.4534E6x^4 - 3.5859E6x^6 + 836855.0y^2 - 1.5903E6y^4 + 798266.0y^6 - 77505.0)$
Hx_{34}	$(x(2.9067E6x^2y^2 + 202733.0x^2y^4 - 4.1814E6x^4y^2 + 836855.0x^2 - 3.1122E6x^4 + 2.9903E6x^6 + 836855.0y^2 - 6.1559E6y^4 + 7.3744E6y^6 - 77505.0))/20000$
Hx_{35}	$-0.00001y(2.6428E7x^2y^2 - 5.3582E7x^2y^4 + 753577.0x^4y^2 - 3.4935E6x^2 + 7.2021E6x^4 - 9.7453E6x^6 - 3.4935E6y^2 + 9.6069E6y^4 - 6.6204E6y^6 + 310311.0)$
Hx_{36}	$-0.00001x(1.4404E7x^2y^2 - 5.1949E7x^2y^4 + 2.3858E6x^4y^2 - 3.4935E6x^2 + 1.0809E7x^4 - 1.0445E7x^6 - 3.4935E6y^2 + 1.3214E7y^4 - 7.3199E6y^6 + 310311.0)$
Hx_{37}	$207.58x^2y^4 - 141.55x^2y^2 + 146.86x^4y^2 + 371.0(x^2 + y^2)^2 - 577.11(x^2 + y^2)^3 + 288.55(x^2 + y^2)^4 - 60.399x^2 - 70.777x^4 + 61.097x^6 - 60.399y^2 - 70.777y^4 + 57.048y^6 + 2.7453$
Hx_{38}	$50.987x^2y^2 + 497.21x^2y^4 - 633.06x^4y^2 - 679.97x^2y^6 + 679.97x^6y^2 - 42.962x^2 + 279.29x^4 - 551.55x^6 + 339.98x^8 + 42.962y^2 - 296.28y^4 + 578.72y^6 - 339.98y^8$
Hx_{39}	$12.142xy(56.0(x^2 + y^2)^3 - 105.0(x^2 + y^2)^2 + 60.0x^2 + 60.0y^2 - 10.0) + 5.2752E - 16xy(5.4846E17x^2y^2 - 2.2554E17x^2 + 1.7122E17x^4 - 3.5441E17y^2 + 3.7725E17y^4 + 6.7292E16)$
Hx_{40}	$1686.8x^2y^4 - 500.39x^2y^2 + 1113.3x^4y^2 - 1307.6x^2y^6 - 2250.8x^4y^4 - 493.07x^6y^2 - 14.792x^2 + 205.02x^4 - 566.78x^6 + 428.7x^8 + 14.792y^2 - 38.218y^4 + 6.7669y^6 + 21.456y^8$
Hx_{41}	$(xy(1.1471E7x^2y^2 - 2.122E7x^2y^4 - 3.2142E6x^4y^2 + 903622.0x^2 - 5.4648E6x^4 + 4.9307E6x^6 - 5.7683E6y^2 + 1.6936E7y^4 - 1.3076E7y^6 + 295844.0))/10000$
Hx_{42}	$1913.2x^2y^4 - 316.43x^2y^2 + 155.31x^4y^2 - 2152.3x^2y^6 - 1429.9x^4y^4 + 245.74x^6y^2 + 24.654x^2 - 158.22x^4 + 403.36x^6 - 323.96x^8 + 24.654y^2 - 158.22y^4 + 286.16y^6 - 152.68y^8 - 0.84269$
Hx_{43}	$-0.001xy(938966.0x^2y^4 - 975366.0x^2y^2 + 938966.0x^4y^2 + 292611.0x^4 - 402411.0x^6 + 292611.0y^4 - 402411.0y^6)$
Hx_{44}	$471.48x^2y^4 - 76.057x^2y^2 + 39.322x^4y^2 - 826.9x^2y^6 + 279.13x^4y^4 - 170.83x^6y^2 - 9.6478x^2 + 98.095x^4 - 267.16x^6 + 223.32x^8 + 9.6478y^2 - 72.743y^4 + 165.0y^6 - 104.71y^8$
Hx_{45}	$-(xy(3.5765E6x^2y^4 - 1.7286E6x^2y^2 + 359977.0x^4y^2 + 240277.0x^2 - 455688.0x^4 + 443300.0x^6 + 443088.0y^2 - 1.273E6y^4 + 868855.0y^6 - 38591.0))/2000$

Table A.4: Table of heptagon polynomials $Hp_j(x, y)$ in Cartesian coordinates.

$Hp_j(x,y)$	Polynomial
Hp_1	1
Hp_2	$(421^{1/2}x sin((2pi)/7)^{1/2}(6829 cos((3pi)/7) - 1733 cos((2pi)/7) - 4735 cos(pi/7) + 3827)^{1/2})/(7(7352 sin((2pi)/7) - 5880 sin(pi/7) - 3279 sin((3pi)/7))^{1/2})$
Hp_3	$(43^{1/2}y sin((2pi)/7)^{1/2}(176 cos((2pi)/7) - 182 cos(pi/7) - 174 cos((3pi)/7) + 93)^{1/2})/(Exp((pi1i)/7)30i - Exp((pi2i)/7)36i + Exp((pi3i)/7)25i + 5Exp((pi1i)/14) + 6Exp((pi3i)/14) - 15i)^{1/2}$
Hp_4	$y(2.3633E - 11 - 6.9972E - 13i) + x^2(3.929 - 3.2085E - 23i) + y^2(3.929 - 3.2085E - 23i) - (1.718 + 4.6581E - 12i)$
Hp_5	$xy(5.5906 - 2.4576E - 13i)$
Hp_6	$x^2(2.7953 + 3.4782E - 23i) - y(4.6035E - 11 - 1.2493E - 12i) - y^2(2.7953 + 3.4782E - 23i)$
Hp_7	$y(0.8242 - 5.2613E - 14i) + y(3.0x^2 + 3.0y^2 - 2.0)(3.3806 + 2.1955E - 25i)$
Hp_8	$x(0.8242 + 1.0945E - 10i) + x(3.0x^2 + 3.0y^2 - 2.0)(3.3806 - 1.2114E - 19i)$
Hp_9	$y(3.0x^2 - 1.0y^2)(3.4372 + 2.2824E - 23i) - y(2.9546E - 11 - 1.084E - 12i)$
Hp_{10}	$3.4372x(x^2 - 3.0y^2)$
Hp_{11}	$16.616(x^2 + y^2)^2 - 14.715x^2 - 14.715y^2 + 2.1808$
Hp_{12}	$15.83x^4 - 10.469x^2 + 10.469y^2 - 15.83y^4$
Hp_{13}	$(xy(316600.0x^2 + 316600.0y^2 - 209399.0))/10000$
Hp_{14}	$4.1634(x^2 + y^2)^2 - 33.307x^2y^2 + 2.0495x^2y - 0.68316y^3$
Hp_{15}	$0.68316x(x^2 - 3.0y^2) + 16.653xy(x^2 - 1.0y^2)$
Hp_{16}	$(x(880933.0x^2y^2 - 472100.0x^2 + 440466.0x^4 - 472100.0y^2 + 440466.0y^4 + 105844.0))/10000$
Hp_{17}	$(y(880933.0x^2y^2 - 472100.0x^2 + 440466.0x^4 - 472100.0y^2 + 440466.0y^4 + 105844.0))/10000$
Hp_{18}	$2.2917x(x^2 - 3.0y^2) + 4.6444x(x^2 - 3.0y^2)(5.0x^2 + 5.0y^2 - 4.0) + 4.0739xy(x^2 - 1.0y^2)$
Hp_{19}	$46.444x^2y^3 - 6.1109x^2y^2 - 48.858x^2y + 69.666x^4y + 1.0185x^4 + 16.286y^3 + 1.0185y^4 - 23.222y^5$
Hp_{20}	$4.9748x(5.0(x^2 + y^2)^2 - 20.0x^2(x^2 + y^2) + 16.0x^4) + 2.8722E - 32xy(2.7648E32x^2 + 2.7648E32y^2 - 1.4526E32)$
Hp_{21}	$24.874x^4y - 49.748x^2y^3 - 2.0861x^2 + 3.9706x^4 + 2.0861y^2 - 3.9706y^4 + 4.9748y^5$
Hp_{22}	$67.795(x^2 + y^2)^3 - 91.961(x^2 + y^2)^2 + 33.378x^2 + 33.378y^2 - 2.5325$
Hp_{23}	$2.6831E - 33x(8.2163E33x^2y - 4.942E33x^2y^2 - 4.5839E33y + 4.942E32x^4 + 8.2163E33y^3 + 2.471E33y^4) + 10.039xy(15.0(x^2 + y^2)^2 - 20.0x^2 - 20.0y^2 + 6.0)$
Hp_{24}	$75.295x^4y^2 - 75.295x^2y^4 - 13.26x^2y^3 + 6.6301x^4y + 23.968x^2 - 89.371x^4 + 75.295x^6 - 23.968y^2 + 89.371y^4 + 1.326y^5 - 75.295y^6$
Hp_{25}	$-0.00001x(1.472E6x^2y^2 + 9.4415E6x^2y - 1.3014E7x^4y + 433266.0x^2 - 736011.0x^4 - 1.2998E6y^2 - 9.4415E6y^3 + 2.208E6y^4 + 1.3014E7y^5)$
Hp_{26}	$141.62x^2y^2 + 14.72x^2y^3 - 162.68x^2y^4 - 162.68x^4y^2 - 12.998x^2y + 22.08x^4y - 23.604x^4 + 32.536x^6 + 4.3326y^3 - 23.604y^4 - 7.3601y^5 + 32.536y^6$
Hp_{27}	$1.573E - 32x(1.6304E33x^2y^2 - 7.1055E32x^2 + 8.1518E32x^4 - 7.1055E32y^2 + 8.1518E32y^4 + 1.2412E32) + 5.8856xy(6.0(x^2 + y^2)^2 - 32.0x^2(x^2 + y^2) + 32.0x^4)$
Hp_{28}	$1.9524y + 25.645x^2y^3 + 88.284x^2y^4 - 88.284x^4y^2 - 11.177x^2y + 12.823x^4y + 5.8856x^6 - 11.177y^3 + 12.823y^5 - 5.8856y^6$
Hp_{29}	$23.019x^2y^4 - 577.12x^2y^3 - 15.891y - 23.019x^4y^2 + 558.66x^2y^5 + 558.66x^4y^3 + 130.9x^2y - 288.56x^4y + 186.22x^6y + 1.5346x^6 + 130.9y^3 - 288.56y^5 - 1.5346y^6 + 186.22y^7$
Hp_{30}	$5.3206x(35.0(x^2 + y^2)^3 - 60.0(x^2 + y^2)^2 + 30.0x^2 + 30.0y^2 - 4.0) + 1.3302E - 32x(4.6123E33x^2y^2 - 2.3074E33x^2y^3 + 6.9223E32x^4y - 2.1593E33x^2 + 2.3062E33x^4 - 2.1593E33y^2 + 2.3062E33y^4 + 6.9223E32y^5 + 4.0529E32)$

<div align="right">Continued on next page</div>

Table A.4 – continued from previous page

$Hp_j(x,y)$	Polynomial
Hp_{31}	$43.947x^2y^2 - 304.04x^2y^3 - 57.612x^2y^4 - 57.612x^4y^2 + 120.24x^2y^5 + 601.17x^4y^3 + 135.13x^2y - 456.06x^4y + 360.7x^6y - 7.3245x^4 + 11.522x^6 - 45.042y^3 - 7.3245y^4 + 152.02y^5 + 11.522y^6 - 120.24y^7$
Hp_{32}	$5.7255x(x^2 - 3.0y^2)(21.0(x^2 + y^2)^2 - 30.0x^2 - 30.0y^2 + 10.0) - 1.4314E - 31x(2.7587E32x^2y^2 + 2.0469E32x^2y - 3.22E32x^4y + 8.5319E31x^2 - 1.3793E32x^4 - 2.5596E32y^2 - 2.0469E32y^3 + 4.138E32y^4 + 3.22E32y^5)$
Hp_{33}	$327.23x^2y^3 - 28.472x^2y^4 + 28.472x^4y^2 - 397.2x^2y^5 - 220.67x^4y^3 - 163.62x^4y + 220.67x^6y + 6.318x^2 - 28.645x^4 + 28.472x^6 - 6.318y^2 + 28.645y^4 - 32.723y^5 - 28.472y^6 + 44.134y^7$
Hp_{34}	$1.5762E - 32x(8.0167E32y - 3.2391E33x^2y^2 + 7.2254E33x^2y^3 - 3.6347E33x^2y + 3.6127E33x^4y + 3.2391E32x^4 - 3.6347E33y^3 + 1.6195E33y^4 + 3.6127E33y^5) - 1.5762(x(8.0x^2y^2 - 1.0(x^2 + y^2)^2) + 4.0xy^2(x^2 - 1.0y^2))(28.0x^2 + 28.0y^2 - 24.0)$
Hp_{35}	$31.265(x^2 + y^2)^3 - 34.846(x^2 + y^2)^2 + 10.087x^2 + 10.087y^2 - 7.1619y(x^2 - 1.0y^2)(16.0x^2y^2 - 1.0(x^2 + y^2)^2) - 14.324x^2y(16.0x^2y^2 - 3.0(x^2 + y^2)^2) - 0.58506$
Hp_{36}	$232.97x^3y^4 - 139.78x^5y^2 - 46.594xy^6 + 6.6563x^7$
Hp_{37}	$52.954x^2y^5 - 88.257x^4y^3 + 302.83(x^2 + y^2)^2 - 517.87(x^2 + y^2)^3 + 285.79(x^2 + y^2)^4 + 17.651x^6y - 61.45x^2 - 61.45y^2 - 2.5216y^7 + 2.8163$
Hp_{38}	$105.43x^2y^3 + 561.26x^2y^4 - 561.26x^4y^2 - 141.02x^2y^5 - 78.344x^4y^3 - 665.01x^2y^6 + 665.01x^6y^2 - 52.717x^4y + 78.344x^6y - 43.828x^2 + 289.85x^4 - 561.26x^6 + 332.51x^8 + 43.828y^2 - 289.85y^4 - 10.543y^5 + 561.26y^6 + 15.669y^7 - 332.51y^8$
Hp_{39}	$1.3995E - 32x(2.2219E33y + 7.5337E33x^2y^2 + 1.7775E34x^2y^3 - 5.598E33x^2y^4 - 1.0076E34x^4y^2 - 9.4897E33x^2y + 8.8877E33x^4y - 7.5337E32x^4 + 1.1196E33x^6 - 9.4897E33y^3 - 3.7668E33y^4 + 8.8877E33y^5 + 5.598E33y^6) + 11.875xy(56.0(x^2 + y^2)^3 - 105.0(x^2 + y^2)^2 + 60.0x^2 + 60.0y^2 - 10.0)$
Hp_{40}	$1206.9x^2y^4 - 115.21x^2y^3 - 456.9x^2y^2 + 1206.9x^4y^2 + 51.879x^2y^5 + 259.39x^4y^3 - 731.68x^2y^6 - 1829.2x^4y^4 - 731.68x^6y^2 + 43.955x^2y - 172.81x^4y + 155.64x^6y + 76.151x^4 - 241.38x^6 + 182.92x^8 - 14.651y^3 + 76.151y^4 + 57.603y^5 - 241.38y^6 - 51.879y^7 + 182.92y^8$
Hp_{41}	$26.132xy(x^2 - 1.0y^2)(28.0(x^2 + y^2)^2 - 42.0x^2 - 42.0y^2 + 15.0) - 1.5398E - 32x(1.6846E34x^2y^4 - 7.4818E33x^2y^2 + 3.3692E33x^4y^2 + 5.6741E33x^2y - 8.5723E33x^4y - 9.5151E32x^2 + 3.7409E33x^4 - 3.3692E33x^6 + 2.8545E33y^2 - 5.6741E33y^3 - 1.1223E34y^4 + 8.5723E33y^5 + 1.0107E34y^6)$
Hp_{42}	$3.7829y + 205.0x^2y^3 + 658.08x^2y^4 - 658.08x^4y^2 - 233.59x^2y^5 - 233.59x^4y^3 - 815.1x^2y^6 + 815.1x^6y^2 - 38.632x^2y + 102.5x^4y - 77.865x^6y + 43.872x^6 - 58.222x^8 - 38.632y^3 + 102.5y^5 - 43.872y^6 - 77.865y^7 + 58.222y^8$
Hp_{43}	$(x(4.3872E7x^2y^3 - 1.025E7x^2y^2 + 1.168E7x^2y^4 + 1.168E7x^4y^2 - 4.0755E7x^2y^5 - 4.0755E7x^4y^3 - 1.3162E7x^4y + 1.7466E7x^6y + 1.9316E6x^2 - 5.125E6x^4 + 3.8932E6x^6 + 1.9316E6y^2 - 5.125E6y^4 - 1.3162E7y^5 + 3.8932E6y^6 + 1.7466E7y^7 - 189155.0))/50000$
Hp_{44}	$3.2151y + 180.77x^2y^3 + 49.357x^2y^4 - 49.357x^4y^2 - 209.65x^2y^5 - 209.65x^4y^3 - 299.42x^2y^6 + 565.18x^4y^4 - 152.72x^6y^2 - 33.452x^2y + 90.383x^4y - 69.883x^6y + 3.2904x^6 + 2.8346x^8 - 33.452y^3 + 90.383y^5 - 3.2904y^6 - 69.883y^7 + 13.313y^8$
Hp_{45}	$-(x(3.2904E6x^2y^3 - 9.0383E6x^2y^2 + 1.0482E7x^2y^4 + 1.0482E7x^4y^2 + 1.894E7x^2y^5 - 2.6275E7x^4y^3 - 987144.0x^4y + 4.8014E6x^6y + 1.6726E6x^2 - 4.5192E6x^4 + 3.4942E6x^6 + 1.6726E6y^2 - 4.5192E6y^4 - 987144.0y^5 + 3.4942E6y^6 - 1.6578E6y^7 - 160766.0))/50000$

Table A.5: Table of octagon polynomials $O_j(x,y)$ in Cartesian coordinates.

$O_j(x,y)$	Polynomial
O_1	1
O_2	$(221^{1/2}x(4-2^{1/2})^{1/2})/7$
O_3	$(221^{1/2}y(4-2^{1/2})^{1/2})/7$
O_4	$-(9870^{1/2}(19-42^{1/2})^{1/2}(43^{1/2}+6^{1/2}-123^{1/2}x^2-123^{1/2}y^2))/1974$
O_5	$(6115^{1/2}xy(8-32^{1/2})^{1/2})/23$
O_6	$(3115^{1/2}(8-32^{1/2})^{1/2}(x^2-y^2))/23$
O_7	$-(1763286^{1/2}y(304-652^{1/2})^{1/2}(522^{1/2}-1052^{1/2}x^2-1052^{1/2}y^2+16))/293881$
O_8	$-(1763286^{1/2}x(304-652^{1/2})^{1/2}(522^{1/2}-1052^{1/2}x^2-1052^{1/2}y^2+16))/293881$
O_9	$(22765^{1/2}y(16-72^{1/2})^{1/2}(3x^2-y^2))/79$
O_{10}	$(22765^{1/2}x(16-72^{1/2})^{1/2}(x^2-3y^2))/79$
O_{11}	$-(212^{(1/4)}33814955^{1/2}(493812^{1/2}-20662)^{1/2}(((138515^{1/2})/6909-(17830^{1/2})/2303)((23^{1/2})/3+$
O_{12}	$15.149x^4-10.301x^2+10.301y^2-15.149y^4$
O_{13}	$(xy(151499.0x^2+151499.0y^2-103011.0))/5000$
O_{14}	$3.5722(x^2+y^2)^2-28.578x^2y^2$
O_{15}	$16.881xy(x^2-1.0y^2)$
O_{16}	$(x(847511.0x^2y^2-464433.0x^2+423766.0x^4-464433.0y^2+423766.0y^4+106300.0))/10000$
O_{17}	$(y(847511.0x^2y^2-464433.0x^2+423766.0x^4-464433.0y^2+423766.0y^4+106300.0))/10000$
O_{18}	$1.5671x(x^2-3.0y^2)+4.2991x(x^2-3.0y^2)(5.0x^2+5.0y^2-4.0)$
O_{19}	$1.5671y(3.0x^2-1.0y^2)+4.2991y(3.0x^2-1.0y^2)(5.0x^2+5.0y^2-4.0)$
O_{20}	$(x(663544.0x^2-9.2405E6x^2y^2+42727.0x^4-1.9906E6y^2+9.0268E6y^4))/250000$
O_{21}	$(y(9.0268E6x^4-1.9906E6x^2-9.2405E6x^2y^2+663544.0y^2+42727.0y^4))/250000$
O_{22}	$15.746x^2y^2-98.482(x^2+y^2)^2+65.655(x^2+y^2)^3+33.421x^2+7.873x^4+33.421y^2+7.873y^4-2.5739$
O_{23}	$(xy(561455.0x^2y^2-343555.0x^2+280722.0x^4-343555.0y^2+280722.0y^4+94815.0))/2000$
O_{24}	$70.181x^4y^2-70.181x^2y^4+23.704x^2-85.887x^4+70.181x^6-23.704y^2+85.887y^4-70.181y^6$
O_{25}	$-0.0008xy(123188.0x^2-169088.0x^4-123188.0y^2+169088.0y^4)$
O_{26}	$123.05x^2y^2-131.25x^2y^4-131.25x^4y^2-20.509x^4+26.25x^6-20.509y^4+26.25y^6$
O_{27}	$-0.00002xy(2.0448E6x^2y^2+1.6748E6x^2-3.2177E6x^4+1.6748E6y^2-3.2177E6y^4-377422.0)$
O_{28}	$95.778x^2y^4-95.778x^4y^2-3.7742x^2+16.748x^4-10.977x^6+3.7742y^2-16.748y^4+10.977y^6$
O_{29}	$(y(5.2607E6x^2y^4-5.5706E6x^2y^2+5.2607E6x^4y^2+1.2929E6x^2-2.7853E6x^4+1.7536E6x^6+1.2929E6y^2-$
O_{30}	$(x(5.2607E6x^2y^4-5.5706E6x^2y^2+5.2607E6x^4y^2+1.2929E6x^2-2.7853E6x^4+1.7536E6x^6+1.2929E6y^2-$
O_{31}	$(y(546666.0x^2y^4-1.4802E6x^2y^2+2.7333E6x^4y^2+657244.0x^2-2.1222E6x^4+1.64E6x^6-219088.0y^2+7$
O_{32}	$-0.0002x(2.7333E6x^2y^4-1.4802E6x^2y^2+546666.0x^4y^2-219088.0x^2+720488.0x^4-546666.0x^6+657244.$
O_{33}	$(y(2.3592E7x^2y^2-3.3078E7x^2y^4-3.9973E6x^4y^2+2.8471E6x^2-2.6447E7x^4+2.988E7x^6-949044.0y^2+$
O_{34}	$(x(2.3592E7x^2y^2-3.9973E6x^2y^4-3.3078E7x^4y^2-949044.0x^2+571133.0x^4+799466.0x^6+2.8471E6y^2-$

Continued on next page

Table A.5 – continued from previous page

$O_j(x,y)$	Polynomial
O_{35}	$-0.00001y(1.1525E7x^2y^2 - 2.5616E7x^2y^4 + 8.4121E6x^4y^2 - 2.2163E6x^2 + 5.7626E6x^4 - 8.5387E6x^6 - 2.2163$
O_{36}	$0.00001x(1.1525E7x^2y^2 + 8.4121E6x^2y^4 - 2.5616E7x^4y^2 - 2.2163E6x^2 + 5.7626E6x^4 - 3.6775E6x^6 - 2.2163E$
O_{37}	$17.696x^2y^2 + 271.92(x^2+y^2)^2 - 466.69(x^2+y^2)^3 + 249.73(x^2+y^2)^4 - 58.48x^2 + 8.8478x^4 - 58.48y^2$
O_{38}	$515.3x^2y^4 - 515.3x^4y^2 - 612.42x^2y^6 + 612.42x^6y^2 - 43.777x^2 + 282.28x^4 - 533.12x^6 + 306.21x^8 + 43$
O_{39}	$1.2888E - 31xy(1.135E33x^2y^2 - 7.1072E32x^2 + 7.0576E32x^4 - 7.1072E32y^2 + 7.0576E32y^4 + 1.692E32) + 10.936x$
O_{40}	$998.18x^2y^4 - 405.99x^2y^2 + 998.18x^4y^2 - 561.64x^2y^6 - 1404.1x^4y^4 - 561.64x^6y^2 + 67.665x^4 - 199.6$
O_{41}	$28.235xy(x^2 - 1.0y^2)(28.0(x^2+y^2)^2 - 42.0x^2 - 42.0y^2 + 15.0) - 4.9913E - 31xy(1.9188E32x^2 - 2.8676E32)$
O_{42}	$758.2x^2y^4 - 758.2x^4y^2 - 926.92x^2y^6 - 7.2442E - 38x^4y^4 + 926.92x^6y^2 - 8.5751x^2 + 66.302x^4 - 105.87$
O_{43}	$(xy(2.2883E6x^2y^2 - 1.4758E6x^2y^4 - 1.4758E6x^4y^2 + 1.326E6x^2 - 5.3791E6x^4 + 5.0859E6x^6 + 1.326E6y^2 -$
O_{44}	$506.19x^4y^4 - 202.48x^2y^6 - 202.48x^6y^2 - 74.922(x^2+y^2)^2 + 149.27(x^2+y^2)^3 - 94.176(x^2+y^2)^4 +$
O_{45}	$370.25x^5y^3 - 370.25x^3y^5 + 52.893xy^7 - 52.893x^7y$

Table A.6: Table of nonagon polynomials $N_j(x,y)$ in Cartesian coordinates.

$N_j(x,y)$	Polynomial
N_1	1
N_2	$2.0829x$
N_3	$2.0829y$
N_4	$x^2(3.7464 + 2.5375E - 23i) + y^2(3.7464 + 2.5375E - 23i) - (1.7271 + 1.1817E - 12i)$
N_5	$xy(5.3095 - 1.3788E - 13i)$
N_6	$x^2(2.6548 - 1.2066E - 13i) - y^2(2.6548 - 1.2066E - 13i)$
N_7	$y(0.48598 - 4.1331E - 12i) + y(3.0x^2 + 3.0y^2 - 2.0)(3.1695 - 1.9206E - 24i)$
N_8	$x(0.48598 + 1.1177E - 11i) + x(3.0x^2 + 3.0y^2 - 2.0)(3.1695 - 7.7846E - 22i)$
N_9	$y(2.768E - 13 - 1.2556E - 12i) + y(3.0x^2 - 1.0y^2)(3.1879 - 1.0423E - 23i)$
N_{10}	$x(x^2 - 3.0y^2)(3.1879 - 6.107E - 26i) - x(6.92E - 12 - 2.9345E - 14i)$
N_{11}	$15.484(x^2+y^2)^2 - 14.339x^2 - 14.339y^2 + 2.2163$
N_{12}	$14.653x^4 - 10.162x^2 + 10.162y^2 - 14.653y^4$
N_{13}	$(xy(293066.0x^2 + 293066.0y^2 - 203244.0))/10000$
N_{14}	$3.7037(x^2+y^2)^2 - 29.63x^2y^2$
N_{15}	$14.815xy(x^2 - 1.0y^2)$
N_{16}	$(3x(273455.0x^2y^2 - 152399.0x^2 + 136722.0x^4 - 152399.0y^2 + 136722.0y^4 + 35439.0))/10000$
N_{17}	$(3y(273455.0x^2y^2 - 152399.0x^2 + 136722.0x^4 - 152399.0y^2 + 136722.0y^4 + 35439.0))/10000$
N_{18}	$1.2242x(x^2 - 3.0y^2) + 4.1388x(x^2 - 3.0y^2)(5.0x^2 + 5.0y^2 - 4.0)$
N_{19}	$3.6725x^2y - 1.2242y^3 + 4.1388y(3.0x^2 - 1.0y^2)(5.0x^2 + 5.0y^2 - 4.0)$
N_{20}	$(x(425600.0x^4 - 212299.0x^2y - 4.256E6x^2y^2 + 212299.0y^3 + 2.128E6y^4))/100000$

Continued on next page

$N_j(x, y)$	Polynomial
N_{21}	$3.1844x^2y^2 - 42.56x^2y^3 + 21.28x^4y - 0.53074x^4 - 0.53074y^4 + 4.2559y^5$
N_{22}	$63.723(x^2 + y^2)^3 - 89.187(x^2 + y^2)^2 + 33.335x^2 + 33.335y^2 - 2.5996$
N_{23}	$(xy(1.3587E6x^2y^2 - 843888.0x^2 + 679344.0x^4 - 843888.0y^2 + 679344.0y^4 + 236211.0))/5000$
N_{24}	$67.934x^4y^2 - 67.934x^2y^4 + 23.621x^2 - 84.389x^4 + 67.934x^6 - 23.621y^2 + 84.389y^4 - 67.934y^6$
N_{25}	$-1.0E - 6x(8.6215E7x^2y - 7.317E6x^2y^2 - 1.1202E8x^4y + 731700.0x^4 - 8.6215E7y^3 + 3.6585E6y^4 + 1.1202E8y^5)$
N_{26}	$129.32x^2y^2 + 7.317x^2y^3 - 140.03x^2y^4 - 140.03x^4y^2 - 3.6585x^4y - 21.554x^4 + 28.006x^6 - 21.554y^4 - 0.7317y^5 + 28.006y^6$
N_{27}	$(x(718288.0x^2y^2 - 9.6751E6x^2y^3 + 2.9025E6x^4y + 221377.0x^2 - 359144.0x^4 - 664122.0y^2 + 1.0774E6y^4 + 2.9025E6y^5))/100000$
N_{28}	$72.563x^2y^4 - 7.1828x^2y^3 - 72.563x^4y^2 + 6.6412x^2y - 10.774x^4y + 4.8376x^6 - 2.2137y^3 + 3.5914y^5 - 4.8376y^6$
N_{29}	$4.879y(35.0(x^2 + y^2)^3 - 60.0(x^2 + y^2)^2 + 30.0x^2 + 30.0y^2 - 4.0) + 2.4395E - 32y(1.5053E33x^2y^2 - 7.218E32x^2 + 7.5267E32x^4 - 7.218E32y^2 + 7.5267E32y^4 + 1.3856E32)$
N_{30}	$4.879x(35.0(x^2 + y^2)^3 - 60.0(x^2 + y^2)^2 + 30.0x^2 + 30.0y^2 - 4.0) + 1.2197E - 32x(3.0107E33x^2y^2 - 1.4436E33x^2 + 1.5053E33x^4 - 1.4436E33y^2 + 1.5053E33y^4 + 2.7712E32)$
N_{31}	$13.916x^4y^2 - 13.916x^2y^4 - 280.27x^2y^3 + 105.48x^2y^5 + 527.42x^4y^3 + 130.51x^2y - 420.4x^4y + 316.45x^6y - 0.92772x^6 - 43.504y^3 + 140.13y^5 + 0.92772y^6 - 105.48y^7$
N_{32}	$5.023x(x^2 - 3.0y^2)(21.0(x^2 + y^2)^2 - 30.0x^2 - 30.0y^2 + 10.0) - 1.2558E - 32x(1.6816E33x^2y^2 - 1.4775E33x^2y^3 + 4.4326E32x^4y + 5.3562E32x^2 - 8.4079E32x^4 - 1.6069E33y^2 + 2.5224E33y^4 + 4.4326E32y^5)$
N_{33}	$288.93x^2y^3 - 23.522x^2y^2 + 29.567x^2y^4 + 29.567x^4y^2 - 329.51x^2y^5 - 183.06x^4y^3 - 144.47x^4y + 183.06x^6y + 3.9203x^4 - 5.9134x^6 + 3.9203y^4 - 28.893y^5 - 5.9134y^6 + 36.612y^7$
N_{34}	$1.3076E - 32x(1.1993E33x^2y - 1.9031E33x^2y^2 - 1.809E33x^4y + 1.9031E32x^4 - 1.1993E33y^3 + 9.5155E32y^4 + 1.809E33y^5) - 1.3076(x(8.0x^2y^2 - 1.0(x^2 + y^2)^2) + 4.0xy^2(x^2 - 1.0y^2))(28.0x^2 + 28.0y^2 - 24.0)$
N_{35}	$13.512x^2y^4 - 13.512x^4y^2 + 114.57x^2y^5 - 190.95x^4y^3 + 38.189x^6y - 3.2901x^2 + 14.251x^4 - 13.512x^6 + 3.2901y^2 - 14.251y^4 + 13.512y^6 - 5.4556y^7$
N_{36}	$-0.00001x(658011.0y + 5.405E6x^2y^3 - 1.9094E7x^2y^4 + 1.1457E7x^4y^2 - 2.8501E6x^2y + 2.7025E6x^4y - 545566.0x^6 - 2.8501E6y^3 + 2.7025E6y^5 + 3.8189E6y^6)$
N_{37}	$294.26(x^2 + y^2)^2 - 485.0(x^2 + y^2)^3 + 257.26(x^2 + y^2)^4 - 61.789x^2 - 61.789y^2 + 2.9228$
N_{38}	$524.02x^2y^4 - 524.02x^4y^2 - 22.919x^2y^5 + 38.198x^4y^3 - 596.84x^2y^6 - 1.1641E - 10x^4y^4 + 596.84x^6y^2 - 7.6396x^6y - 43.962x^2 + 280.84x^4 - 524.02x^6 + 298.42x^8 + 43.962y^2 - 280.84y^4 + 524.02y^6 + 1.0914y^7 - 298.42y^8$
N_{39}	$2.5121E - 33x(7.4261E33y + 5.6561E34x^2y^3 - 1.5206E34x^2y^4 + 9.1234E33x^4y^2 - 3.0971E34x^2y + 2.8281E34x^4y - 4.3445E32x^6 - 3.0971E34y^3 + 2.8281E34y^5 + 3.0411E33y^6) + 10.658xy(56.0(x^2 + y^2)^3 - 105.0(x^2 + y^2)^2 + 60.0x^2 + 60.0y^2 - 10.0)$
N_{40}	$1081.5x^2y^4 - 61.185x^2y^3 - 430.58x^2y^2 + 1081.5x^4y^2 + 78.818x^2y^5 + 43.788x^4y^3 - 621.89x^2y^6 - 1554.7x^4y^4 - 621.89x^6y^2 + 30.592x^4y - 43.788x^6y + 71.763x^4 - 216.3x^6 + 155.47x^8 + 71.763y^4 + 6.1185y^5 - 216.3y^6 - 8.7575y^7 + 155.47y^8$
N_{41}	$1.3087E - 32x(3.3458E33x^2y^4 - 4.6751E33x^2y^2 + 6.0224E33x^4y^2 - 3.5224E33x^2y + 5.1657E33x^4y + 4.6751E32x^4 - 6.6915E32x^6 + 3.5224E33y^3 + 2.3375E33y^4 - 5.1657E33y^5 - 3.3458E33y^6) + 22.21xy(x^2 - 1.0y^2)(28.0(x^2 + y^2)^2 - 42.0x^2 - 42.0y^2 + 15.0)$
	Continued on next page

Table A.6 – continued from previous page

$N_j(x, y)$	Polynomial
N_{42}	$562.25x^2y^4 - 60.131x^2y^3 - 562.25x^4y^2 + 25.953x^2y^5 + 129.76x^4y^3 - 653.37x^2y^6 + 653.37x^6y^2 + 23.903x^2y - 90.197x^4y + 77.858x^6y + 37.483x^6 - 46.669x^8 - 7.9676y^3 + 30.066y^5 - 37.483y^6 - 25.953y^7 + 46.669y^8$
N_{43}	$-0.00002x(3.0066E6x^2y^2 - 3.7483E7x^2y^3 - 6.4882E6x^2y^4 - 1.2976E6x^4y^2 + 3.2669E7x^2y^5 + 3.2669E7x^4y^3 + 1.1245E7x^4y - 1.4001E7x^6y + 398388.0x^2 - 1.5033E6x^4 + 1.2976E6x^6 - 1.1951E6y^2 + 4.5098E6y^4 + 1.1245E7y^5 - 3.8929E6y^6 - 1.4001E7y^7)$
N_{44}	$2.0694y + 102.31x^2y^3 - 111.12x^2y^5 - 111.12x^4y^3 - 171.14x^2y^6 + 427.85x^4y^4 - 171.14x^6y^2 - 20.199x^2y + 51.154x^4y - 37.039x^6y + 6.1121x^8 - 20.199y^3 + 51.154y^5 - 37.039y^7 + 6.1121y^8$
N_{45}	$1.28E - 9x(8.6809E10x^2y^4 - 7.9928E10x^2y^2 + 8.6809E10x^4y^2 - 2.674E11x^2y^5 + 2.674E11x^4y^3 - 3.8201E10x^6y + 1.5781E10x^2 - 3.9964E10x^4 + 2.8936E10^6 + 1.5781E10y^2 - 3.9964E10y^4 + 2.8936E10y^6 + 3.8201E10y^7 - 1.6167E9)$

Bibliography

[1] L. W. Piotrowski, T. Batsch, H. Czyrkowski, M. Cwiok, R. Dabrowski, G. Kasprowicz, A. Majcher, A. Majczyna, K. Malek, L. Mankiewicz, K. Nawrocki, R. Opiela, M. Siudek, M. Sokolowski, R. Wawrzaszek, G. Wrochna, M. Zaremba, and A. F. Żarnecki, "PSF modelling for very wide-field CCD astronomy," Astronomy & Astrophysics **551**, A119 (2013).

[2] G. Zheng, X. Ou, R. Horstmeyer, and C. Yang, "Characterization of spatially varying aberrations for wide field-of-view microscopy," Optics Express **21**, 15131 (2013).

[3] G. Zheng, R. Horstmeyer, and C. Yang, "Wide-field, high-resolution Fourier ptychographic microscopy," Nature Photonics **7**, 739–745 (2013).

[4] R. G. Lane and M. Tallon, "Wave-front reconstruction using a Shack–Hartmann sensor," Applied Optics **31**, 6902 (1992).

[5] T. Ito, Y. Fujii, N. Ohta, S. Saitoh, T. Matsuura, and T. Yamamoto, "Measurement of Space Variant PSF for Restoring Degraded Images by Security Cameras," in "SICE-ICASE, 2006. International Joint Conference," (2006), pp. 2542–2545.

[6] M. Řeřábek and P. Páta, "Modeling of the widefield space variant security systems," in "Security Technology, 2008. ICCST 2008. 42nd Annual IEEE International Carnahan Conference On," (2008), pp. 121–125.

[7] T. Ito, H. Hoshino, Y. Fujii, and N. Ohta, "Reconstruction of face image from security camera based on a measurement of space variant PSF," in "ICCAS-SICE, 2009," (2009), pp. 2301–2304.

[8] G. Pojmanski, "The All Sky Automated Survey," (1997).

[9] A. Burd, M. Cwiok, H. Czyrkowski, R. Dabrowski, W. Dominik, M. Grajda, M. Husejko, M. Jegier, A. Kalicki, G. Kasprowicz, K. Kierzkowski, K. Krupska, K. Kwiecinska, L. Mankiewicz, K. Nawrocki, B. Pilecki, L. Piotrowski, K. Pozniak, R. Romaniuk, R. Salanski, M. Sokolowski,

D. Szczygiel, G. Wrochna, and W. Zabolotny, "Pi of the Sky – all-sky, real-time search for fast optical transients," New Astronomy **10**, 409–416 (2005).

[10] T. E. Pickering, "The MMT all-sky camera," in "Ground-Based and Airborne Telescopes," , vol. 6267 L. M. Stepp, ed. (Proc. SPIE, 2006), vol. 6267, pp. 62671A–62671A–7.

[11] E. Anisimova, P. Janout, M. Blažek, M. Bednář, K. Fliegel, P. Páta, S. Vítek, and J. Švihlík, "Analysis of images obtained from space-variant astronomical imaging systems," Proc. SPIE **8856** (2013).

[12] M. Řeřábek, "Advanced Processing of Images Obtained from Wide-field Astronomical Optical Systems," Acta Polytechnica **51**, 90–96 (2011).

[13] M. Řeřábek, "Space Variant PSF Deconvolution of Wide-Field Astronomical Images," Acta Polytechnica **48**, 79–84 (2008).

[14] V. N. Mahajan, "Zernike Circle Polynomials and Optical Aberrations of Systems with Circular Pupils," Applied Optics **33**, 8121–8124 (1994).

[15] M. Born and E. Wolf, *Principles of Optics* (Cambridge University Press, 1999), 7th ed.

[16] F. von Zernike, "Beugungstheorie des schneidenver-fahrens und seiner verbesserten form, der phasenkontrastmethode," Physica **1**, 689–704 (1934).

[17] R. J. Noll, "Zernike polynomials and atmospheric turbulence," J. Opt. Soc. Am. **66**, 207–211 (1976).

[18] H. H. Hopkins, "Image formation by a general optical system 1: General theory," Applied Optics **24**, 2491 (1985).

[19] J. Sasián, "Theory of sixth-order wave aberrations," Applied Optics **49**, D69–D95 (2010).

[20] J. Ye, Z. Gao, S. Wang, X. Liu, Z. Yang, and C. Zhang, "Bi-Zernike polynomials for wavefront aberration function in rotationally symmetric optical systems," (OSA, 2013), p. JM3A.6.

[21] R. W. Gray, C. Dunn, K. P. Thompson, and J. P. Rolland, "An analytic expression for the field dependence of Zernike polynomials in rotationally symmetric optical systems," Optics Express **20**, 16436 (2012).

[22] S. Weddell and R. Webb, "Reservoir Computing for Prediction of the Spatially-Variant Point Spread Function," Selected Topics in Signal Processing, IEEE Journal of **2**, 624–634 (2008).

[23] S. Weddell and R. Webb, "The restoration of extended astronomical images using the spatially-variant point spread function," in "Image and Vision Computing New Zealand, 2008. IVCNZ 2008. 23rd International Conference," (2008), pp. 1–6.

[24] S. Yokozeki and K. Ohnishi, "Spherical Aberration Measurement with Shearing Interferometer Using Fourier Imaging and Moiré Method," Applied Optics **14**, 623 (1975).

[25] J. Sung, M. Pitchumani, and E. G. Johnson, "Aberration measurement of photolithographic lenses by use of hybrid diffractive photomasks," Applied Optics **42**, 1987 (2003).

[26] J. Chung, J. Kim, X. Ou, R. Horstmeyer, and C. Yang, "Wide field-of-view fluorescence image deconvolution with aberration-estimation from Fourier ptychography," Biomedical Optics Express **7**, 352 (2016).

[27] S. Y. Hasan and A. H. Al-Hamdani, "Zernike polynomiales for optical systems with rectangular and square apertures of area equal to," Indian Journal of Pure & Applied Physics (IJPAP) **51**, 837–843 (2016).

[28] K. P. Thompson, K. Fuerschbach, and J. P. Rolland, "An analytic expression for the field dependence of FRINGE Zernike polynomial coefficients in optical systems that are rotationally nonsymmetric," (2010), p. 784906.

[29] R. Maksimenka, P. Nuernberger, K. F. Lee, A. Bonvalet, J. Milkiewicz, C. Barta, M. Klima, T. Oksenhendler, P. Tournois, D. Kaplan, and M. Joffre, "Direct mid-infrared femtosecond pulse shaping with a calomel acousto-optic programmable dispersive filter," Optics Letters **35**, 3565 (2010).

[30] P. Pata, M. Klima, J. Bednar, P. Janout, C. Barta, R. Hasal, L. Maresi, and S. Grabarnik, "OFT sectorization approach to analysis of optical scattering in mercurous chloride single crystals," Optics Express **23**, 21509–21526 (2015).

[31] J. A. Díaz and V. N. Mahajan, "Imaging by a system with a hexagonal pupil," Applied Optics **52**, 5112–5122 (2013).

[32] C. Ferreira, J. L. López, R. Navarro, and E. P. Sinusía, "Zernike-like systems in polygons and polygonal facets," Applied Optics **54**, 6575–6583 (2015).

[33] V. N. Mahajan and G.-m. Dai, "Orthonormal polynomials in wavefront analysis: Analytical solution," JOSA A **24**, 2994–3016 (2007).

[34] V. N. Mahajan, "Orthonormal aberration polynomials for anamorphic optical imaging systems with rectangular pupils," Applied Optics **49**, 6924–6929 (2010).

[35] J. A. Díaz and V. N. Mahajan, "Study of Zernike polynomials of an elliptical aperture obscured with an elliptical obscuration: Comment," Applied Optics **52**, 5962–5964 (2013).

[36] Y. L. Qi and Z. Y. Cheng, "Linear Space-Variant Model and Restoration Algorithm of Imaging System," Applied Mechanics and Materials **608-609**, 559–567 (2014).

[37] F. Heide, M. Rouf, M. B. Hullin, B. Labitzke, W. Heidrich, and A. Kolb, "High-quality Computational Imaging Through Simple Lenses," ACM Trans. Graph. **32**, 149:1–149:14 (2013).

[38] R. Shack and B. Platt, "Production and Use of a Lenticular Hartmann Screen," (Optical Society of America, 1971).

[39] P. Janout, P. Páta, J. Bednář, E. Anisimova, M. Blažek, and P. Skala, "Stellar objects identification using wide-field camera," (2015), p. 94501I.

[40] B. Paczyński, "Astronomy with Small Telescopes," Publications of the Astronomical Society of the Pacific **118**, 1621–1625 (2006).

[41] S. Vítek, "Modeling of Astronomical Images," Baltic Astronomy **18**, 387–391 (2009).

[42] P. Janout, P. Páta, P. Skala, and J. Bednář, "PSF Estimation of Space-Variant Ultra-Wide Field of View Imaging Systems," Applied Sciences **7**, 151 (2017).

[43] P. Janout, M. Blažek, and P. Páta, "New generation of meteorology cameras," (International Society for Optics and Photonics, 2017), vol. 10603, p. 106031C.

[44] J. W. Goodman, *Introduction to Fourier Optics* (Roberts & Co, Englewood, Colo, 2005), 3rd ed. OCLC: ocm56632414.

[45] P. Janout, P. Skala, J. Bednář, and P. Páta, "Měření vlastností extrémně širokoúhlých zobrazovacích systémů," Slaboproudý obzor **71 (2015)**, 11–13 (2015).

[46] C. Laroche and M. Prescott, "Apparatus and method for adaptively interpolating a full color image utilizing chrominance gradients," Americká klasifikace 348/273, 348/E09.01, 348/272; Mezinárodní klasifikace H04N9/04, G06T3/40; Klasifikace CPC H04N2209/046, H04N9/045, G06T3/4015, G06T3/4007; Evropská klasifikace G06T3/40B, H04N9/04B, G06T3/40C.

[47] P. Koten, K. Fliegel, S. Vítek, and P. Páta, "Automatic Video System for Continues Monitoring of the Meteor Activity," Earth, Moon, and Planets **108**, 69–76 (2011).

[48] S. Vítek, P. Koten, P. Páta, and K. Fliegel, "Double-Station Automatic Video Observation of the Meteors," Advances in Astronomy pp. 1–4 (2010).

[49] V. Stanislav and N. Maria, "Real-Time Detection of Sporadic Meteors in the Intensified TV Imaging Systems," Sensors **18**, 77 (2017).

[50] I. Chang, "Collinear beam acousto-optic tunable filters," Electronics Letters **28**, 1255 (1992).

[51] V. B. Voloshinov and N. V. Polikarpova, "Acousto-optic investigation of propagation and reflection of acoustic waves in paratellurite crystal," Applied Optics **48**, C55 (2009).

[52] E. Anisimova, P. Páta, and M. Blažek, "Stellar Object Detection Using the Wavelet Transform," Acta Polytechnica **51**, 9–12 (2011).

[53] M. Blažek and P. Páta, "Colour transformations and K-means segmentation for automatic cloud detection," Meteorologische Zeitschrift **24**, 503–509 (2015).

[54] E. S. Wirström, M. S. Lerner, P. Källström, A. Levinsson, A. Olivefors, and E. Tegehall, "HCN observations of comets C/2013 R1 (Lovejoy) and C/2014 Q2 (Lovejoy)," Astronomy & Astrophysics **588**, A72 (2016).

[55] P. Janout, P. Páta, P. Skala, K. Fliegel, S. Vítek, and J. Bednář, "Application of field dependent polynomial model," (2016), p. 99710F.

[56] K. Fliegel, P. Janout, J. Bednář, L. Krasula, S. Vítek, J. Švihlík, and P. Páta, "Performance evaluation of image deconvolution techniques in space-variant astronomical imaging systems with nonlinearities," (2015), p. 959927.

[57] E. Anisimova, J. Bednář, M. Blažek, P. Janout, K. Fliegel, P. Páta, S. Vítek, and J. Švihlík, "Estimation and measurement of space-variant features of imaging systems and influence of this knowledge on accuracy of astronomical measurement," (2014), vol. 9217, pp. 92171E–92171E–13.

[58] S. Vítek, K. Fliegel, P. Páta, and P. Koten, "MAIA: Technical Development of a Novel System for Video Observations of Meteors," Acta Polytechnica **51**, 109 (2011).

[59] S. Vítek, M. Nasyrova, and V. Stehlikova, "Radiometric calibration of wide-field camera system with an application in astronomy," (SPIE, 2017), p. 112.

[60] S. Vítek, "Light-pollution measurement with the Wide-field all-sky image analyzing monitoring system," Contributions of the Astronomical Observatory Skalnate Pleso **47**, 215–219 (2017).

[61] J. M. Trigo-Rodriguez, J. M. Madiedo, P. S. Gural, A. J. Castro-Tirado, J. Llorca, J. Fabregat, S. Vítek, and P. Pujols, "Determination of Meteoroid Orbits and Spatial Fluxes by Using High-Resolution All-Sky CCD Cameras," Earth, Moon, and Planets **102**, 231–240 (2008).

[62] J. Romero, R. Luzón-González, J. L. Nieves, and J. Hernández-Andrés, "Color changes in objects in natural scenes as a function of observation distance and weather conditions," Applied Optics **50**, F112 (2011).

[63] J. Hernández-Andrés, J. Romero, J. L. Nieves, and R. L. Lee, "Color and spectral analysis of daylight in southern Europe," JOSA A **18**, 1325–1335 (2001).

[64] T. Smith and J. Guild, "The C.I.E. colorimetric standards and their use," Transactions of the Optical Society **33**, 73–134 (1931).

[65] J. Schanda and International Commission on Illumination, eds., *Colorimetry: Understanding the CIE System* (CIE/Commission internationale de l'eclairage ; Wiley-Interscience, [Vienna, Austria] : Hoboken, N.J, 2007). OCLC: ocm77256743.

[66] C. A. Poynton, *A Technical Introduction to Digital Video* (J. Wiley, New York, 1996).

[67] S. Lloyd, "Least squares quantization in PCM," IEEE Transactions on Information Theory **28**, 129–137 (1982).

[68] P. Janout and P. Páta, "Orthonormalization, analysis and numerical approximation for general N-gon apertures," Optical Engineering **2018** (2018). Under review.

[69] P. Janout and P. Páta, "Orthonormal N-gon polynomials," http://william.multimediatech.cz/orthonormal-n-gon-polynomials/ (2018). Mat files.

[70] E. Abbe, "Beiträge zur Theorie des Mikroskops und der mikroskopischen Wahrnehmung," .

[71] H. Köhler, "On Abbe's Theory of Image Formation in the Microscope," Optica Acta: International Journal of Optics **28**, 1691–1701 (1981).

[72] H. H. Hopkins, "On the Diffraction Theory of Optical Images," Proceedings of the Royal Society A: Mathematical, Physical and Engineering Sciences **217**, 408–432 (1953).

[73] H. H. Hopkins, "The frequency response of a defocused optical system," Proc. R. Soc. Lond. A **231**, 91–103 (1955).

[74] L. Seidel, "Zur Dioptrik. Ueber die Entwicklung der Glieder 3ter Ordnung, welche den Weg eines ausserhalb der Ebene der Axe gelegenen Lichtstrahles durch ein System brechender Medien bestimmen, von Herrn Dr.L. Seidel," Astronomische Nachrichten **43**, 289–304 (1856).

[75] R. Navarro, J. Arines, and R. Rivera, "Direct and inverse discrete Zernike transform," Opt. Express **17**, 24269–24281 (2009).

[76] J. Sasian, *Introduction to Aberrations in Optical Imaging Systems* (Cambridge University Press, Cambridge, 2012).

[77] D. Malacara, ed., *Optical Shop Testing*, Wiley series in pure and applied optics (Wiley-Interscience, Hoboken, N.J, 2007), 3rd ed. OCLC: ocm74916130.

[78] V. N. Mahajan and J. A. Díaz, "Imaging characteristics of Zernike and annular polynomial aberrations," Applied Optics **52**, 2062 (2013).

[79] R. Upton and B. Ellerbroek, "Gram–Schmidt orthogonalization of the Zernike polynomials on apertures of arbitrary shape," Optics Letters **29**, 2840–2842 (2004).

[80] G. A. Korn and T. M. Korn, *Mathematical Handbook for Scientists and Engineers*, vol. 1968.

[81] V. N. Mahajan and G.-m. Dai, "Orthonormal polynomials for hexagonal pupils," Optics Letters **31**, 2462–2464 (2006).

[82] V. N. Mahajan, "Orthonormal polynomials in wavefront analysis: Analytical solution: Errata," JOSA A **29**, 1673–1674 (2012).

[83] G.-m. Dai and V. N. Mahajan, "Nonrecursive determination of orthonormal polynomials with matrix formulation," Optics Letters **32**, 74–76 (2007).

[84] R. Gilmozzi and J. Spyromilio, "The European Extremely Large Telescope (E-ELT)," The Messenger **127** (2007).

[85] R. Maksimenka and P. Tournois, "Mid-infrared high-frequency high-resolution reflective acousto-optic filters in mercury halides," Optics Communications **285**, 715–719 (2012).

[86] V. N. Mahajan, *Optical Imaging and Aberrations* (SPIE Optical Engineering Press, Bellingham, Wash, 1998).

[87] W. Swantner and W. W. Chow, "Gram–Schmidt orthonormalization of Zernike polynomials for general aperture shapes," Applied Optics **33**, 1832–1837 (1994).

[88] J. A. Nelder and R. Mead, "A Simplex Method for Function Minimization," The Computer Journal **7**, 308–313 (1965).

[89] M. J. D. Powell, "On search directions for minimization algorithms," Mathematical Programming **4**, 193–201 (1973).

[90] J. F. Bonnans, ed., *Numerical Optimization: Theoretical and Practical Aspects*, Universitext (Springer, Berlin ; New York, 2006), 2nd ed.

[91] W. H. Press, ed., *Numerical Recipes: The Art of Scientific Computing* (Cambridge University Press, Cambridge, UK ; New York, 2007), 3rd ed. OCLC: ocn123285342.

[92] I. Trujillo, A. Aguerri, J. Cepa, and C. M. Gutierrez, "The effects of seeing on Sersic profiles. II. The Moffat PSF," Monthly Notices of the Royal Astronomical Society **328**, 977–985 (2001).

[93] S. Vítek and M. Blažek, "Notes on DSLR photometry," (2012), vol. 7, p. 231.

[94] T. Lukeš, P. Křížek, Z. Švindrych, J. Benda, M. Ovesný, K. Fliegel, M. Klíma, and G. M. Hagen, "Three-dimensional super-resolution structured illumination microscopy with maximum a posteriori probability image estimation," Optics Express **22**, 29805–29817 (2014).

[95] T. Lukeš, G. M. Hagen, P. Křížek, Z. Švindrych, K. Fliegel, and M. Klíma, "Comparison of image reconstruction methods for structured illumination microscopy," (2014), p. 91293J.

[96] S. Vítek, J. Švihlík, K. Fliegel, J. Kukal, and Z. Krbcová, "Estimation of Poisson noise in spatial domain," (SPIE, 2017), p. 105.

[97] Z. Krbcova and J. Kukal, "Relationship between entropy and SNR changes in image enhancement," EURASIP Journal on Image and Video Processing **2017**, 83 (2017).

[98] M. Blazek and P. Pata, "Image processing of globular clusters - Simulation for deconvolution tests (GlencoeSim)," New Astronomy **48**, 24–29 (2016).

Publications of the Author Relevant to the Thesis

Journals with Impact Factor:

[A.1] Janout, P.; Páta, P.; Skala, P.; Bednář, J. *PSF Estimation of Space-Variant Ultra-Wide Field of View Imaging Systems*, In: Applied Sciences, 2017, 7(2).
ISSN 2076-3417   Shares: **25**/25/25/25

[A.2] Páta, P.; Klíma, M.; Bednář, J.; Janout, P.; Barta, C.; Hasal, R.; Maresi, L.; Grabarnik, S. *OFT Sectorization Approach to Analysis of Optical Scattering in Mercurous Chloride Single Crystals*, In: Optics Express, 2015, 23(16), 21509-21526.
ISSN 1094-4087   Shares: 17/17/17/**17**/8/8/8/8

[A.3] Janout, P.; Páta, P. *Orthonormalization, analysis and numerical approximation for general N-gon apertures*, In: Optical Engineering, 2018.
Under review.   Shares: **50**/50

Reviewed Journals:

[A.4] Janout, P.; Páta, P. *Celooblohová kamera s extrémně širokoúhlým zorným polem*, In: Jemná mechanika a optika, 2014, 59(10), 281-283.
ISSN 0447-6441   Shares: **50**/50

[A.5] Janout, P.; Skala, P.; Bednář, J.; Páta, P. *Měření vlastností extrémně širokoúhlých zobrazovacích systémů*, In: Slaboproudý obzor, 2015, 71(1), 11-13.
ISSN 0037-668X   Shares: **25**/25/25/25

[A.6] Bednář, J.; Anisimova, E.; Janout, P.; Páta, P. *Optická Fourierova transformace*, In: Jemná mechanika a optika, 2015, 60(11-12), 311-313.
ISSN 0447-6441   Shares: 25/25/**25**/25

Indexed in ISI:

[A.7]   Janout, P.; Blažek, M.; Páta, P. *New generation of meteorology cameras*, In: Photonics, Devices, and Systems VII. Bellingham: SPIE, 2017, Proceedings of SPIE. vol. 10603. ISSN 0277-786X.
ISBN 978-1-5106-1702-5   Shares: **33**/33/33

[A.8]   Fliegel, K.; Vítek, S.; Páta, P.; Janout, P.; Myslík, J.; Pecák, J.; Jícha, M. *Evaluation of color grading impact in restoration process of archive films*, In: Applications of Digital Image Processing XXXIX, Bellingham: SPIE, 2016, Proceedings of SPIE. ISSN 0277-786X.
ISBN 978-1-5106-0333-2   Shares: 14/14/14/**14**/14/14/14

[A.9]   Janout, P.; Páta, P.; Skala, P.; Fliegel, K.; Vítek, S.; Bednář, J. *Application of field dependent polynomial model*, In: Applications of Digital Image Processing XXXIX, Bellingham: SPIE, 2016. pp. 99710F-1-99710F-9, Proceedings of SPIE, ISSN 0277-786X.
ISBN 978-1-5106-0333-2   Shares: **17**/17/17/17/17/17

[A.10] Fliegel, K.; Janout, P.; Bednář, J.; Krasula, L.; Vítek, S.; Švihlík, J.; Páta, P. *Performance evaluation of image deconvolution techniques in space-variant astronomical imaging systems with nonlinearities*, In: Applications of Digital Image Processing XXXVIII, Bellingham: SPIE, 2015, pp. 959927-1-959927-14, Proceedings of SPIE, ISSN 0277-786X.
ISBN 978-1-62841-765-4   Shares: 14/**14**/14/14/14/14/14

[A.11] Janout, P.; Páta, P.; Bednář, J.; Anisimova, E.; Blažek, M.; Skala, P. *Stellar objects identification using wide-field camera*, In: Proc. SPIE 9450, Photonics, Devices, and Systems VI, Bellingham: SPIE, 2015. pp. 94501I-1-94501I-9, Proceedings of SPIE. ISSN 0277-786X.
ISBN 978-1-62841-566-7   Shares: **25**/15/15/15/15/15

[A.12] Anisimova, E.; Bednář, J.; Blažek, M.; Janout, P.; Fliegel, K.; Páta, P.; Švihlík, J.; Vítek, S. *Estimation and measurement of space-variant features of imaging systems and influence of this knowledge on accuracy of astronomical measurement*, In: Applications of Digital Image Processing XXXVII, Bellingham: SPIE, 2014, pp. 92171E-1-92171E-13, Proceedings of SPIE, ISSN 0277-786X.
ISBN 978-1-62841-244-4   Shares: 13/13/13/**13**/13/13/13/13

[A.13] Anisimova, E.; Fliegel, K.; Blažek, M.; Janout, P.; Bednář, J.; Páta, P.; Vítek, S.; Švihlík, J. *Analysis of images obtained from space-variant astronomical imaging systems*, In: Applications of Digital Image Processing XXXVI, Bellingham (stát Washington): SPIE, 2013, pp. 885607-1-885607-11, ISSN 0277-786X.
ISBN 9780819497062   Shares: 13/13/13/**13**/13/13/13/13

Remaining Publications of the Author

[A.14] de Ugarte-Postigo, A.; Blažek, M.; Janout, P.; Sprimont, P.; Thone, C.C.; Gorosabel, J.; Sánchez-Ramírez, R. *GRBSpec: a multi-observatory database for gamma-ray burst spectroscopy*, In: Proceedings of SPIE vol. 9152, Bellingham (stát Washington): SPIE, 2014, ISSN 0277-786X. ISBN 978-0-8194-9620-1   Shares: 14/14/**14**/14/14/14/14

[A.15] Páta, P.; Janout, P.; Bednář, J. *Čidlo slunečního svitu*, 2014.
                                                    Shares: 33/**33**/33

[A.16] Bednář, J.; Janout, P.; Páta, P.; Skala, P. *Studie k tématu vyhodnocení kvality provedení parkovacího manévru*, 2015.
                                                    Shares: 25/**25**/25/25

[A.17] Páta, P.; Janout, P.; Blažek, M. *Celooblohová kamera pro detekci typů mraků*, Functional Sample, 2018.
                                                    Shares: 33/**33**/33